Università degli Studi di Milano-Bicocca
Facoltà di Scienze Matematiche, Fisiche e Naturali
Dipartimento di Scienza dei Materiali

Doctorate in Nanostructures and Nanotechnologies

XXV cycle

Dislocation modelling in realistic Si-Ge nanostructures

Doctorate Thesis of :
Francesca Boioli
(054810)

Supervisor: Prof. Leonida Miglio
Coordinator: Prof. Gianfranco Pacchioni

January 2013

Contents

Introduction

SiGe heterostructures have gained a lot of interests in view of developing devices integrated into the main-stream Silicon technology and also from a scientific point of view as a prototypical system to understand the properties of more complex systems, such as III-V semiconductors. Si-Ge epitaxial structures, as well as other mismatched heteroepitaxial materials, have a high potential to improve the state-of-the-art of Si devices, thanks to the fact that the strain modifies the band structures of this material class, opening new possibility of band-gap engineering. Since the nineties, the development of devices having strained-SiGe layers as the active part occurred, in particular the heterojunction bipolar transistors, further developed to what is presently the fourth-generation of SiGe technology. Also the introduction of strained Si layers by using relaxed SiGe virtual substrates, is very important, for example, for the complementary metal–oxide–semiconductor (CMOS) technology.

In order to effectively exploit SiGe or strained-Si layers in any application, it is fundamental to growth high quality single crystalline materials, reducing as much as possible the defect density in the active volume and the surface corrugation, and to obtain the desired strain state in the epitaxial layers. However the possibility of using such heterostructures for any application, is hindered by the nucleation of dislocation, which is often an unavoidable strain-relief mechanisms. Dislocation formation affects both the final material quality and the relaxation degree of mismatched layers. These defects are often charged and act as non-radiative recombination centers and it is generally accepted that they are detrimental for opto-electronic devices based on Si-Ge semiconductors. Moreover, a cross hatch morphology at the surface is typically produced by misfit dislocations at the substrate-epilayer interface, so as to increase the layer roughness. In the past years, a lot of effort has been devoted reduce the defect density or to segregate dislocations in non-active regions. However, dislocation engineering, intended as the precise control of dislocation position, has always been a goal out of reach, because of the nucleation of such defects at unpredictable sites at the surface or at other heterogeneities. It is clear that predicting the extent of the plastic relaxation process and governing dislocation nucleation and positioning would be of the utmost importance.

Self-assembled nanoislands and nanowires represent other novel heterostructures that can be exploited to obtain defect-free configurations with the desired strain state. Even in this case, very high stresses arise from the epitaxial integration of lattice mismatched materials and dislocation formation remains a competitive strain relief mechanism. Hence it is of fundamental importance to determine the coherency limits of such nanostructures and to

elucidate the main strain relief mechanisms in the attempt to predict the final dislocation microstructure and strain state in heteroepitaxial systems.

The main goal of this work, is the understanding of the fundamental mechanisms of dislocation nucleation and propagation in Si-Ge nanostructures (i.e. films, nanoislands and nanowires) through dislocation modelling. Even if dislocation formation and motion relies on a sequence of discrete atomic displacements, such defects induce in a crystal a smooth deformation field in the entire structure. The elastic theory of dislocations provides a good description of such stress field and of the elastic energy, as produced by dislocations in bulk materials or in finite size solids with simple geometries. In order to assess the stresses and the energetics of plastically relaxed multifaceted structures, characterized by an high surface to volume ratio and typical length scale in the order of tens or hundreds of nanometers, linear elasticity theory numerically solved by finite element methods is the most suitable tool, since in this approximation the dislocation-surface interaction can be correctly taken into account. Moreover, the motion of dislocations in nanostructures can be handled by using three-dimensional dislocation dynamics simulations. This simulation technique, originally developed to study plasticity in bulk materials, has been demonstrated to give accurate results also for nanometric systems, and is the tool of choice to study the motion and interactions of a large density of dislocation in thin films or three-dimensional nanocrystals. In this work, we employed the microMegas code [1] suitably modified in collaboration with Dr. B. Devincre and Dr. R. Gatti to handle dislocation motion in realistic nanostructures which may expose many surfaces and form both convex and concave domains. Important properties determined by the atomistic nature of dislocations moving in a discrete lattice, can be included, both in the finite element calculations and in dislocation dynamics simulations, by adopting simple rules that take into account such atomistic features.

The first topic addressed in this work, is the investigation of plastic relaxation in SiGe epitaxial films aimed at governing dislocation nucleation and positioning. In particular, we show with the help of finite element calculations and dislocation dynamics simulations that a turning point to direct dislocation formation and propagation in predefined regions, is the introduction of preferential nucleation sites through substrate nanopatterning. Theoretical predictions indicating effective dislocation trapping along the features of trench- or pit-patterned substrates are discussed and compared with tailored experiments of SiGe deposition on nanopatterned substrate.
The second issue investigated here concerns self-assembled SiGe nanoislands. In these epitaxial nanostructures an intriguing mechanism of dislocation ordering is observed. In this work we reproduced such behavior by using a simple analytical model based on energetics considerations. Furthermore, the plastic relaxation onset for dislocation formation has been determined in epitaxial islands grown on pit-patterned substrates and nucleated in pits. The key factors influencing dislocation formation in such structures have been identified, opening new possibility to grow large defect-free islands on nanopattered substrates.
The last topic considered here, is dislocation formation in core-shell nanowires. Elastic and plastic strain relaxaion has been investigated in such structures and a mechanism for

[1] developed at the Laboratoire d'Etude des Microstructures in Châtillon (France)

dislocation nucleation and propagation in core-shell nanowires is presented. This allowed us to predict dislocation configurations that are more efficient in the strain relief process and the expected misfit dislocation pattern at the core-shell interface.

In the following, it is outlined how the present manuscript is organized.

In Chapter 1, a brief introduction on the concept of dislocations is given, presenting the main properties determined by the atomistic nature of dislocations and by the influence of the crystal lattice on these defects.

In Chapter 2, the basic aspects of the heteroepitaxial growth are presented. In particular, the growth of Si-Ge alloys on Si(001) substrates, leading to a two-dimensional layer by layer growth or to three-dimensinal nanoscrystal formation, is reviewed and the principal strain relaxation mechanisms in such a system are discussed. Moreover, the formation of one-dimensional heterostructures, nanowires, with different architectures, among those the core-shell nanowires, is illustrated.

In Chapter 3, the dislocation properties derived by elastic dislocation theory are described and the methods adopted to model dislocations in heteroepitaxial nanostructures are presented. First, the relevant definitions and concepts extracted by linear elasticity theory and classical dislocation theory are summarized. The analytical solutions for the energy and the stress field induced by dislocations in bulk materials are discussed as a starting point for the modellization of plastic relaxation in more complex systems. Second, the methodology adopted to calculate the stresses and the energetics of elastically and plastically relaxed heteroepitaxial nanostructures, as obtained by using finite element calculations, is reported. Finally, the dislocation dynamics simulation technique, used to address dislocation motion in nanostructures, is presented.

In Chapter 4, results on plastic relaxation in low mismatched SiGe films are reported. The influence of trench- and pit-patterned substrates in the elastic and plastic relaxation of conformal films grown on top of them has been investigated. In particular, by using finite element calculations and dislocation dynamics simulations, it is shown that is possible to direct preferential dislocation nucleation and positioning by growing SiGe films on suitably patterned Si(001) substrates.

In Chapter 5, results on plastic relaxation in SiGe nanoislands are presented. First, misfit dislocation formation and ordering in SiGe islands grown on flat Si substrates is addressed by using a simple analytical energy balance model. Second, the onset of plastic relaxation in islands grown on pit patterned substrates and nucleated in pits has been studied by finite element calculations in order to determine the coherency limits for growing such nanostructures and the effect of the substrate patterning in delaying dislocation formation at larger volumes is demonstrated.

In Chapter 6, results on dislocation formation in Si-Ge core-shell nanowires are discussed. In particular, an analysis based on the effective stress responsible for dislocation nucleation and propagation in the epitaxial shell is presented. This analysis followed by dislocation dynamics simulations was used to determine the expected dislocation configurations in nanowires and to estimate the critical shell size for growing coherent core-shell heteroepitaxial wires. Finally, the main results and the perspectives emerging from this work are summarized in the Conclusions.

1

Dislocations in the Si-Ge lattice

The development of experimental techniques such as x-ray diffraction or trasmission electron microscopy, allowed to recognize and directly observe the presence of defects in crystal lattice. Among them, particular interest has been dedicated to dislocations, because these defects govern the crystal ability to flow and yield under stress, as well as many other mechanical behaviors, such as creep, fatigue, ductility and brittleness. Moreover, they influence crystal growth and affect optical and electrical properties of metal and semiconductor materials. Dislocations can develop in crystalline materials during the crystal growth, either for kinetic or thermodynamic reasons, or after the crystal growth under the application of stresses or strains. In fact, since dislocations induce a stress field in the crystal lattice, the formation of this kind of defects represents an effective mechanism for the elastic energy relaxation in systems undergoing tensile or compressive deformations. In particular, in heteroepitaxial growth processes, large strains arise from the epitaxial integration of one material on a different one and dislocations are formed in response to such a deformation. One of the objectives of this work is to understand the mechanisms of dislocation formation and propagation in such heteroepitaxial structures. The scope of this Chapter is to recall the basic definitions and concepts about dislocations in crystals, that are extesively used throughout this work, and to describe the main characteristics of dislocations in diamond lattice materials, such as Si and Ge.

1.1 Introduction to crystal dislocations

Dislocations are defects of the crystal lattice topology and can be described by the displacements of atoms in a perfect crystal from their equilibrium positions. A review of the basic aspects of dislocations can be found in Ref. [1, 2], while we refer Ref. [3] for a detailed and comprehensive analysis of the classical dislocation theory.
There exhist different types of dislocations. Among them the *edge* and the *screw* types are the most important ones. All the other dislocations can be described as a combination of the these two dislocations and for this reason are called *mixed* type. As we will see, dislocation position and type are defined by two important vectors, the Burgers vector $\boldsymbol{b}$ and

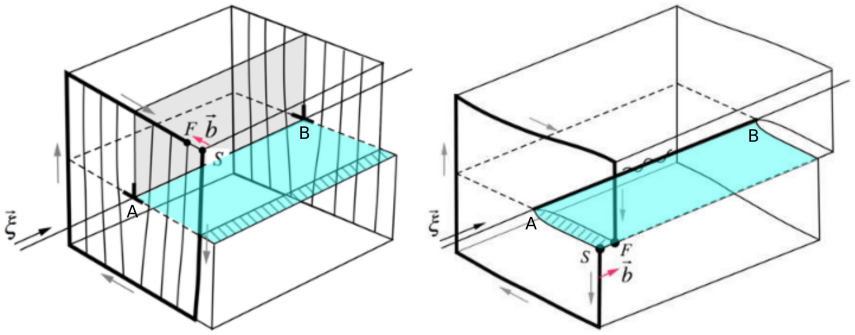

FIGURE 1.1: Sketch of an edge (a) and a screw (b) dislocation.

the line direction $\boldsymbol{\xi}$, and by their reciprocal orientation. An edge and a screw dislocation are sketched in Fig. 1.1 (a) and (b), respectively. The two dislocation lines are indicated by the segments AB (parallel to the vector $\boldsymbol{\xi}$) and the two Burgers vectors are drawn with a red vector $\boldsymbol{b}$. Let us consider a perfect structure and to cut it along the plane colored in blue, as in Fig 1.1. If the regions above and below the cutting plane are displaced in the opposite directions perpendicularly to the line AB, we obtain an edge dislocation, as in Fig. 1.1(a). If instead the same two regions are displaced in the opposite directions parallel to the line AB, a screw dislocation is formed, as in Fig. 1.1(b). In case they are displaced in a general direction, which is neither parallel, neither perpendicular to the line AB the dislocation is a mixed one. As can be observed in Fig. 1.1(a), an edge dislocation can be identified in the crystal by the presence of an extra half plane in the deformed region (see the grey plane). In this case the dislocation line can be identified with the edge of the extra half plane. Instead, if in a crystal a screw dislocation is present, the lattice planes perpendicular to the dislocation line are tilted around the dislocation line AB, as in screw thread. Such a deformation is a shear deformation in the planes parallel to the dislocation line, whereas in the planes perpendicular to it no deformation is observed.

From the description above, it is clear that the dislocation line represents the boundary between a slipped and an unslipped crystal region. Consequently, a dislocation cannot end at any point of a perfect crystal, but it has to terminate in correspondence to a boundary, a free surface, or an other dislocation or defect position. Otherwise, it must form a closed loop. This concept has been demonstrated in the linear elasticity framework [4], but it also follows from the definition of $\boldsymbol{b}$ below.

1.1.1 Burgers vector and dislocation line

Dislocations are one-dimensional defects that can assume an arbitrary shape: straight segments, closed loops or curved dislocation lines. In order to give a precise description of their position and shape, it is useful to define a vector field that indicates the line direction at any point $\boldsymbol{r}$ of the defect. The *line direction* $\boldsymbol{\xi}(\boldsymbol{r})$ is then defined as the versor parallel to tangent of the dislocation line in $\boldsymbol{r}$ along its positive direction. While the line direction can change along a single dislocation line, the direction of the atoms displacements induced by the dislocation remain constant. The Burgers vector represents

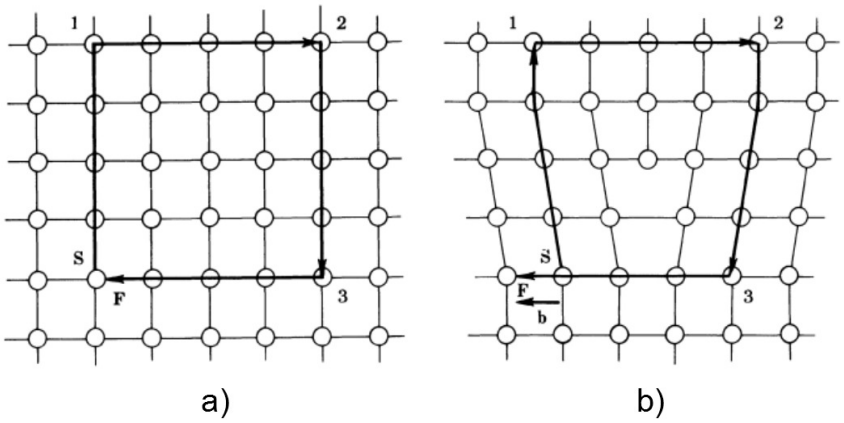

FIGURE 1.2: Burgers circuit in a perfect crystal (a) and around the dislocation line (b). The Burgers vector is the vector (SF) connecting the start with the finish sites of the circuit. The sense of the circuit is that of a right-hand (RH) screw. The convention adopted to define the Burgers vector is the SF/RH convention.

the dislocation displacement vector. Let us consider a perfect simple cubic crystal and the same crystal with an edge dislocation, as shown in Fig. 1.2. In order to define the Burgers vector we need first to assign the dislocation line direction $\boldsymbol{\xi}$. In Fig. 1.2(b) the positive sense of $\boldsymbol{\xi}$ is taken to be into the paper. In fig. 1.2 two clockwise circuits are drawn; the first in the perfect crystal and the second one around the dislocation line. Both start at the position $\boldsymbol{S}$ and finish in $\boldsymbol{F}$. Each circuit segment (vertical and horizontal ones) is made by the same number of lattice vectors. The circuit on the left, in the perfect crystal, is a closed loop, whereas by doing the same displacements around the dislocation, we found a vector $\boldsymbol{F} - \boldsymbol{S}$ upon closure of the circuit. This vector is the *Burgers vector*. The Burgers vector can be also obtained by summing all the vectors $\boldsymbol{\Delta u_i}$, that are the differences between the atom-pairs distances in a perfect crystal, Fig. 1.2(a), and in the distorted one, Fig. 1.2(b), along the Burgers circuit:

$$\boldsymbol{b} = \boldsymbol{F} - \boldsymbol{S} = \sum \boldsymbol{\Delta u_i} \, . \tag{1.1}$$

This definition can be extended to a continuum medium, and the Burgers vector is given by the integral of the atom diplacements $\boldsymbol{u}$ from the perfect crystal positions, along a close circuit around the dislocation line:

$$\boldsymbol{b} = \int_c \frac{\partial \boldsymbol{u}}{\partial \ell} d\ell \, , \tag{1.2}$$

where C can be any close path around the dislocation line and $\partial \boldsymbol{u}/\partial \ell$ is the gradient of the displacement field (see Section 3.3.1) along this path. The definition of $\boldsymbol{b}$ is not unique, but depends on the convention adopted. Here we have reported the SF/RH convention that will be used throughout this work (the vector closing the Burgers circuit, goes from the finish site to the start poitn (SF) and the sense of the circuit is that of a right-handed screw RH). By adopting this convention the position of the extra half-plane around an edge dislocation can be found by using the right-hand rule. In particular, the unit vector

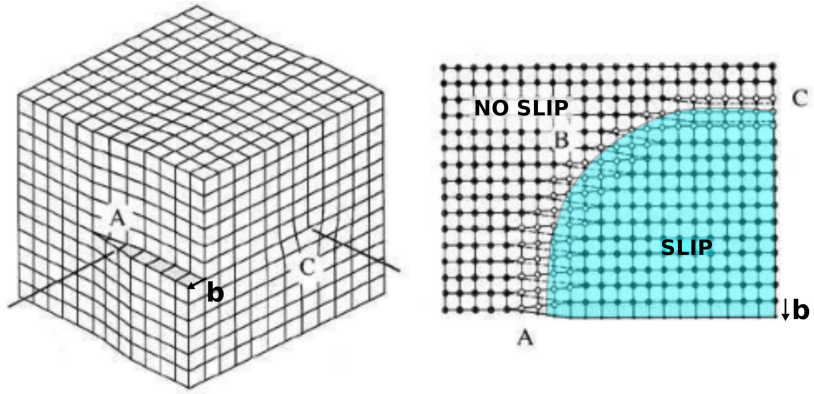

FIGURE 1.3: Mixed dislocation characterized by edge and screw components that vary along the dislocation line. In (a) the dislocation starts with screw character. The line bends and assumes a mixed character in B and terminates at an other surface in C as an edge type dislocation. The slip region is colored in blue.

$\boldsymbol{\xi} \times \boldsymbol{b}/b$, starting at the dislocation location, indicates the position and the direction of the extra half-plane of atoms. We notice that by reversing the direction of $\boldsymbol{\xi}$ in the above definition of $\boldsymbol{b}$, the Burgers vector would results in the same direction but opposite in sign. This means that the same dislocation can be described by the two vectors $\boldsymbol{\xi}$ and $\boldsymbol{b}$, or equivalently, by $-\boldsymbol{b}$ and $-\boldsymbol{\xi}$.

The same Burgers vector definition can be applied to screw or mixed type dislocations. In Fig. 1.1, the Burgers vector is found by following the convention adopted above, for both the edge and the screw dislocation. The Burgers circuit is indicated by the grey arrows.

It is now clear that the Burgers vector of a screw dislocations is parallel to the line direction ($\boldsymbol{b} \cdot \boldsymbol{\xi}=b$ for a right-hand screw and $\boldsymbol{b} \cdot \boldsymbol{\xi}=-b$ for a left-hand screw), while the one of an edge dislocation is perpendicular to $\boldsymbol{\xi}$ ($\boldsymbol{b} \cdot \boldsymbol{\xi}=0$). In case of a mixed dislocation, $\boldsymbol{\xi}$ can assume an arbitrary direction with respect to $\boldsymbol{b}$. The character or type of a dislocation is defined by the angle between its line direction $\boldsymbol{\xi}$ and its Burgers vector $\boldsymbol{b}$. When the dislocation line is straight, the reciprocal orientation between $\boldsymbol{b}$ and $\boldsymbol{\xi}$ is constant and dislocations are denominated by the angle they form. Mixed type dislocations can be described as the combination of a screw and an edge dislocation having as their Burgers vectors, the components of original Burgers vector $\boldsymbol{b}$ projected onto the directions parallel and perpendicular to the dislocation line, respectively. In particular, since $\boldsymbol{\xi}$ can change along a dislocation, but $\boldsymbol{b}$ is invariant, the character of the dislocation along its line is given by its Burgers vector screw and edge components $\boldsymbol{b_S}$ and $\boldsymbol{b_E}$:

$$\boldsymbol{b_S} = (\boldsymbol{b} \cdot \boldsymbol{\xi})\boldsymbol{\xi} \tag{1.3}$$

$$\boldsymbol{b_E} = (\boldsymbol{b} \times \boldsymbol{\xi}) \times \boldsymbol{\xi} \, . \tag{1.4}$$

In Fig. 1.3 we sketched a dislocation with variable character along its line. The region where the slip displacement has occurred is colored in blue. The dislocation character varies along the line as $\boldsymbol{\xi}$ changes its direction, while $\boldsymbol{b}$ is conserved.

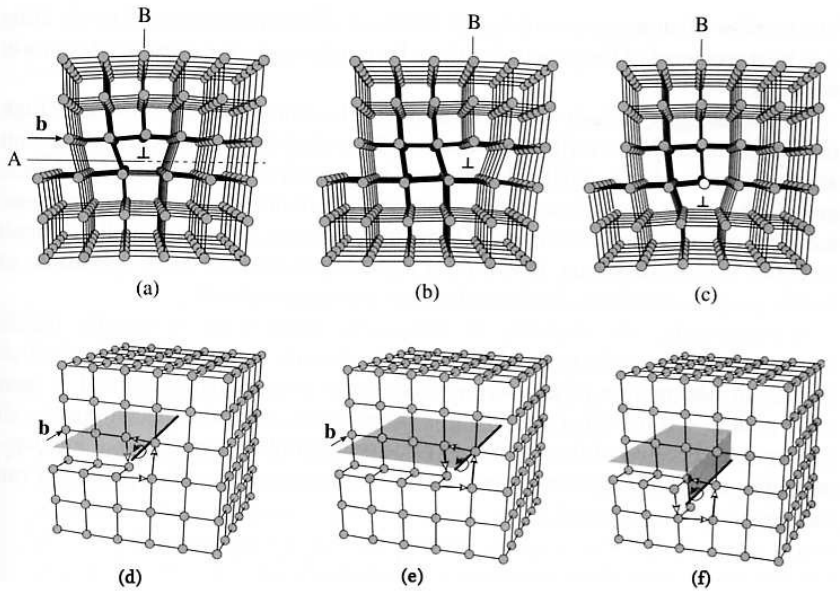

FIGURE 1.4: An edge dislocation in a simple cubic crystal. When it moves on its glide plane by one lattice spacing (b) no atoms need to be inserted or removed. When it moves perpendicular to its glide plane (c) a row of atoms (white spheres) needs to be inserted. (d) A screw dislocation in a simple cubic crystal. Regardless of which direction the dislocation moves, (e) and (f), no atom needs to be inserted or removed. [5]

1.1.2 The dislocation motion

The motion of dislocations under an applied stress field provides an explanation for plastic deformation in crystals. While the driving force for this motion can be derived from continuum elasticity theory, as it is discussed in Section 3.3, the mechanisms for dislocation motion and the response to this force are governed by the crystal lattice properties and by atomistic mechanisms.

Two different mechanisms have been proposed to describe the dislocation motion: the glide and the climb process. A simple explanation for these two mechnisms relies on the different motion of screw and edge dislocation segments. Let us consider a straight edge dislocation as drawn in Fig. 1.4(a) and let us move it by one lattice spacing along the direction parallel to its Burgers vector in the plane indicated by A. To reach this position, all it requires is for a row of atoms at the right of the dislocation core to break their bonds and to exchange their neighbours with the atoms at the edge of the extra half-plane at the dislocation position, as shown in Fig. 1.4(a,b). If the same dislocation is moved by one atomic step along the direction perpendicular to $\boldsymbol{b}$ and parallel to the plane indicated by B, up or down, we need to remove or add a row of atoms, respectively, as it shown in Fig. 1.4(a,c). In (b) the dislocation move inside its *glide plane*, defined as the plane that contains simultaneusly the Burgers vector and the dislocation line (the normal of the glide plane is then defined by $\boldsymbol{b} \times \boldsymbol{\xi}$), while in (c) it moves perpendicularly to it. The motion along the glide plane is called, accordingly, *glide*, whereas the motion out of it is called climb. Glide and climb are also called conservative and non-conservative motion, because

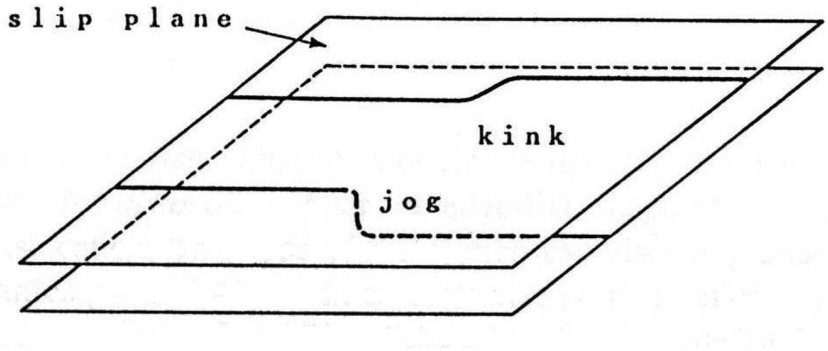

FIGURE 1.5: Sketch of a dislocation kink and jog.

in the first case the total number of atoms is conserved, while in the second case a row af atoms should be provided or removed. Obiously, in real crystals atoms are neither added or eliminated, but climb motion is possible thanks to atoms or vacancies diffusion, that are absorbed or emitted by the dislocation. The definition of the glide plane for a screw dislocation is not unique, since in this case $\boldsymbol{b} \parallel \boldsymbol{\xi}$. As a consequence, the motion of a screw dislocation does not require the insertion or removal of atoms, regardless of the movement direction, as shown in Fig. 1.4(e,f). Hence a screw dislocation can always glide. In case of a mixed dislocation, the glide plane is determined by $\boldsymbol{\xi} \times \boldsymbol{b}$, as for the edge case.

At moderate temperatures and stress the glide motion is governed by the thermally assisted kink pair mechanism. The dislocation glide is assumed to involve the creation and migration of kink pairs, which are two symmetric steps in the dislocation line, which make a small segment of the dislocation line to be displaced by one row of atoms to the adjacent one, as shown in Fig. 1.5. By the lateral motion of the kinks away from each other in opposite directions, the entire dislocation line is moved by one atomic step in the glide plane. The formation of kink pairs is then followed by their migration (whith the assistance of stress or thermal fluctuations), resulting in the progressive dislocation glide motion. In this regime the dislocation motion is thermally activated, due to the energy barrier for kink formation and the mobility drastically increases with temperatures. At high temperature and stress, glide is no more thermally activated and can be described as a simple dissipative motion where the dislocation velocity is proportional to the stress and it is limited by the lattice resistance due to dislocation interaction with lattice vibrations. In this regime the glide motion is governed by a viscous drag mechanism.

The equivalent of kinks for the climb motion are called jogs, see Fig. 1.5. This motion can developed similarly to glide, creating a symmetric pair of steps (jogs) perpendicularly to the glide planes. However, climb requires atoms or vacancies diffusion and is generally more difficult. In general dislocations can move by a combination of glide and climb motion. At low and moderate temperatures climb is tipically neglected, and dislocations are assumed to move by glide motion only since it requires less energy. The climb motion can be activated only at sufficiently high temperature or under the condition of vacancy super-saturation. Even in this case, the time scale for the two kinds of motion is usually

very different, being climb slower than climb, and for this reason they are rarely treated together. In this work, we have neglegted the climb motion, as it does not play a significant role in the systems investigated.

1.1.3 Slip systems

As glide motion is expected to be the favorite mechanism for dislocation motion in most conditions (e. g. low and moderate temperature), it is fundamental to understand which are the planes in a crystal structure where dislocations can effectively glide. The motion of dislocations is defined by the active *slip systems*. A dislocation slip system is defined as the combination of the Burgers vector and the glide plane which characterize the dislocation, i.e. the direction of the displacements induced by the dislocation and the crystallographic plane where it moves. Once the possible Burgers vectors and glide planes are defined, the limits for dislocation motion in a crystal are established. In the previous paragraph, we have associated the Burgers vector with a unit lattice vectors in a simple cubic structure. In general, it is possible to associate dislocation Burgers vectors with lattice vectors, and among them, it is reasonable to consider the ones small in magnitude. Dislocations with Burgers vector equal to a lattice vector, or a multiple of it, are called *perfect* dislocations. Instead, if the Burgers vector cannot be decomposed in a sum of lattice vectors the dislcoations are called *partial* dislocations. Here and throughtout this work we will consider only perfect dislocations. In between all the possible perfect dislocations, typically, only those with the shortest Burgers vector are stable. This has been explained in terms of dislocation energy by Frank [6]. Since the energy of a dislocation is proportional to b^2 (see Section 3.3), he proposed that in a first approximation it is possible to neglect the other terms contributing to the dislocation energy. In particular, in order to establish the stability of a dislocation, he proposed that a perfect dislocation with Burgers vector $\boldsymbol{b_1}$ that can dissociate into perfect dislocations $\boldsymbol{b_2} + \boldsymbol{b_3}$ will disssociate if:

$$b_1^2 > b_2^2 + b_3^2 \, . \tag{1.5}$$

A more precise procedure would require to include the exact expression for the dislocation energy, which is known to depend also on the character of the dislocation. However, this criterion, tells us immidiately that the shorter is the Burgers vector, the lower is the dislocation energy and the more stable is the dislocation itself. Also, if $\boldsymbol{b_1}$ is a multiple of a lattice vector so that $\boldsymbol{b_1} = 2\boldsymbol{b_2} = 2\boldsymbol{b_3}$, the dislocation will dissociate into $\boldsymbol{b_2} + \boldsymbol{b_3}$.

Single crystalline materials deform by glide in the close packed directions. In fact, planes with the highest density of lattice sites have the largest spacing between two adjacent planes. As a consequence they have a lower resistance to the glide motion with respect to the other crystallographic planes. Following first the Frank criterion, perfect dislocations with Burgers vectors equal to the minimum lattice vectors are expected. Moreover, among the possible glide planes that contain such Burgers vectors, the closest packed planes in the crystal structure are the favorite ones to promote dislocation glide motion. By following these two simple criteria, it is possible to identify the preferential slip systems in most of the crystal structure and materials.

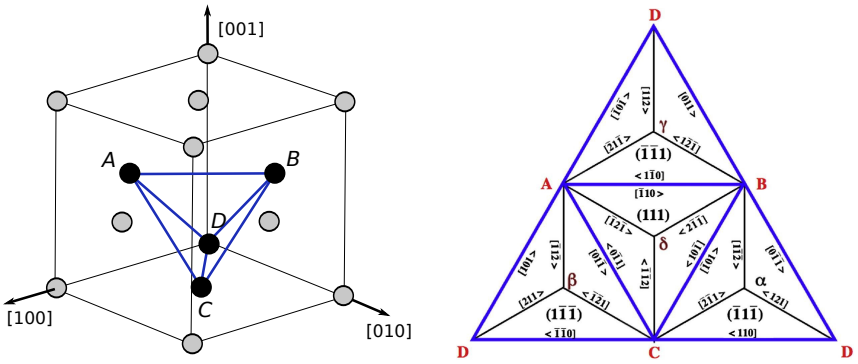

FIGURE 1.6: (a) Diamond lattice cubic cell and the Thompson tetrahedron highlighted in blue, illustrating the possible slip planes and the Burgers vectors of dislocations in a diamond crystal. (b) Two-dimensional representation of the Thompson tetrahedron [7].

1.2 Dislocations in the diamond structure

In Face Centered Cubic (FCC) and diamond structure materials, the minimum lattice vectors are the $a/2\langle 110\rangle$ and the planes containing them with the highest lattice site density are the $\{111\}$. Thus in these structures the most favorite slip systems, the primary slip systems, are are the $\langle 110\rangle\{111\}$, characterized by $\{111\}$ glide planes and Burgers vectors along the $\langle 110\rangle$ directions. This prediction has been confirmed by a series of experiments. The number of slip systems of this type is 12, and is given by all the possible combinations of $\{111\}$ slip planes and $\langle 110\rangle$ Burgers vectors. These are visulized in Fig. 1.6 by using the Thompson tetrahedron construction. In Fig. 1.6(a) a tetrahedron bounded by the four different $\{111\}$ planes in the diamond cubic cell is shown. In Fig. 1.6(b) the same tetrahedron is represented in two dimension with three lateral facets of the tetrahedron bounded to a central one. In this construction the facets of the tetrahedron represent the four $\{111\}$ glide planes and its edges represent the possible Burgers vector along the $\langle 110\rangle$ directions.

1.3 Dislocations in the Si-Ge heteroepitaxial system

In the heteroepitaxial Si-Ge system, the most commonly observed dislocations are the following three types:

- screw dislocations. Burgers vector and dislocation line are parallel and aligned to one of the $\langle 110\rangle$ directions; $\boldsymbol{b}$ and $\boldsymbol{\xi}$ lie in the same glide plane and parallel to each others.
- 60°dislocations. Burgers vector and dislocation line are parallel to the $\langle 110\rangle$ directions; $\boldsymbol{b}$ and $\boldsymbol{\xi}$ lie in same glide plane and form a 60°angle
- edge dislocations. Burgers vector and dislocation line are parallel to the $\langle 110\rangle$ directions; $\boldsymbol{b}$ and $\boldsymbol{\xi}$ are perpendicular to each others and they do not lie in same glide plane.

Throughout this manuscript, we will call 60°and 90°dislocations, the above described dislocation types. In heteroepitaxial Si-Ge structures, the most important dislocations are the 60°dislocations, as they can nucleate and propagate in the low energy {111} glide planes. On the contrary, edge dislocations aligned to the ⟨110⟩ directions have Burgers vector and dislocation lying in a {100} plane, so that they cannot propagate easily by glide motion. However, these edge dislocation can be formed by reaction of two 60°dislocations giving rise to the well known Lomer-Cottrell junction.

2

$Si_{1-x}Ge_x$ heteroepitaxy

The epitaxial integration of different materials on top of a Si substrate is fundamental in order to obtain devices integrated in the actual Si-based technology. This achievement can be reached by controlling the growth morphology, the strain accumulated in the heteroepitaxial deposition and the defect microstructure. In this chapter, we recall the basic aspects of the heteroepitaxial growth of lattice mismatched materials and the main mechanisms of strain relaxation observed in such systems. In particular, we focused on the crystal growth of $Si_{1-x}Ge_x$ alloys deposited on a Si(001) substrate, and on the possible growth modalities, leading to two-dimensional (2D) or three-dimensional (3D) heteroepixial architectures. Finally we introduce the catalyst assisted growth of Si-Ge nanowires and the principal one-dimensional heteroepitaxial structures that can be produced.

2.1 Heteroepitaxial growth modes

Heteroepitaxy consists in the single-crystal growth of a material A on the substrate surface of a different crystalline material B. This can be achieved by using deposition techniques such as Molecular Bean Epitaxy (MBE), Chemical Vapor Deposition (CVD) or Metalorganic Vapor Phase Epitaxy (MOVPE). Advancements in this field allowed for the deposition of different species on a variety of substrate materials and orientations. A review of these growth techniques can be found in Ref. [8, 9]. Both lattice matched and mismatched materials can be grown. In the latter case, strain relaxation mechanisms are present that strongly influence the morphology of the epilayer.

Three different growth modes are distinguished in heteroepitaxy [10]: the 2D layer by layer or Frank-van der Merwe (FM) growth, the 3D island formation or Volmer-Weber (VW) growth modality and the Stranski-Krastanow (SK) mechanism, characterized by the initial formation of a 2D layer, followed by 3D island nucleation and evolution. The FM growth consists in the formation of a complete monolayer on the flat substrate surface before starting the nucleation of the second layer. The subsequent development of one monolayer on top of another one leads to the formation of a thick 2D film. On the contrary, the VW growth is characterized by the formation of 3D isolated clusters, also

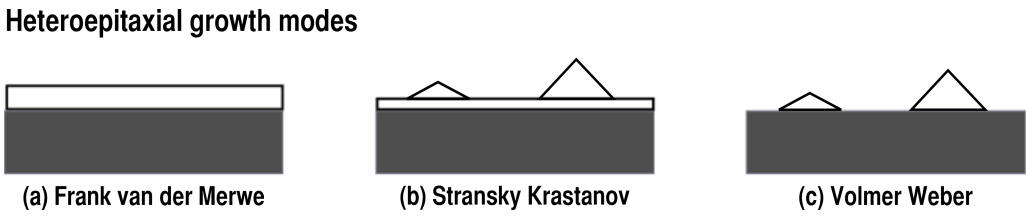

FIGURE 2.1: Heteroepitaxial growth modes. (a) Layer by layer, or Frank van der Merwe (FM) growth. (b) 3D island formation on top of thin wetting layer, or Stransky Krastanov (SK) growth. (c) 3D island formation on top of the substrate surface, or Volmer Weber (VW) growth mode.

called islands, directly on top of the substrate surface. Finally, in the SK growth modality the deposition proceeds through the initial formation of a 2D thin layer that wets the substrate surface, named wetting layer (WL), followed by 3D island nucleation on top of it. These three growth modalities are schematically shown in Fig. 2.1. In the equilibrium theory of heteroepitaxy, the growth mechanisms observed can be explained in terms of surface and interfacial energy minimization. In absence of strain, the favorable growth mode can be identified by considering the areal change in the surface energy $\Delta\gamma$ associated with the covering of the substrate with an epitaxial layer. If γ_e and γ_s are the surface energy of the epilayer and of the substrate and γ_i is the interfacial energy between the two materials, then:

$$\Delta\gamma = \gamma_e + \gamma_i - \gamma_s \ . \tag{2.1}$$

Following the surface energy minimization criterium, if $\Delta\gamma < 0$ the preferential growth mechanism will be two-dimensional, while if $\Delta\gamma > 0$, 3D island formation will be expected. Assuming that the interface contribution γ_i is negligible with respect to the surface terms, 2D growth occurs when $\gamma_e < \gamma_s$, so that the epilayer will cover the exposed substrate surface decreasing the total energy. On the contrary, if $\gamma_e > \gamma_s$, the surface energy minimization leads to 3D clusters formation. However, if a lattice mismatch exists between the substrate and epilayer, even in the case of $\gamma_e < \gamma_s$, the misfit strain can induce islanding after the initial 2D wetting layer formation. This is because the elastic energy stored in the system increases linearly with the layer thickness, and after some monolayers it can be energetically favored to create 3D islands, that can relieve the mismatch strain thanks to the exposed sidewalls. Therefore, the SK mechanisms is expected in case of wetting epitaxy ($\gamma_e < \gamma_s$) and high film/substrate mismatch. Whereas, the VW growth mode is favored in case of non-wetting epitaxy ($\gamma_e > \gamma_s$).

The morphological evolution of realistic SK systems is generally more complex and needs further considerations. An early attempt to elucidate this mechanism was developed by Daruka and Barabási [11]. Their model captures the main features of this growth modality and they succeeded in building an equilibrium phase diagram for heteroepitaxy of a wetting material A on a substrate B, as a function of the deposited material volume, expressed in monolayers, and of the mismatch strain, that can help predict the heteroepitaxial growth mode. Still, in order to capture the realistic island evolution with the increasing deposition volume, a more detailed approach is needed that takes into account the surface energies of the exposed facets and the elastic strain relaxation variation with

the island shape and volume.
This scenario is further complicated by kinetic factors (e.g. diffusion barriers at step edges, the Ehrlich-Schwoebel barrier) or different growth conditions (e.g. temperature, deposition flux, or introduction of surfactants) that can play a significant role and modify the expected epilayer growth mode [12]. Investigation of the competitive strain relaxation mechanisms in the different growth conditions is fundamental in order to predict the final heteroepitaxial structure and to drive the growth towards the desired morphology. In the next sections we will discuss in more details the $Si_{1-x}Ge_x$/Si(001) growth and the key thermodynamic and kinetic factors that are relevant for this system.

2.2 Si-Ge alloy properties

Silicon, Germanium and Si-Ge alloys have the same diamond crystallographic structure. This can be described as a face centered cubic (FCC) lattice characterized by a basis of two atoms at each lattice point: one at origin of the unit cell and the second one displaced by one quarter of the diagonal unit cell from the origin. Si and Ge share the same cubic structure but have different lattice parameters, the Ge lattice constant being ∼4% larger than the Si one. The two materials can be alloyed as $Si_{1-x}Ge_x$ with any value of $0 \leq x \leq 1$. Throughout this work, we considered the lattice constant of the Si-Ge alloy to change with x according to the Vegard's law:

$$a_{SiGe} = a_{Ge}\, x + a_{Si}\, (1 - x) \tag{2.2}$$

where a_{Ge}, a_{Si} and a_{SiGe} are the Ge, Si and $Si_{1-x}Ge_x$ alloy lattice parameters, respectively. Also the misfit strain f is assumed to vary linearly with the Ge concentration in the $Si_{1-x}Ge_x$ alloy:

$$f = \frac{a_{SiGe} - a_{Si}}{a_{Si}} = \frac{a_{Ge} - a_{Si}}{a_{Si}}\, x = x\, f_{Ge} \tag{2.3}$$

with f_{Ge} being the misfit between pure Ge and Si. Deviations from such a linear relation are expected [13]. However, due to the high mismatch between these two materials, the approximation adopted does not affect significantly the misfit strain value. The values of the Si and Ge lattice constants measured at room temperature (300K) are $a_{Ge} = 0.5658$ and $a_{Si} = 0.5432$ nm. With the increasing temperatures these values increase due to thermal expansion. Even though Si and Ge have a different thermal expansion coefficient, the lattice constants difference at high growth temperatures (∼ 1000K) is only the 0.2% larger with respect to the lattice mismatch measured at 300K (one order of magnitude smaller than the 4%) [14, 15]. Throughout this work we neglected the dependence of the Si/Ge lattice constants on temperature, since it is a minor contribution and we used the values observed at room temperatures and reported above.

2.3 $Si_{1-x}Ge_x$ epitaxial growth

The deposition of a $Si_{1-x}Ge_x$ alloy on top of a Si(001) substrate starts with the formation of a thin pseudomorphic 2D layer, since the Ge(001) (or Si-Ge alloy) surface energy is lower

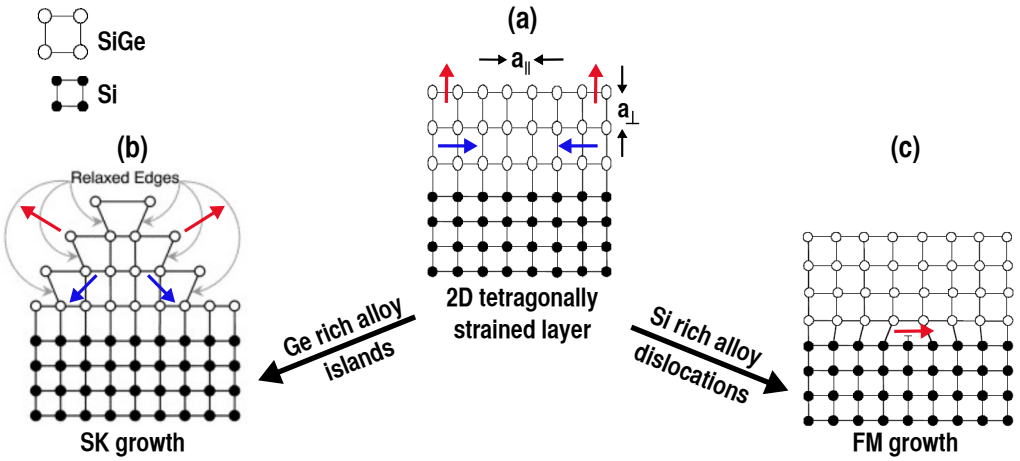

FIGURE 2.2: The deposition of SiGe on top of Si strat with the formation of a thin tetragonally strained 2D layer, followed by a layer by layer growth for Si rich alloys and by island formation for Ge rich alloys. Strain relaxation is obtained via plastic or elastic strain relaxation, respectively.

than the Si(001) one. Assuming that the epilayer is much thinner than the substrate, the Ge (or SiGe) cubic unit cell is tetragonally deformed, in order to match the Si lattice constants in the two orthogonal in-plane directions. In the attempt to preserve the unit cell volume, the lattice constant perpendicular to free surface is expanded with respect to the equilibrium value. As a consequence, this Ge (or SiGe) layer is biaxially compressed inside the growth plane and undergoes a tensile deformation in the direction perpendicular to the exposed surface, as indicated by the red and blue arrows in Fig. 2.2(a). As the epilayer thickness grows, the elastic energy stored in system linearly increases with it. The deposition of Si rich $Si_{1-x}Ge_x$ (x > 0.2-0.3) alloys proceeds with a layer by layer growth and the elastic energy stored in the system is relaxed via the formation of interfacial defects, such as misfit dislocations, see Fig. 2.2(c). On the contrary, the deposition of Ge or Ge rich $Si_{1-x}Ge_x$ alloys follows the SK growth modality and, on top of a thin tetragonally strained wetting layer, 3D island formation is observed so as to elastically relieve part of the misfit strain, see Fig. 2.2(b). Between low-mismatched and high-mismatched regimes, there are important differences both in the morphology and in the strain relaxation process, which in part are due to surface roughness and 3D structures formation during the heteroepitaxial growth of highly mismatched layers. In the next sections we will describe the competitive plastic and elastic strain relaxation mechanisms in these two regimes.

2.4 Plastic relaxation and 2D layer growth

In low mismatched heteroepitaxial systems ($f < 1\%$), as Si rich Si-Ge alloys grown on Si(001), a defect free pseudomorphic (or coherent) 2D layer is initially formed. Such an epitaxial layer exhibits an in-plane lattice constant which is equal to the substrate one. The layer is biaxially compressed and the in-plane strain $\varepsilon_{\parallel}$ is given by the lattice mismatch between the substrate and the epilayer material: $\varepsilon_{\parallel} = f$. Since there is no constraint in the direction perpendicular to free surface, the pseudomorphic layer is tetragonally distorted

and the out-of-plane strain component $\varepsilon_{\perp}$ has an opposite sign with respect to $\varepsilon_{\parallel}$. As the film thickness increases, the elastic energy stored in the system also increases, and beyond a critical value, it becomes energetically favorable to introduce misfit dislocations at the interface, that reduce the in-plane strain. This value is called the critical film thickness h_c. Beyond the critical thickness, part of the strain is accommodated thanks to the formation of dislocations and their motion in the epilayer (plastic relaxation process). The residual in-plane strain component can be written as:

$$\varepsilon_{\parallel} = f - \delta \tag{2.4}$$

where δ is the plastic strain induce by the misfit dislocations microstructure in the in-plane directions. If δ is different from zero, there exist at the interface misfit dislocations with an average spacing of:

$$S = b_{eff}/\delta \tag{2.5}$$

where b_{eff} is the effective Burgers vector, i. e. the interface plane component of the Burgers vector in the direction perpendicular to the misfit dislocation lines, as explained in the paragraph below. These two quantities are generally dependent on the initial misfit f and on the layer thickness h. Kinetic limitations may prevent or delay the formation of misfit dislocations, in this case coherent metastable films can be obtained.

In highly mismatched heteroepitaxial systems, the planar surface of the highly stressed epilayer is unstable to the formation of undulations. This is because the energy reduction associated with elastic relaxation induced by the surface roughening exceeds the increase in energy due the extra surface exposed. The instability of the surface of a solid under stress is known as the Asaro Tiller and Grienfield (ATG) instability [16, 17]. The ATG instability occurs at moderate and high Ge concentration, hindering the layer by layer growth and eventually resulting in the SK growth. The critical misfit for island formation in the SiGe/Si(001) is $\sim 1\%$ equivalent to an average Ge concentration in the Si-Ge alloy of 0.2. [18]. However at large deposition volumes, islands coalesce and thick Ge rich films are formed. In such systems, the elastic relaxation provided by surface corrugation or island nucleation is not sufficient to relieve the in-plane deformation in the entire film volume. Also several growth methods have been developed that inhibit island growth, thanks to the use of surfactants such as hydrogen during the deposition process [19], and allow for high misfit 2D film formation. Hence also in Ge rich 2D layers plastic relaxation occurs and influence the morphology of the growing epilayer structure.

2.4.1 Dislocations

Dislocations are crystallographic line defects that induce a lattice deformation that depends on the dislocation line position and on the Burgers vector. In heteroepitaxy, dislocations are formed in order to relax the misfit strain. In Fig. 2.3 an edge (a) and a screw (b) dislocations lying at the interface between two mismatched materials are sketched. Here the epilayer has a larger lattice parameter than the substrate one, as for the SiGe/Si(001) system. From Fig. 2.3, it is clear that the edge dislocation having $\boldsymbol{b}$ parallel to the interface (a), induce a displacement of the atoms parallel to $\boldsymbol{b}$ and equivalent to the removal of an half-plane of atoms. Hence a tensile strain parallel to $\boldsymbol{b}$ is induced by the edge

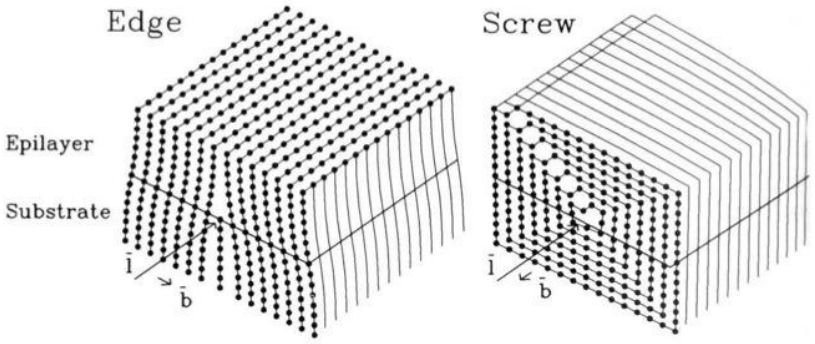

FIGURE 2.3: Illustration of an edge (a) and screw (b) dislocation at the interface between the substrate and the epilayer.

dislocations in the epilayer, that partially relieve the in-plane compression in the direction perpendicular to the dislocation line. On the contrary, the deformation induced by a screw dislocation does not modify the in-plane lattice parameter of the epitaxial layer and it does not help in relieving the in-plane compression. We notice that the strain relaxation efficiency of the edge dislocation shown in 2.3(a) is directly related to the orientation of its Burgers vector. In particular, the maximum efficiency in the strain relaxation of the epilayer is found when an edge dislocation is produced at the interface and its Burgers vector also lie in the interface plane. In this case a plastic strain equal to b is induced in each plane of the epilayer. Considering the more general case of a mixed dislocation lying at the interface with an arbitrary Burgers vector, the efficiency of such a defect in relieving the misfit strain can be quantified, evaluating the effective Burgers vector b_{eff}, which is the projection of the Burgers vector in the direction perpendicular to the dislocation line in the interface plane:

$$b_{eff} = b \cos\beta \cos\theta \,, \tag{2.6}$$

where β is the angle between the misfit dislocation line and its Burgers vector and θ is the angle between its Burgers vector and a line in the interface drawn perpendicular to the dislocation line direction.

In heteroepitaxial Si-Ge structures grown on Si (001) interfacial dislocations are observed along the [110] and the $[\bar{1}10]$ directions. In particular two kinds of them are typically recognized in experiments: the 60°and the edge, or 90°, dislocations. 60°dislocations are the most commonly observed ones, especially in low misfit SiGe films, and are the favorite ones, since they can glide on the low energy $\{111\}$ glide planes. Their Burgers vectors lie in one of $\{111\}$ planes parallel to one of the $\langle 110\rangle$ directions, so that their effective Burgers vector is $b_{eff} = b/2$. 90°dislocations are more efficient in relieving the interfacial strain, since their Burgers vector lie in the (001) glide plane, i.e. the interface plane, perpendicular to the dislocation line ($b_{eff} = b$). They are typically observed in high-mismatched SiGe films and they are probably formed by reaction of two misfit dislocations. Their formation is still debated in literature, since they cannot nucleate and propagate easily by glide motion in the (001) slip plane.

Most of the dislocations are located at the interface between the epitaxial film and the substrate, so as to relax the maximum in-plane strain. These defect lines are called misfit dislocations (MD). Still, dislocations cannot terminate at perfect crystal positions. As a consequence, a certain density of dislocations crossing the film volume and connecting the misfit dislocation segments to the surface are observed. These are called threading dislocations (TD). Since dislocations can degrade the performances of devices built using semiconductor heteroepitaxial layers, a lot of effort has been devoted to determine both the thermodynamic and the kinetic conditions at which misfit dislocations form.

2.4.2 Critical film thickness

Early theoretical works by Frank and van der Merwe, elucidate the film growth process and evaluated the thermodynamic critical thickness h_c for misfit dislocation formation in lattice-mismatched hetero-epitaxial films [20, 21]. In this work, they predicted h_c on the basis of elastic energy minimization. This model was then modified and applied to the diamond structure in low lattice mismatch systems such as SiGe/Si [22, 23]. A similar approach has been followed by several authors to determine h_c for different material systems and mismatch values. Here we report the results obtained by Matthews [24], where the energy of a coherent uniformly strained film and the energy associated with a misfit dislocation array with a regular spacing were calculated as a function of the layer thickness. The h_c value is obtained when the energy cost associated with such crystal defects formation is equal to energy gain due to the strain reduction in the layer induced by the dislocations. This leads to the following equation of the critical thickness h_c:

$$h_c = \frac{b(1-\nu\cos^2\beta)}{8\pi|f|(1+\nu)\cos\theta}[\ln\frac{h_c}{b}+1] \tag{2.7}$$

where β is the angle between the misfit dislocation line and its Burgers vector, θ is the angle between its Burgers vector and a line in the interface drawn perpendicular to the dislocation line direction, ν is the Poisson's ratio and $f = \varepsilon_{\parallel}$ is the misfit strain. Adapting Eq. 2.7 to (001) SiGe films, it is assumed that $\cos\beta = \cos\theta = 1/2$, $b = a_{SiGe}/\sqrt{2}$, corresponding to the Burgers vector for a 60°dislocation on $a/2\langle 110\rangle\{111\}$ slip systems. The critical thickness obtained by using Eq. 2.7 is plotted in Fig. 2.5 as a function of the misfit f, by assuming b=4 Åand ν=0.33.

An other simple and helpful model, developed by Matthews and Blakeslee [26] and widely used to study plastic relaxation in mismatched epitaxial systems, is based on a force balance instead of the aforementioned energy balance. Here it is assumed that a pre-existing threading dislocation that cross the film connecting the interface to the surface, as shown by the segment in Fig. 2.4(a), can bend (Fig. 2.4(b)) and move under the applied stress field depositing a misfit dislocation segment at the film/substrate interface once the critical layer thickness h_c is exceeded (Fig. 2.4(c)). Two forces act on the dislocation. The first is caused by the epitaxial stress field F_E, and this contribution drives the motion of the threading dislocation so as to elongate the misfit segment length and promote the plastic relaxation. On the contrary, the line tension contribution F_L opposes to such a motion, taking into account the additional crystal deformation associated with the misfit

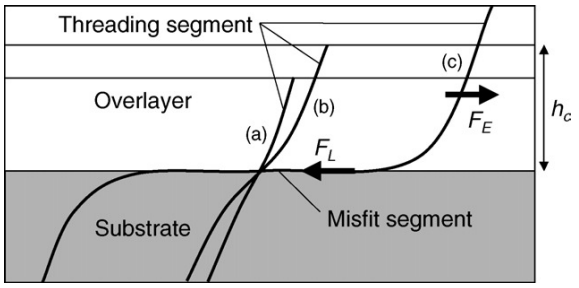

FIGURE 2.4: Schematic illustration of the Matthews and Blakeslee model of critical thickness. A pre-existing threading dislocation in a coherent interface (a); critical interface (b), and incoherent interface. Critical thickness h_c is determined by the equality of the force exerted in the dislocation line by misfit stress F_E and the line tension in the dislocation line F_L. [25]

segment extension. For a given misfit value f, the layer thickness at which the two forces are equal is h_c. For $h < h_c$, the line tension contribution dominates and the threading segment is immobile, as shown in Fig. 2.4(a). By increasing the film thickness to $h > h_c$ the elastic energy budget in the system increases and the force F_E induced by strain field overcomes the F_L contribution. As a consequence the threading dislocation propagates in the epitaxial layer progressively elongating the misfit dislocation segment deposited at the interface and relieving the in-plane strain, as shown in Fig. 2.4(c).
This force balance model is essentially equivalent to the energy balance model. In fact, the expression for h_c as a function of f turned out to be exactly the same as in Eq. 2.7. Moreover, this model explains how the plastic strain relaxation in epitaxial layers proceeds. In an overcritical film ($h > h_c$), once a certain density of threading segments are formed, independently of how they are nucleated (e. g. from the interface, surface, or defects, etc...), their motion leads to the formation of long misfit segments at the interface and progressively promotes the layer strain relaxation. This process continues until the in-plane strain in the film is reduced to a critical value, referred as channeling strain ε_{ch}. This is found when the total force acting on the threading segments in the epilayer is null. The residual strain in a film with a thickness h is then equal to such ε_{ch} value, that can be obtained by inverting Eq. 2.7:

$$\varepsilon_{ch} = \frac{b(1 - \nu \cos^2 \beta)}{8\pi h(1 + \nu) \cos \theta} [\ln \frac{h}{b} + 1] \, . \tag{2.8}$$

Obviously, this model depicts a simplified scenario. In fact, threading dislocations can interact or react with each others or can be stopped by other obstacles, as planar or point defects, or in presence of local fluctuations in the stress field. Also the nucleation of dislocations, which is still debated in literature, may limit the strain relaxation process and metastable coherent films or partially relaxed layers with a residual strain larger than the predicted ε_{ch} value can be produced.

In literature, experimental works of MBE deposition of SiGe films on Si(001) substrates, conducted at a growth temperature of 550°C [27, 28], reported significantly larger critical thicknesses than the h_c values predicted by Eq. 2.7. In an attempt to explain this discrepancy, People and Bean developed an alternative expression for h_c by taking

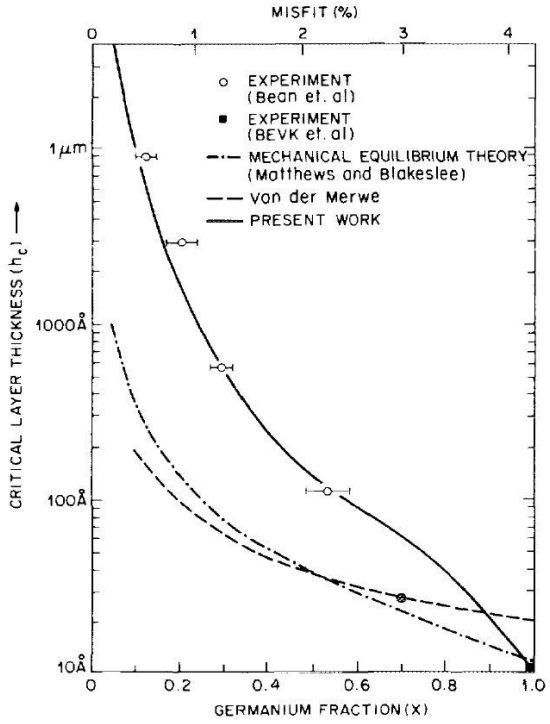

FIGURE 2.5: Critical layer thickness h_c versus lattice mismatch strain f. [33]

into account the extra energy required for the generation of a regularly spaced misfit dislocation network. The critical thickness, as a function of the misfit f, was calculated by equating the areal energy density of pseudomorphic layer with the one of a dense network of misfit dislocations at the interface. Dislocations were assumed to have screw character and a uniform spacing $S = 2\sqrt{2}a$. Although this model is in good agreement with the critical thickness measured for the $Si_{1-x}Ge_x$/Si(001) heteroepitaxial system by Bean et al. [27] and by Bevk et al. [29], their interpretation depends on their rather ad hoc estimation of the energy of the misfit dislocation array, assumed to have a fixed spacing S. The dominant reason causing the discrepancy between theory and experiments seems to be the non-equilibrium growth conditions for strain-relaxed SiGe films. In fact, such experimental data were measured after the deposition of SiGe films at low growth temperatures, suggesting that such SiGe layers are metastable. On the contrary, high temperature (900°C) post-growth annealing of SiGe films grown at 500–600°C [30, 31], rapid-thermal CVD deposition experiments at 900°C [32] or SiGe growth by an UHV evaporation technique at 750°C, are few examples that lead to excellent agreement of the experimental critical thickness with the predicted h_c values of the Matthews and Blakeslee model, as shown in Fig. 2.5. The latter is in agreement with most of the experimental results in literature and it is the most widely accepted model for the thermodynamic critical layer thickness of dislocation formation.

In general, kinetic effects such as the energy barrier for the formation or motion of misfit dislocations give rise to non-equilibrium behavior and deviations from the Matthews and

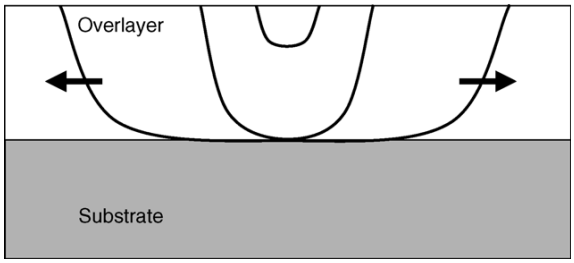

FIGURE 2.6: Sketch of the nucleation of a dislocation half-loop at the surface. The loop expands and thanks to the lateral motion of the threading dislocations a misfit segment is deposited at the interface. [25]

Blakeslee predictions. An early attempt to describe the influence of kinetics on the critical thickness was proposed by Matthews et al. [34], where they included in the force balance derived in Ref. [26] an additional term opposing to the dislocation motion which takes into account the lattice friction, known in literature as the Peierls stress [3], which is typically large in crystals with the diamond structure. An other example of a kinetic model taking into account the activated nucleation and propagation of dislocations was proposed by Dodson and Tsao [35, 36], obtaining results in remarkable agreement with the previous experimental data [22, 27]. However, kinetic effects are strongly related to the peculiar growth condition (e.g. temperature, growth rate, initial dislocation or other defect density) and all of them significantly affect the final strain state and morphology making reliable predictions very challenging. Still, the models presented capture the essential features of 2D layers relaxation process and remain useful to predict the thermodynamic or kinetic limit for the plastic relaxation onset. In the next paragraph we will briefly describe the nucleation and propagation of dislocations in epitaxial layers, discussing the conditions and factors that may enhance or hinder these two processes.

2.4.3 Dislocation nucleation mechanisms

The model of Matthews and Blackeslee relies on the assumption that pre-exhisting dislocations coming from the substrate can bend and propagate so as to promote plastic relaxation. This mechanism, however, it is not sufficient to explain the large density of dislocation typically observed in films, considering that substrates with a very low defect density are available. Hence nucleation of new dislocations during the growth must take place. The detailed nucleation mechanisms of misfit dislocation in heteroepitaxial systems are still controversial and currently object of study. In general two mechanisms can be distinguished: the homogeneous and the heterogeneous dislocation nucleation.

Homogeneous nucleation consists in the formation of a dislocation half-loop at the surface [24, 37]. This mechanism is illustrated in Fig. 2.6. A small half-loop is created at the epilayer surface; the loop glides towards the interface and a misfit segment is deposited at the interface and two threading segments are associated with it. In particular, in a reference stress field there exists a critical radius R_c, above which the loop continues to expand untill it reaches the interface. Then, the two TDs move apart depositing a misfit segment

and lengthen it, promoting further strain relaxation. On the contrary, subcritical half-loops will shrink and self-annihilate. Matthews calculated R_c as a function of the misfit strain between film and substrate in Ref. [24]. In the simplest approximation (neglecting the extra energy for the surface step created by the dislocation loop), by considering the dislocation line energy and the strain energy released by a perfect dislocation half loop formation and by minimizing it with respect to R_c, he found:

$$R_c = \frac{b(1-\nu\cos^2\beta)}{8\pi|f|(1+\nu)\cos\theta}[\ln\frac{h_c}{b}+1]\frac{1}{\sin\phi}\ , \tag{2.9}$$

that by looking at Eq. 2.7, can be rewritten as:

$$R_c = h_c/\sin\phi\ , \tag{2.10}$$

where ϕ is the angle between the glide plane and the (001) interface plane. It means that, the critical radius for half-loop formation is related to the critical film thickness h_c by a simple geometrical relation. In fact, h_c is found by projecting the critical radius calculated in the dislocation glide plane into the plane perpendicular to the free surface and containing the misfit segment at the interface. The activation energy for half-loop nucleation may be determined by the energy required to form a half loop with radius R_c. By looking at Eq. 2.9, it is clear that the larger the misfit strain f the smaller is the critical loop radius R_c. The activation barrier for homogeneous nucleation is then expected to decrease with the misfit strain (i.e. with the Ge content in SiGe films). This trend has been shown by Hull et al. in Ref [38], where the energy of dislocation half-loops was calculated for SiGe/Si(0 0 1) systems.

Heterogeneous nucleation consists in dislocation formation at an existing heterogeneity or defect in the film. The local stress field induced by such a defect can lower the energy required to form a dislocation loop or half-loop. In low misfit film, where the energy barrier for homogeneous nucleation is high, any defects, starting from surface steps or cusps, to precipitates or stacking fault regions, could be possible dislocation sources. Therefore, homogeneous nucleation of half-loops is physically justified at moderate and high mismatches, while heterogeneities play a significant role in the dislocation nucleation mechanisms at low mismatch [39]. Among the possible defects, the presence of defects or roughness at the surface plays a crucial role in the dislocation nucleation. Local stress concentrations at surface cusps or defects may lead to barrierless nucleation of dislocation half-loops [38, 40, 41]. In some cases, dislocations are found as a result of island coalescence at the position where the different islands merge.

In the final stage of 2D layer strain relaxation, when a large density dislocations is present, dislocation interact and react with each other and, from the interaction between different misfit and threading dislocations, multiplication events can occur. So far, several mechanisms for dislocation multiplication have been proposed, as the Hagen–Strunk sources [42], the Frank–Read sources [43–45], cross-slip and pinning [46, 47]. As we have seen in this paragraph, dislocation nucleation is governed by many factors, that affect the whole plastic relaxation process and dislocation nucleation is still a crucial issue to understand and govern the growth and relaxation of 2D SiGe films.

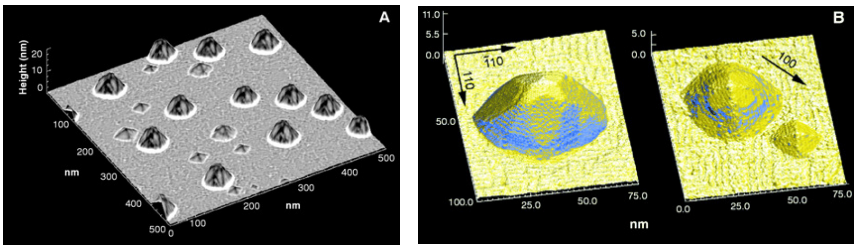

FIGURE 2.7: (a) STM topograph of strained Ge nanocrystals on Si(001), showing both pyramids and domes. (b) Higher magnification images of the nanocrystals: (left) a mature dome and (right) a nanocrystal entering the transition stage and a small pyramid. [53]

2.5 Elastic relaxation and 3D nanoisland formation

The deposition of Ge on Si(001) is known to result in self-assembled nanoisland formation following the Stranski-Krastanow growth mode. An example of SiGe islands on Si(001) is shown in Fig. 2.7. The first evidence of island formation in the Ge/Si(001) system was found more than 30 years ago [48, 49] and a huge number of works followed it in order to understand this growth modality and to exploit such self-assembled nanometric islands for different applications. Several reviews collected the main findings in this field [50–52] and reported a large variety of island morphologies.

Ge deposition results in the initial formation of a uniformly strained wetting layer (WL), that grows pseudomorphically up to a thickness of 3-4 monolayers (ML). Then, the growth continues with the transition from 2D layer by layer growth to 3D nanoislands formation. The initial WL is produced by the lower surface energy of Ge with respect to Si, which converges to bulk values in three to four monolayers (ML) [54, 55]. Whereas, 3D coherent islands formation on top of it, is driven by the thermodynamic. The formation of 3D structures is an attempt to recover the bulk in-plane Ge lattice parameter and allowing for a better elastic energy relaxation. It is clear that different island shapes relax differently the epitaxial strain, steep islands are generally more efficient than shallow ones. This is confirmed by the observed experimental trend, as shown in Fig. 2.8, where the island aspect ratio (AR), defined as the ratio between the height h and square root of the basal area B_{is}, $AR = h/\sqrt{B_{is}}$, is plotted as a function of the island volume V. The increase of coherent island AR with V is evident by looking at Fig. 2.8.
In literature, several island morphologies have been observed. At the early stages of Ge deposition very shallow islands (AR lower the 0.1) called prepyramids or *mounds* have been observed [56]. Proceeding with the deposition, prepyramids transform into huts (truncated pyramids with rectangular base) or square based pyramids, both bounded by {105} facets (AR=0.1) [48, 53]. In general, huts are observed at low growth temperatures and growth rates, while pyramids are found at higher growth temperatures. With the increasing Ge deposition volume, {105} pyramids evolve into steeper multifaceted islands called *domes* [53, 57], as shown in Fig. 2.7. Such islands are characterized by the appearance of {113} and {15 3 23} facets and by AR=0.22-0.26. A third island morphology, called *barn*, characterized by {111} facets in addition to the ones observed in domes and by higher

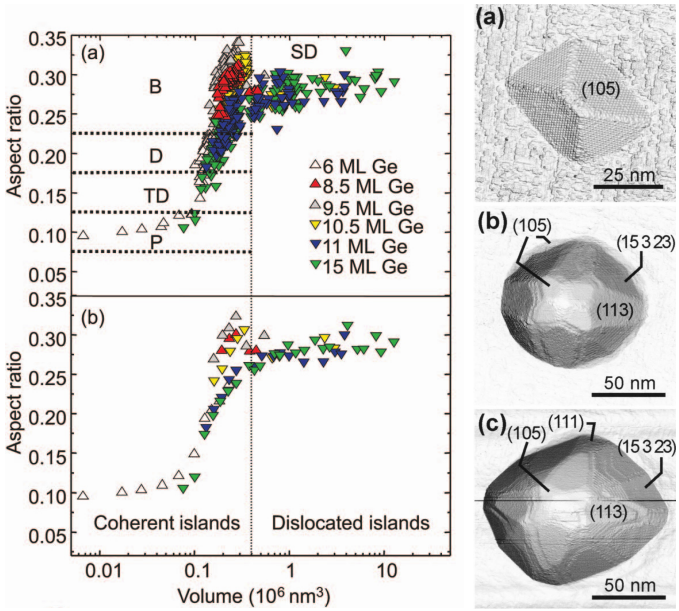

FIGURE 2.8: Left:(a) Evolution of the island aspect ratio versus volume for different samples with Ge coverages varying between 6 and 15 ML. The line marks the critical volume for dislocation in- troduction at 700 °C. (b) Average aspect ratio values for islands having similar volumes vs volume. [58] Rigth: Top-view STM images of coherent $Si_{1-x}Ge_x$ islands on Si(001). Gray scale in the images encodes local slope on the surface. (a) *Hut*. (b) *Dome*. (c) *Barn*. Families of facets bounding these island shapes are labeled. [59]

AR=0.26-0.33 is also observed [58, 59]. Finally, large plastically relaxed islands, called *superdomes*, are formed [60]. These evolve cyclically [61], maintaing on average a constant AR, as shown in Fig. 2.8.

The morphological evolution of coherent islands, relies on the delicate balance between the decreased elastic load for steeper islands and the higher surface energy caused by the increased surface to volume ratio. A simple model based on thermodynamic arguments can explain the morphological evolution of the islands with deposition (i.e. volume). The stability of SiGe islands on Si(001) can be explained by considering the variation of the elastic energy density stored in the island and of the surface energy with respect to the WL [52]. In particular, assuming that the wetting layer critical thickness for island formation is reached ($h \gtrsim 3$ ML, as shown in Ref. [18, 62]), for a fixed island shape and for a given volume V, the total energy difference between the island configuration and an additional flat layer on the WL can be written as:

$$\Delta E = E_{is} - E_{WL} = (\rho_{is} - \rho_{WL})\, V + \gamma_{is}\, c_s\, V^{2/3} - \gamma_{WL}\, c_b\, V^{2/3}\,. \tag{2.11}$$

In equation 2.11, the first term takes into account the elastic relaxation gained by the island formation, which scales linearly with V, being ρ_{is} and ρ_{WL} the elastic energy densities in the island and in the WL. The last two terms quantify the energy increase caused by the exposed island free surface and the energy gain due to the covering of the WL surface by the island base, which are both proportional to $V^{2/3}$. Here γ_{is} and γ_{WL} are the surface

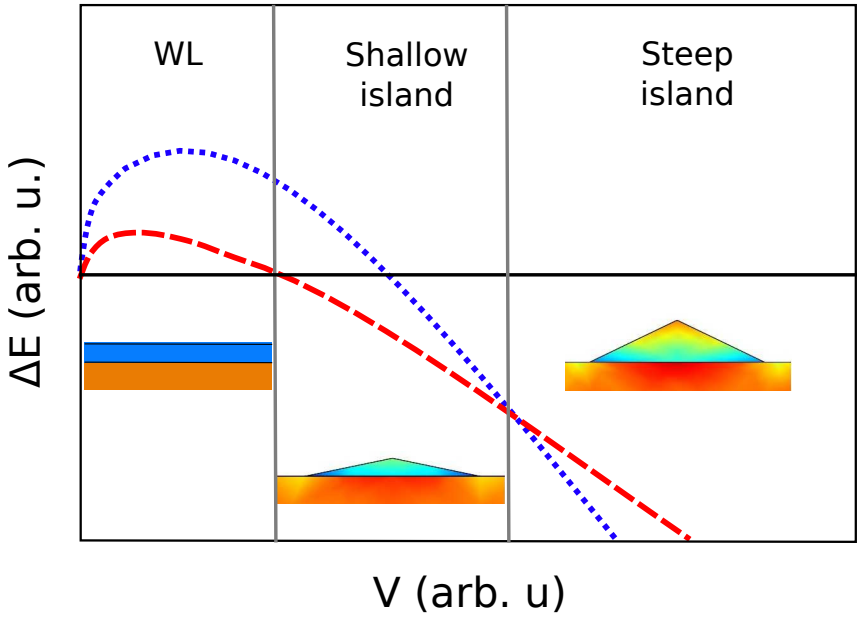

FIGURE 2.9: Energy difference between the WL and a shallow (full line) a steep island (dashed line), as a function of the Ge volume.

energy density of the WL and of the island and c_s and c_a are geometrical parameters depending only on the island shape, such that $c_s = S_{is}/V_{is}^{2/3}$ and $c_b = B_{is}/V_{is}^{2/3}$, where S_{is} is the island free surface and B_{is} represents the area of the WL covered by the island basis. In Fig. 2.9, a typical plot representing the energy variation expressed in Eq. 2.11 for a shallow and a steep island is shown. This graph illustrates that, initially the surface term dominates and the wetting layer is more stable than any island. With the increasing volume, the volumetric term associated with the elastic energy relaxation becomes more and more important favoring shallow islands, first, and steep islands formation.
Actually a continuous evolution of islands AR as function of their volumes is observed experimentally, that reflects the fact that the island facets may assume different extension leading to a slightly different island morphology. An analytical solution based on Eq. 2.11 was used to explain such progressive variation of the AR with volume in an idealized two-dimensional case, [63] and extended for realistically shaped islands to give a more quantitative predictions, that can be useful for the interpretation of the experimental results in Ref. [64].

2.5.1 Si-Ge alloying

Even in the case of nominally-pure Ge deposition on Si(001), Ge-Si alloying occurs from the very beginning of the the growth. In fact, the Ge composition of the wetting layer was found to be lower than 1, reaching values ∼0.8, as shown by recent photoluminescence experiments [66]. The Si-Ge intermixing process becomes even more significant during island formation leading to a Ge content in the island significantly smaller than 1. The incorporation of Si into islands is promoted by the presence of trenches around the island

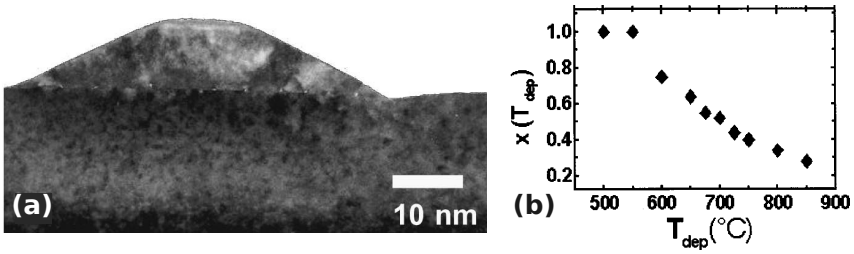

FIGURE 2.10: (a) TEM cross section of a dome grown at 600°C. (b) Ge average content x in the epilayer as a function of the growth temperatureT_{dep}. [65]

perimeter, as shown at the border of SiGe islands in the cross section TEM image of Fig. 2.10(a). In fact, the island growth towards high AR is accompanied by the formation of trenches carved in the WL and in the substrate in correspondence of the island edges [67]. This allows for a partial strain relaxation along the island basal border, where a large compressive strain is induced by the bending of the island. As a second effect, Si atoms can diffuse at the surface and mix with Ge atoms [68]. During the island growth these trenches evolve with the islands, moving laterally with the increasing island base and augmenting their depth, continuously providing Si atoms for the intermixing process. Si incorporation in islands is driven, first, by the entropy of mixing that leads to alloy Si and Ge and second, by the elastic energy minimization [69]. In fact, the island enrichment in Si results in a lower mismatch between the island and the substrate.
The extent of the Si-Ge alloying process is known to increase with temperature [70, 71]. Thus, the average island Ge content decreases with the growth temperature T_g [65, 72, 73], as shown in Fig. 2.10(b) where the Ge concentration in SiGe islands is plotted as a function of the deposition temperature of Ge/Si(001). This alloying process is a competitive strain relaxation mechanism. In fact, the island enrichment in Si results in a island lattice parameter smaller than the Ge one and closer to the Si bulk value, causing the reduction of the lattice mismatch and of the elastic budget stored in the island. This, in turn, influences the evolution of islands, delaying the transition from shallow to steep island morphologies (as the pyramid to dome transition) [65, 74] and the critical dimension for the onset of plastic relaxation [75], as discussed in the following paragraph.

Si-Ge exchange process can also produce a non homogeneous Ge composition profile inside islands. In particular, partial segregation of Ge at the island surface has been observed and predicted [69, 76]. However, variation in the composition profile are small (variation $<$ than the 10% in composition have been measured across the island profile) and in most cases it is reasonable to assume an unifrom Ge distribution inside SiGe islands.

2.5.2 Plastic relaxation

SK growth allows to partially relieve the misfit strain in Ge islands by elastic relaxation. However, at large deposition volumes, plastic relaxation becomes a competitive strain relaxation mechanism also in 3D islands. By looking at island AR vs. V plot in Fig. 2.8, we can clearly distinguish between two regimes. The first, at relatively small V, represents

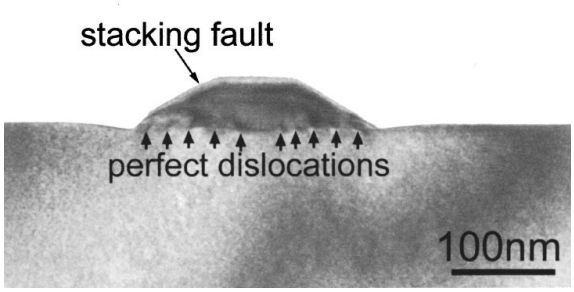

FIGURE 2.11: TEM image of a SiGe islands showing an array of perfect dislcoations at SiGe/Si(001) interface. [77]

the coherent island evolution, where island AR increases almost linearly with the volume. Whereas, the second one, shows the evolution of plastically relaxed islands. The volume at which the transition between these two regimes is observed is called critical island volume V_c. As we have seen for films, the introduction of a misfit dislocation introduces a in-plane deformation equal to b_{eff} (see Eq. 2.6) that allows for further strain relaxation (in addition to the elastic one). The most commonly observed dislocations in SiGe islands, as for films, are the 60°dislocations, especially at high growth temperatures [78]. In Fig. 2.11, a cross-section TEM image of a SiGe islands with an array of 60°dislocations is shown. These defects are believed to nucleate from the island surface, at the positions where the stress is maximum, and glide in the {111} planes depositing a straight misfit segment along the [110] or [$\bar{1}$10] direction. Several theoretical models have been developed in order to study the interaction between dislocations and the epitaxial strain field of the island. In particular, 60°dislocations are expected to nucleate close to the island edges where the stress is maximum [63] and to segregate to one side of the island, allowing for a better strain relaxation [79]. In literature, only few models have been developed for the calculation of the critical volume V_C for dislocation formation. These are generally based on an energy balance between the energy cost E_{cost} for introducing a dislocation, which produces a deformation in the crystal, and the energy gain E_{gain} due to relaxation of the misfit strain induced by the dislocation itself. Also, they differ in the approximation of the island geometry and of the energy evaluation. The critical volume for the formation of a straight 60°dislocation segment V_C has been evaluated by considering 2D and simplified island shapes [63, 80, 81], or 3D realistic shaped islands [75, 82]. In particular, in Ref. [75] the equilibrium critical volume was calculated as a function of the average island Ge content x (which is known to depend on the growth temperature), showing that V_C augment with the decreasing island Ge concentration. The authors also compared their theoretical predictions with a set of deposition experiments of Ge/Si(001) at different temperatures, showing a remarkable agreement between experiments and results. This suggests that plastic relaxation in epitaxial islands does not present severe kinetic limitations as for 2D layers.

Several experiments have shown that plastic relaxation strongly influences the morphological evolution of islands. In-situ observations of Ge/Si(001) growth by using an ultra-high-vacuum transmission electron microscopy (UHV TEM) showed that plastically

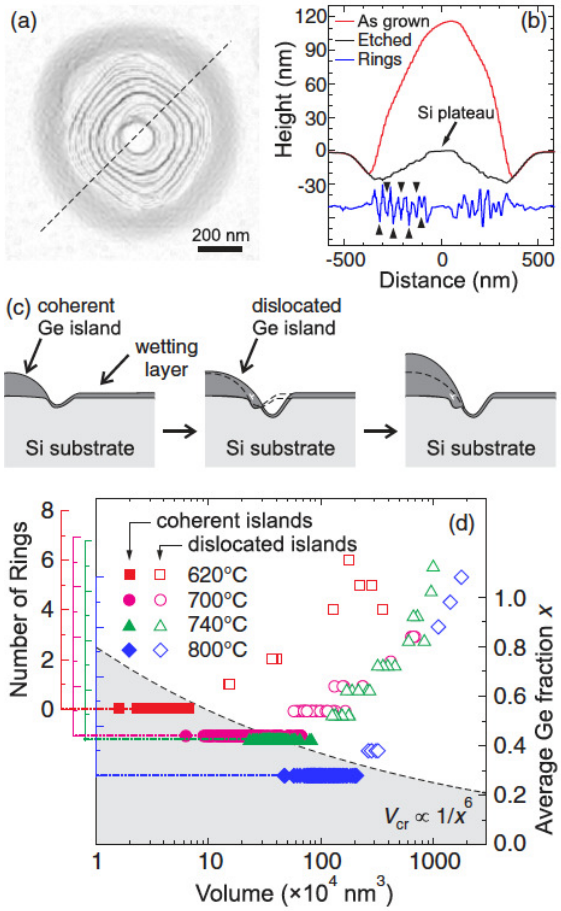

FIGURE 2.12: (a) AFM scan of the tree-ring structure left over by a single superdome (grown at 800 °C) after etching. (b) Cross-sectional profile of the same superdome before and after etching taken along the dashed line shown in (a). The bottommost curve represents the numerical second derivative (in arbitrary units) of the AFM topography of the profile after etching. The solid triangles indicate the position of the rings. (c) Schematic representation of the mechanism leading to the formation of ring structure. (d) Number of rings vs island volume for different temperatures. Note that the scatter plots of the number of rings are vertically shifted by a constant factor proportional to the estimated average Ge fraction x. [83]

relaxed islands evolve according to a cyclic growth mechanism [61, 78], that can be summarized as follows. When a dislocation nucleates, close to the island edges, the island expands rapidly in base by decreasing its AR and incorporating the dislocation into the island. Then, by incorporating new material, it slowly increases its volume recovering the original AR. As soon as a new dislocation is nucleated, the same process is repeated and continues cyclically during the island growth. In Ref. [84] a pattern of concentric 60 °dislocations is shown, that was probably produced by this cyclic mechanism. The oscillation in AR due to the periodic drop and the recovery of the island height, explains the almost constant AR value (~ 0.3), observed at large volumes in Fig. 2.8. Moreover, the cyclic growth guided by the periodic nucleation of dislocation segments, allows to interpret the results of selective etching experiments performed on SiGe islands on Si(001). The AFM analysis of the island footprints leaved on the substrate after the selective etching process, shows a tree-ring like structure at the position where large dislocated islands were grown [83], as shown in Fig. 2.12(a,b). The formation of such tree-ring structures is illustrated in Fig. 2.12(c). During the growth, islands carve trenches at the island edges (see Fig. 2.10). When a dislocation is nucleated in the island, a sudden and fast expansion of the island base at expense of its thickness is observed. As a consequence, the dislocation is incorporated in the island and the trench is covered. Then the island grows in height, recovering its original AR and carving new trenches around the larger base. When an other dislocation is nucleated the process is repeated, until a stepped profile is carved in the Si(001) substrate, as revealed by the experiments. In Fig. 2.12(d), are plotted the number of rings carved in the substrate as a function of the original island volumes. In agreement with the proposed mechanisms, the number of rings (i.e. dislocations) progressively increase with the island volume. Moreover, the higher the growth temperature the larger is the volume of dislocated islands, due to enhanced intermixing between Si and Ge.

In the experiments described above the observed dislocations are the 60°type. It is worth to mention, that 90°dislocations are also observed, generally at low growth temperatures [78]. In literature, the formation of this kind of defects is controversial. A possible mechanism is that at low growth temperature, islands are rich in Ge, and the high epitaxial misfit strain can induce the homogeneous nucleation of this dislocation directly at the interface. An other possible explanation is that during the coalescence of two neighboring islands a 90°dislocation can form at the interface at the position where the islands merge.

2.5.3 Island ordering

In the Ge/Si(001) system, a bimodal distribution in size is typically found, consisting of pyramids and dome-shaped islands [53, 57]. However, islands in controlled positions and with a narrow size distribution are desirable both for fundamental investigations and applications. Recently, it has been shown that the key to successfully create laterally ordered islands, is the growth on nanopatterns, which can provide preferential nucleation sites for the island growth. Several experimental techniques are available for patterning, including the Focus Ion Beam (FIB) manipulation,[85–87] and the nano-imprint, holographic, or electron-beam lithography assisted by reactive-ion etching.[88–92] Advancements in these techniques allowed for the creation of different patterns, characterized by periodic arrays

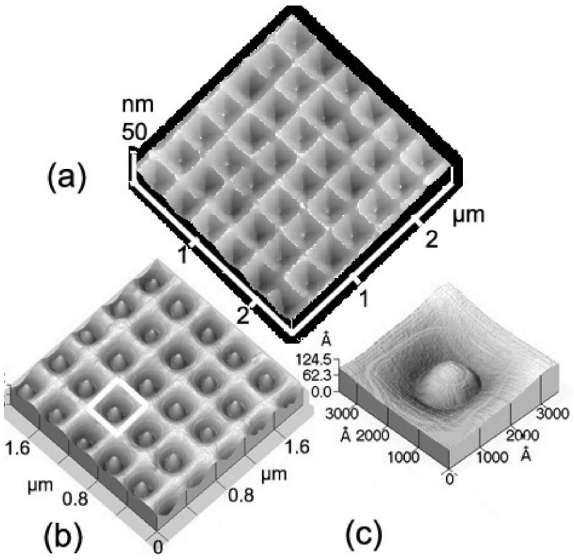

FIGURE 2.13: 3D topography of a patterned substrate (a) after Si buffer layer growth and (b) after deposition of 4ML of Ge. (c) Zoomed single island taken from (b).

of pits, trenches or mesa templates. Depending on the specific features of the pattern, islands nucleate at different positions. For example, in large shallow pits islands nucleate at the center of the pits [89], while they occur in between the pits for narrow FIB patterned pits [85]. Also, island formation on top of mesa structures or at the concave intersection between two neighboring mesas has been observed, depending on the size and the separation in the pattern [90, 91]. A particularly efficient pattern geometry consists in an ordered array of pits. Controlling the width, the depth and the separation of the pits, it is possible to induce preferential nucleation inside the pits, obtaining a high degree of island ordering [93] . Moreover, islanding on the terraces in between the pits can be avoided by suitably tuning the growth conditions. An example of Si(001) substrate patterned with a regular arrangement of pits, where islands are selectively nucleated inside the pits is shown in Fig. 2.13. The morphological evolution of islands nucleated in pits is similar to the one observed on flat Si substrates: {105} pyramids are found for low Ge deposition volume, which evolve in steeper islands with dome and barn shape at larger deposition volumes [94]. Interestingly, islands in pits are homogeneous in shape and size. In fact, a narrow size distribution is observed for islands grown on pit-patterned, compared to the typical spread in volumes reported for islands on flat Si(001) substrates [95]. Strain relaxation via Si-Ge intermixing, leading to a lower average Ge composition with the increasing T_g, and via dislocation nucleation is observed. Recent experimental evidence and preliminary calculations have shown that SiGe islands nucleating in shallow pits on Si(001) are more relaxed than on flat Si(001) [93, 96, 97]. Interestingly, such extra relaxation is expected to delay the onset of plasticity [93]. This aspect will be investigated in Chapter 2.5

2.6 Nanowire heterostructures

The last heteroepitaxial structures we study in this work are the nanowires (NWs). The growth of one-dimensional(1D) Si wires catalyzed by a liquid metal droplet has been demonstrated by Wagner et al. in the early 1960s, for structures with typical width in the micrometer scale called whiskers[98]. This growth method is well known as vapor-liquid-solid (VLS) technique and it is widely used to grow wires with typical width in the nanometer scale (< 50 nm) of a variety of semiconductor materials on different substrates and with different orientation. [99–102]. Togheter with the VLS synthesis, other growth techniques have been exploited, such as the growth on nano-patterned substrates to produce arrays of nanowires uniform in size and in ordered position, or the catalyst-free self-assembling to produce random arrays of wires. Here, the VLS mechanism and the two main wire "architectures", referred as axial and radial heterostructures, are briefly discussed and the Ge/Si core-shell nanowires, our system of interest, introduced. For more details about the various nanowires synthesis techniques and the progress made in this field see for example Ref. [103–105] and references therein.

2.6.1 Vapor Liquid Solid Growth Process

The Vapor Liquid Solid (VLS) mechanism is a widely used method to grow 1D structures which involves metal nanoparticles as catalysts to continuously supply material and favor the vertical growth. The mechanism was early proposed by Wagner & Ellis [98] and more extensively developed by Givargizov [106] and can be summarized in the following steps. First the metal nanoparticles are deposited on top of the substrate. The as-prepared sample is placed in a reaction chamber or tube and the temperature is increased until the particles melt forming a liquid droplet. Second, the gas precursors of the growth materials are injected into the reaction chamber. Since the sticking coefficient at the droplet surface is higher than the sticking coefficient at the substrate free surface, the atom precursors are deposited preferentially at the droplet surface and form a liquid alloy. The continuous incorporation of the semiconductor precursor leads to the supersaturation of this alloy component. As a consequence, the semiconductor component precipitates and the crystal growth starts at the solid-liquid interface leading to the wire formation, as sketched in Fig. 2.14(a,b). The lateral growth of the wire is typically limited by the size of the liquid droplet, while the orientation is not necessary perpendicular to the surface. For example, group IV and zincblende structure wires are preferentially oriented along the [111] direction, and wurzite wires along the [0001]. This synthesis process it is highly diffuse, because it is possible to grow a wide range of NW materials, from group IV, to III–V and II–V, and to select different substrate material and orientation. Moreover, this approach allows a precise control of the NW composition and dopants concentration, through fine control of the growth parameters.

2.6.2 Axial and Radial Nanowire Heterostructures

Another advantage of the VLS process is that, along with homogeneous single crystal wires, it is possible to grow heterostructures adding one or more layers of a second material axially

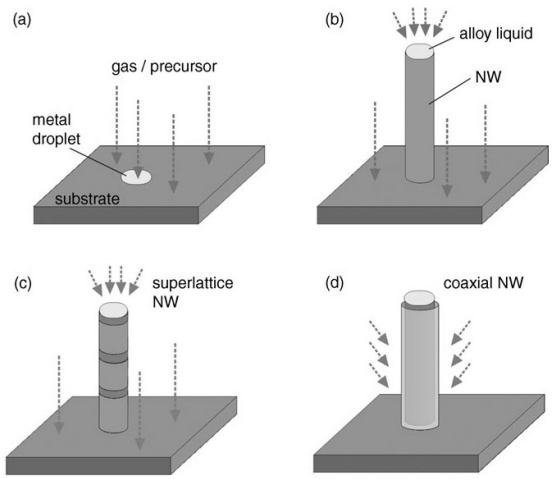

FIGURE 2.14: NWs of different structures based on the "bottom-up" growth mode: a) Exposure of a metal-droplet-coated substrate to reactant precursors; b) a monophase NW grown outwards, with the metal droplet acting as catalyst; c) a superlattice NW grown by consecutively alternating the reactant precursors; d) a coaxial NW formed by conformal coating of the preformed nanowire in (b) with a different material. [103]

or radially with respect to the initial NW, as shown respectively in Figs. 2.14 (c) and (d). This allows, for example, the fabrication of p-n junctions, perpendicular or parallel to wire axis direction. The synthesis of these structures is based on the control of radial versus axial growth. As we discussed in the previuos section the axial growth is achieved when the precursor decomposition and incorporation occurs at the nanoparticle site and not on the NW surface. Axial heterostructures are obtained by switching the material gas precursor and controlling the growth condition so that the deposition of the second material still occurs at the catalyst site. This operation can be repeated several times so as to form a superlattice NW, as shown in Fig. 2.14(c). On the contrary, by altering the growth condition it is possible to favor the deposition of the second material at the pre-existing NW surface (core) and to drive the conformal growth of a second component shell around the core, as shown in Fig. 2.14(d). Such structures are also called core-shell nanowires. NWs with the desired doping level in the subsequent layers are produced by the controlled introduction of reactants and dopants.

3

Dislocation Modelling in Nanostructures

Dislocations are complex objects, that induce a strong distortion of the atomic bondings close to dislocation line position, but they also produce a long range deformation field in the entire crystal. The latter is well described by linear elasticity theory. In this work we want to investigate plastic relaxation in epitaxial structures, such as thin film, nanoislands and nanowires. Even if we are dealing with nanostructures, the characteristic length of such systems can be as wide as tens or hundreds of nanometers. As a consequence, atomistic simulations are computationally too demanding in order to simulate such structures. Moreover, dislocation formation and propagation in heteroepitaxial systems is driven by the attempt to relax the epitaxial stress field. Therefore, an accurate description of the long range deformation field is needed to understand how these defects interact with each other and with structures under stress. For these reasons, we believe that continuum simulations are the appropriate tool to investigate plastic relaxation in such systems. One of the peculiarity of nanostructures, is the high surface to volume ratio, thus, the influence of the free surface on the elastic and plastic relaxation process cannot be neglected. In particular, an accurate description of the epitaxial stress field in nanostructures with multiple facets and the interaction of the dislocation stress field with it, is actually possible by using linear elasticity theory solved by finite element method. This method is the tool of choice for precise calculations of the elastic energy in elastically and plastically relaxed nanostructures. The second issue we need to address, is the dynamics of dislocations in the epitaxial nanostructures. To this aim, three-dimensional dislocation dynamics is the natural tool to access the evolution of a large density of dislocation lines. This simulation method is known to give accurate results in many problems of crystal plasticity. Moreover, the interaction of dislocations with the epitaxial field and with the free surfaces can be treated with suitable approximations that have been successfully tested for the plastic relaxation in micro and nanometer size objects.

In this Chapter, we first outline the definitions of linear elasticity theory necessary to describe the deformed state of epitaxial nanostructures and the analytical solution for the

stress field of a dislocation in bulk materials or semi-infinite solids. Then, we describe how to address elastic and plastic relaxation in nanostructures by using finite element method. Finally, we summarize the main features of the dislocation dynamics code employed (*microMegas*) and how we set up the simulations to tackle plastic relaxation in nanostructures. Also, we present a new stochastic procedure to handle the dislocation nucleation process that has been implemented in the dislocation dynamics code microMegas.

3.1 Linear elasticity theory framework

A solid body responds to an applied force by exhibiting a deformation. Linear elasticity theory provides a mathematical description of such deformations for a vast class of solids (linear elastic media), whose mechanical response is well described by a linear relation between stresses and strains. In this section are recalled the main concepts of linear elasticity theory that has been used throughout this work. For a more complete insight into linear elasticity theory, see for example Ref. [107, 108].

3.1.1 Displacement vector and strain tensor

Let $\{e_i\}_{i=1}^3$ be a set of three orthogonal unit vectors forming a coordinate system for the vector space Ω. The position of a material point inside a medium in the undeformed state is given by the vector $\boldsymbol{x} = x_i e_i$. If the medium considered undergoes a deformation the position in the deformed state is given by $\boldsymbol{x}' = x_i' e_i$. The dispacement produced by the deformation is then:

$$\boldsymbol{u} = \boldsymbol{x}' - \boldsymbol{x} \ . \tag{3.1}$$

The vector $\boldsymbol{u}$ is called the *displacement vector*. Since $\boldsymbol{u}(\boldsymbol{x})$ is defined at each point $\boldsymbol{x}$ in the domain Ω, it constitutes a vector field. In linear elasticity theory, the displacements and their derivatives are assumed to be small: $|\boldsymbol{u}| \ll 1$ and $|\nabla \boldsymbol{u}| \ll 1$.

Throughout this chapter, the convention of the repeated index has been adopted, i.e. any index which is repeated once in a product is assumed to be summed from 1 to the the number of dimensions N of the problem: $\boldsymbol{a} \cdot \boldsymbol{b} = a_i b_i = \sum_{i=1}^N a_i b_i$. Furthermore, the directional derivative of a given function f is written as $f_{,j} = \frac{\partial f}{\partial x_j}$.

A displacement field $\boldsymbol{u}(\boldsymbol{x}) \neq 0$ does not necessarily lead to deformation, as it can be related to rigid-body translation or rotations. A deformation results when the the relative positions between the points in Ω change. A Taylor expansion to the first order of the displacement fields leads to:

$$\begin{aligned} u_i(\boldsymbol{x}) &= u_i^0 + u_{i,j} dx_j \\ &= u_i^0 + \frac{1}{2}(u_{i,j} + u_{j,i}) dx_j + \frac{1}{2}(u_{i,j} - u_{j,i}) dx_j \\ &= u_i^0 + \varepsilon_{ij} dx_j + \omega_{ij} dx_j \end{aligned} \tag{3.2}$$

where we introduce the following definitions:

$$\varepsilon_{ij} = \ \tfrac{1}{2}(u_{i,j} + u_{j,i}) \tag{3.3}$$

$$\omega_{ij} = \ \tfrac{1}{2}(u_{i,j} - u_{j,i}) \tag{3.4}$$

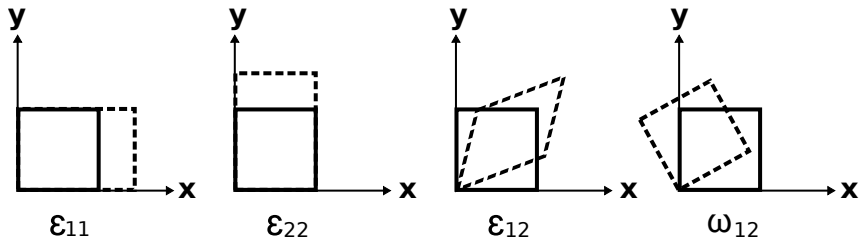

FIGURE 3.1: Illustration of the effect of the strain tensor and the rotation tensor components in a simplified 2D system.

ε_{ij} is the *strain tensor* and ω_{ij} is the *rotation tensor*. The strain tensor ε_{ij} is symmetric in the (i, j) indexes, while the rotation tensor ω_{ij} is antisymmetric, i.e. $\varepsilon_{ij} = \varepsilon_{ji}$ and $\omega_{ij} = -\omega_{ij}$. In the two dimensional case, strain and rotation can be easily represented as shown in Fig. 3.1, where the x and y directions are parallel to the e_1 and e_2 basis vectors. In this work, we will never have to deal with rotations of the body, so we will not investigate further the properties of ω_{ij}.

We notice that the ε_{ii} components represent the relative length change along the reference axis e_i of the chosen coordinate system, as illustrated in Fig. 3.1(a,b). On the contrary, each ε_{ij} strain tensor component with $i \neq j$ describes the shear deformation in the plane defined by the axis parallel to the basis vectors e_i and e_j, as shown in Fig. 3.1(c). In component-free notation, the strain tensor can be expressed as

$$\boldsymbol{\varepsilon} = \frac{1}{2}(\nabla \otimes \boldsymbol{u} + \boldsymbol{u} \otimes \nabla)\,. \tag{3.5}$$

The strain tensor can be decomposed in a traceless part and a multiple of the identity part,

$$\varepsilon_{ij} = \frac{1}{3}\mathrm{Tr}\,\boldsymbol{\varepsilon}\;\delta_{ij} + \left(\varepsilon_{ij} - \frac{1}{3}\mathrm{Tr}\,\boldsymbol{\varepsilon}\;\delta_{ij}\right)\,, \tag{3.6}$$

where δ_{ij} is the *Kronecker delta*. Since such decomposition is invariant under orthogonal transformations, it is independent of the choice of the basis set $\{e_i\}_{i=1}^{3}$. It is possible to demonstrate that only only the trace of $\boldsymbol{\varepsilon}$ (the first term of Eq. 3.6) is related to the local change of volume. In particular, if we consider an infinitesimal volume element dV prior to a deformation $\boldsymbol{\varepsilon}$, the final element volume dV' after the deformation is given by

$$dV' = dV(1 + \mathrm{Tr}\,\boldsymbol{\varepsilon}) = dV(1 + \varepsilon_{ii})\,. \tag{3.7}$$

Hence, the quantity $\mathrm{Tr}\,\boldsymbol{\varepsilon}$ represents the relative volume change of the infinitesimal volum element dV that undergoes a deformation $\boldsymbol{\varepsilon}$. We notice that in epitaxial thin films, the deformation is defined by only the diagonal part. Thus, in order to reduce such a deformation dislocations that induce a strain field with non zero ε_{ii} strain components are the one expected in the SiGe epilayer on Si.
On the other hand, the traceless part is called strain deviator tensor, and it is related to distortion.

3.1.2 Stress tensor

Another important tensor in elasticity theory is the stress field σ_{ij}, which is the force per unit area exerted on the i-th face in the j-th direction. The stress tensor field is related to the *traction force* $\boldsymbol{T}$ per unit area on any surface element with normal vector $\boldsymbol{n}$ as

$$T_i = \sigma_{ij} n_j \ . \tag{3.8}$$

In linear elasticity theory, it is assumed that the stress and strain tensor are related through the linear relation

$$\sigma_{ij} = C_{ijkl} \varepsilon_{kl} \ , \tag{3.9}$$

where C_{ijkl} are constants. The previous relation is the *elastic constitutive law*, and it is usually known as *generalized Hooke's law*. C_{ijkl} is called *elastic stiffness* tensor (briefly, stiffness tensor) and takes the elastic constants of the material as its components.

For a general anisotropic material, it is posssible to demonstrate that there are only 21 independent components out of the total 81 components, due to the symmetry of ε_{ij} and σ_{ij} and to thermodynamic reasons. However, real materials usually displays more symmetries, due to their crystalline structure, which further reduces the number of independent C_{ijkl} components. An interesting class of materials exhibits cubic symmetry, e.g. body-centered of face-centered cubic crystal structure. In presence of cubic symmetry, the number of independent components reduces drastically to 3,

$$C_{1111} = C_{2222} = C_{3333} \quad \equiv c_{11} \tag{3.10}$$

$$C_{1122} = C_{2233} = C_{3311} \quad \equiv c_{12} \tag{3.11}$$

$$C_{1212} = C_{1313} = C_{2323} \quad \equiv c_{44} \tag{3.12}$$

The elastic stiffness tensor can be inverted to give the *compliance tensor* S_{ijkl}, such that

$$\varepsilon_{ij} = S_{ijkl} \sigma_{kl} \ . \tag{3.13}$$

Isotropic continuos media

The simplest possible case is the one of an isotropic homogeneous continuous medium, i.e. all the directions are equivalent and the C_{ijkl} tensor is independent from the coordinates $\boldsymbol{x}$ of the point considered in the elastic medium. This is an important class of materials also because most of the analytical expressions derived in the classical dislocation theory to describe the dislocation stress field were obtained within the assumption of isotropic media, and are not available for a general anisotropic materials. For an isotropic material there exist only two independent components of elastic stiffness constants. In particular, the isotropic case can be treated as a cubic one, in which the elastic constant are constrained by

$$c_{11} = c_{12} + 2c_{44} \, . \tag{3.14}$$

In general, the Lamé constants λ and μ, also called *shear modulus*, are used:

$$\lambda \equiv c_{12} \qquad \mu \equiv c_{44} \ . \tag{3.15}$$

Furthermore, it follows that $c_{11} = \lambda + 2\mu$. Therefore, Eq. 3.9 can be rewritten for this important case as

$$\begin{aligned}
\sigma_{11} &= (\lambda + 2\mu)\varepsilon_{11} + \lambda\varepsilon_{22} + \lambda\varepsilon_{33} \\
\sigma_{22} &= \lambda\varepsilon_{11} + (\lambda + 2\mu)\varepsilon_{22} + \lambda\varepsilon_{33} \\
\sigma_{33} &= \lambda\varepsilon_{11} + \lambda\varepsilon_{22} + (\lambda + 2\mu)\varepsilon_{33} \\
\sigma_{12} &= \mu\varepsilon_{12} \\
\sigma_{23} &= \mu\varepsilon_{23} \\
\sigma_{13} &= \mu\varepsilon_{13}
\end{aligned} \tag{3.16}$$

Instead of the Lamé constants, two other quantities can be used to described isotropic materials, the *Young's modulus* Y and the *Poisson's ratio* ν, which can be expressed through the following relations:

$$\lambda = \frac{\nu Y}{(1+\nu)(1-2\nu)} \qquad \mu = \frac{Y}{2(1+\nu)} \; . \tag{3.17}$$

Let us consider the simple case of a isotropic homegeneous medium that undergoes an uniaxial stress parallel to the e_1 direction, i.e. all the stress tensor components are null expect for $\sigma_{11} = \sigma'_{11}$. It is easy to show by substituting Eq. 3.17 in Eq. 3.16, that the responce to such a stress is

$$\begin{aligned}
\varepsilon'_{11} &= \frac{1}{Y}\sigma'_{11} \\
\varepsilon'_{22} &= \varepsilon'_{22} = -\frac{\nu}{Y}\sigma'_{11} \\
\varepsilon'_{12} &= \varepsilon'_{23} = \varepsilon'_{13} = 0 \; .
\end{aligned}$$

As we can see, the Young's modulus describe the length change along the direction of the applied stress (ε'_{11}), while the Poisson's ratio describe the deformation (contraction or expansion) in the two directions perpendicular to the applied stress direction:

$$\varepsilon'_{22} = \varepsilon'_{33} = -\nu\varepsilon'_{11} \; .$$

3.1.3 Elastic energy density

The expression for the elastic energy of an continuum media is given by

$$E = \frac{1}{2}\int_\Omega dV \, C_{ijkl}\varepsilon_{ij}\varepsilon_{kl} = \frac{1}{2}\int_\Omega dV \, \sigma_{ij}\varepsilon_{ij} = \int_\Omega dV \, \rho_{el} \; , \tag{3.18}$$

being ρ_{el} the elastic energy density at each point in Ω. This expression can be written for an elastic isotropic medium as

$$\begin{aligned}
\rho_{el} &= \frac{1}{2}\,\sigma_{ij}\varepsilon_{ij} \\
&= \frac{1}{2}\,(2\mu\varepsilon_{ij} + \lambda\varepsilon_{kk}\delta_{ij})\varepsilon_{ij} \\
&= \mu\varepsilon_{ij}\varepsilon_{ij} + \frac{1}{2}\lambda\varepsilon_{kk}\varepsilon_{ii} \; , \qquad (3.19) \\
& \qquad (3.20)
\end{aligned}$$

where λ and μ are the Lamé coefficient introduced in the previous paragraph.

3.1.4 Mechanical equilibrium condition

Given the domain Ω, let us consider an arbitrary subdomain ω and suppose there is a traction T_i per unit area on the surface $\partial\omega$ and a body force f_i per unit volume. Then, force equilibrium in ω requires:

$$\int_{\partial\omega} d\gamma\, T_j + \int_{\omega} dV\, f_i = 0\,, \tag{3.21}$$

where the first term on the left represents the traction force on $\partial\omega$ and the second one the body force inside ω. Introducing the definition in Eq. 3.8, the previous equation turns out to be:

$$\int_{\partial\omega} d\gamma\, \sigma_{ij}\, n_j + \int_{\omega} dV\, f_i = 0\,. \tag{3.22}$$

Using Gauss' theorem for σ_{ij}, we then have the following equation:

$$\int_{\omega} dV\, (\sigma_{ij}\, n_j \,+\, f_i) = 0\,. \tag{3.23}$$

Since the previus condition must hold for any volume ω, the equilibrium condition at any point inside the body is:

$$(\sigma_{ij}\, n_j \,+\, f_i) = 0\,. \tag{3.24}$$

3.1.5 Boundary value problem

In order to find the equilibrium values of u_i, ε_{ij} and σ_{ij} in a given system, the mechanical equilibrium condition and the specified boundary conditions must be solved. Let us consider a solid medium of volume Ω and boundary $\partial\Omega = \Gamma_N \bigcup \Gamma_D$. Two types of boundary conditions are generally imposed. A traction force $\boldsymbol{g}$ may be applied on a boundary of the domain (Neumann boundary condition) or a certain values of the displacement $\boldsymbol{u}$ may be fixed (Dirichlet boundary conditions).
The general expression of the elastic problem as a boundary value problem can be written:

$$\begin{cases} -\sigma_{ij,j} &=& f_i & \text{on } \Omega \\ u_i &=& 0 & \text{on } \Gamma_D \\ \sigma_{ij} n_j &=& g_i & \text{on } \Gamma_N \end{cases} \tag{3.25}$$

The first equation simply describes the mechanical equilibrium equation for a solid body subjected to a volume force $\boldsymbol{f}$. The Dirichlet boundary conditions for the displacement are applied on Γ_D and the Neumann boundary conditions are applied on Γ_N. A free surface is described by applying the Neumann boundary condition and imposing that the traction force on Γ_N is null ($\boldsymbol{g} = 0$). The boundary Γ_D is fixed, and the displacements $\boldsymbol{u}$ are zero at this boundary position.

3.2 Elastic relaxation in epitaxial nanostructures

3.2.1 Biaxially strained films

Let us consider a flat homogeneous Ge film on top of a Si(001) substrate. The Ge film is ideally infinite along the $x = [001]$ and $y = [010]$ directions and the free surface is

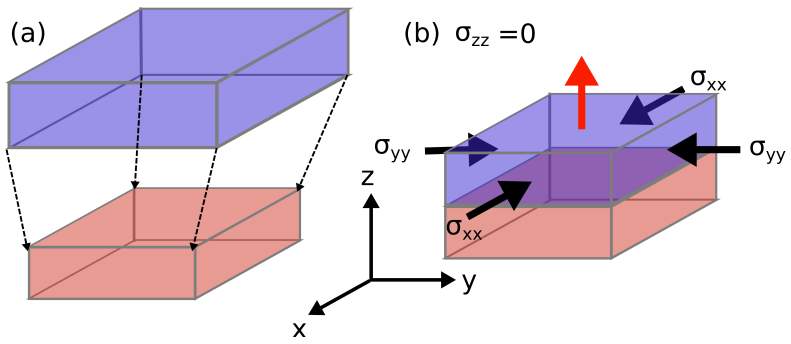

FIGURE 3.2: Illustration of the the biaxial stress in a planar film, resulting for example from the epitaxial integration of a Ge film on a Si substrate.

perpendicular to the $z = [001]$ direction. As a result, the film is biaxially strained along the x and y directions and it is free to expand in the positive z direction, as sketched in Fig. 3.2. Let us assume that the unit vectors $\{e_i\}_{i=1}^{3}$ of our reference system are parallel to the x, y and z directions, respectively. The in-plane strain components are fixed by the epitaxial relation between the Ge film and the Si substrate $\varepsilon_{xx} = \varepsilon_{yy} = \varepsilon_m$. Moreover, because of the planar simmetry the strain components ε_{ij} with $i \neq j$ are null. The only unknown strain component is ε_{zz}. In this simple case, the mechanical equilibrium condition is found by solving the boundary condition $\boldsymbol{\sigma} \cdot \hat{\boldsymbol{n}} = \boldsymbol{g}$ at the free surface with normal $\boldsymbol{n} = [001]$. Assuming isotropic elastic constants and no traction force $\boldsymbol{g}$ acting at the free surface, this condition reduces to:

$$0 = \sigma_{zz} = \lambda\varepsilon_{xx} + \lambda\varepsilon_{yy} + (\lambda + 2\mu)\varepsilon_{zz} \tag{3.26}$$

where

$$\varepsilon_m = \frac{a_{SiGe} - a_{Si}}{a_{SiGe}} \,. \tag{3.27}$$

By solving the boundary condition in Eq. 3.26, the strain component ε_{zz} is found

$$\varepsilon_{zz} = -2\frac{\lambda}{\lambda + 2\mu}\varepsilon_m = -2\frac{\nu}{1 - nu}\varepsilon_m \,.$$

The value of ε_{zz} has an opposite sign with respect to the in-plane strain component, being the deformation along z an attempt to recover the undeformed unit cell volume in the biaxially strained Ge film. Once the stress and strain tensor components are known, the elastic energy density in the film is given by

$$\begin{aligned} \rho_{el} &= \mu\varepsilon_{ij}\varepsilon_{ij} + \frac{1}{2}\lambda\varepsilon_{kk}\varepsilon_{ii} \\ &= {\varepsilon_m}^2 2\mu\left[1 + \frac{2\lambda}{\lambda + 2\mu}\right] \\ &= {\varepsilon_m}^2 \frac{Y}{1 - \nu} \,. \end{aligned} \tag{3.28}$$

For a pure Ge film, assuming ν=0.26 and Y=103 GPa, we have $\varepsilon_{xx} = \varepsilon_{yy} = \varepsilon_m$=0.04, $\varepsilon_{zz} = 0.03$ and $\rho_{el} = 1.38$ eV·nm^{-3}. For a $Si_{1-x}Ge_x$ film, the values of ε_{xx}, ε_{zz} and ρ_{el}

can be found assuming ε_m to vary with the Ge composition according to Eq. 2.3 and by linearly interpolating the Ge and Si elastic constants.

3.2.2 3D nanostructures

The elastic stresses and strains in an epitaxial flat film can be found analytically, due to the simple film geometry and boundary conditions. However, epitaxial nanostructures may have complex geometry and may expose many surfaces, so that numerical methods are needed to solve the condition of mechanical equilibrium combined to the boundary conditions. Since the elastic problem is described in terms of partial differential equations (PDEs), it can be solved in a continuum approach using finite element method (FEM), which is the most suitable technique for solving partial differential equations (PDEs) over complex domains. The results shown in this thesis are obtained using the commercial FEM code Comosol Multiphysics.

3.2.3 Epitaxial stress field by finite element method

The epitaxial strain or stress field of an arbitrary shaped nanostructure can be found by defining the initial strain state of the system by using the eigenstrain formalism, as defined in the Eshelby's Theory of inclusions.

Suppose we have a continum region Ω, which undergoes a permanent deformation. The strain value needed to restore the zero-stress condition in the region Ω (assumed unformly strained) is called *eigenstrain*. In general, we say that there is a condition of eigenstrain ε^*_{ij} in a certain region of the body if the stress vanishes as $\varepsilon_{ij} = \varepsilon^*_{ij}$. As a consequence, the eigenstrain tensor can be defined in the following way:

$$\sigma_{ij} = C_{ijkl}(\varepsilon_{ij} - \varepsilon^*_{ij}) \ . \tag{3.29}$$

The previous relation defines the eigenstrain ε^*_{ij} as the value of the strain field to have the stress field equal to zero. In fact,

$$\varepsilon_{ij} = \varepsilon^*_{ij} \Rightarrow \sigma_{ij} = 0 \ . \tag{3.30}$$

Furthermore, the eigenstress is defined as

$$\sigma^*_{ij} = C_{ijkl}\varepsilon^*_{ij} \ . \tag{3.31}$$

Generally, the deformed region is not able to reach the state of eigenstrain, i.e. the condition of zero stress. Instead, both the deformed region and the surrounding domains will deform in order to lower the total elastic energy.

Initial conditions

In the case of epitaxial nanostructure, one can assume that the eigenstrain condition is given by the lattice mismatch between the epilayer and the substrate, which is given by ε_m

(Eq. 3.27), as for the planar film case. The internal stress condition assigned to simulate the lattice mismatch between the epilayer and the substrate becomes:

$$\begin{cases} \sigma_{ij} = & C_{ijkl}(\varepsilon_{ij} - \varepsilon_m) & \text{epilayer} \\ \sigma_{ij} = & C_{ijkl}(\varepsilon_{ij} - 0) & \text{substrate} \end{cases}$$

Thus, the epilayer acts as a stressor in the system.

Boundary conditions

In the calculation of the stress field of epitaxial nanostructures (films, islands or nanowires) we assumed that there are no external body forces or acting on them, so that we set f_i=0. The epitaxial nanostructures are in contact with the substrate at the epilayer/substrate interface. The boundary value problem is given by

$$\begin{cases} -\sigma_{ij,j} &= 0 & \text{on} \Omega \\ u_i &= 0 & \text{on} \Gamma_D \\ \sigma_{ij} n_j &= 0 & \text{on} \Gamma_N \end{cases} \tag{3.32}$$

where, the Dirichlet boundary condition is applied at the bottom surface of the substrate, while at all the free surfaces the Neumann boundary condition is applied assuming that there are no traction force acting on them (g_i=0).

3.3 Dislocations in linear elasticity theory

Linear elasticity theory, is a very useful tool to describe the elastic field (in particular the long range field) produced by dislocations. In the following, we report the results concerning an isolated straight dislocation in a continuous isotropic medium, because the treatment of such dislocations is quite straightforward and analytical solutions have been provided for such defects. In general, dislocation displacements, stresses and strains depend on the finite size of the structure they are in. In case of a semi-infinite solid, as planar thin films, the simple image construction, as we will see below, can satisfy the boundary value problem, mimicking the effect of the free surface. Except for some simple geometries, in a multifaceted nanostructure the exact solution of the boundary value problem is quite difficult and the effect of the free surface on the dislocation must be solved numerically. In this Section, we describe the displacements, stresses and elastic energy of a straight infinite dislocation in a continuous isotropic medium. This is a helpful example to understand the deformation field induced by a dislocation with arbitrary orientation. The concept of force on a dislocation is introduced and the image construction in few simple geometries is presented. Analytical solutions exist also to describe the stress field of finite size straight dislocation segments [3, 109, 110] and they are qualitatively similar to the ones of an infinite straight dislocation (at least in the middle of the segments). It is worth to notice, that a curved dislocation line can be approximated by a sum of small straight segments.

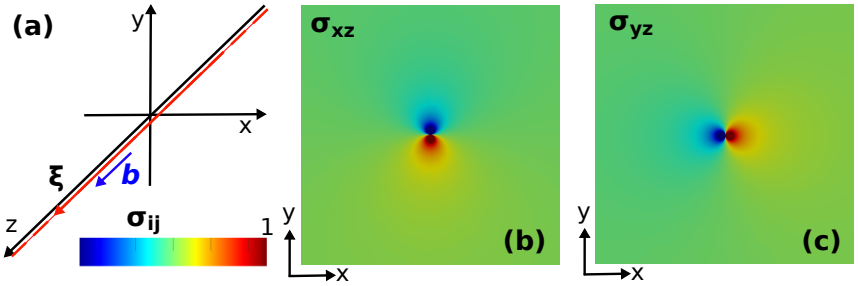

FIGURE 3.3: Stress tensor components for an infinite straight dislocation line $\boldsymbol{\xi}$ in a Si bulk material, parallel to the positive sense of the z direction with Burgers vector aligned to the z direction (screw dislocation), as sketched in (a). The stress tensor component (b-e) are plotted in a plane perpendicular to the dislocation line.

3.3.1 Dislocation displacements and stresses

As the dimensions of a solid body increase, the effect of the surfaces on a dislocation in the middle of it becomes smaller. In the limit of an infinite medium analytical solutions are provided for dislocation displacements, stresses and strains. Let us consider an infinite isotropic medium and let us choose a reference system where the z axis is parallel to the dislocation line $\boldsymbol{\xi}$ and the origin of the reference system is located exactly at the dislocation position. For the sake of clarity, we rewrite each components of the displacement field u_i as $u_x = u$, $u_y = v$ and $u_z = w$.

From the equilibrium equations (Eq. 3.24, combined with Eq. 3.3 and Eq. 3.8), considering static conditions, the exact expressions of the displacements around a dislocation can be obtained by imposing the following condition. If a close loop around the dislocation is taken, the displacement of the final point with respect to the initial one has to be equal to the Burgers vector length. From the displacement expressions the stress and strain terms can be obtained by simply exploiting the strain stress tensor definitions, expressed by Eq. 3.3 and Eq. 3.8.

Screw dislocation

In case of a pure screw dislocation, with $\boldsymbol{\xi}$ parallel to the z axis and such that its tangent vector is aligned to the positive orientation of z, the Burgers vector will be in the same direction ($\boldsymbol{b} = \mathrm{b}\ \hat{\boldsymbol{z}}$). The displacement field satisfying the equations of elasticity induced by such a screw dislocation is:

$$\begin{aligned} w &= -\frac{b}{2\pi} \arctan \frac{y}{x} \\ u &= v = 0 \end{aligned} \tag{3.33}$$

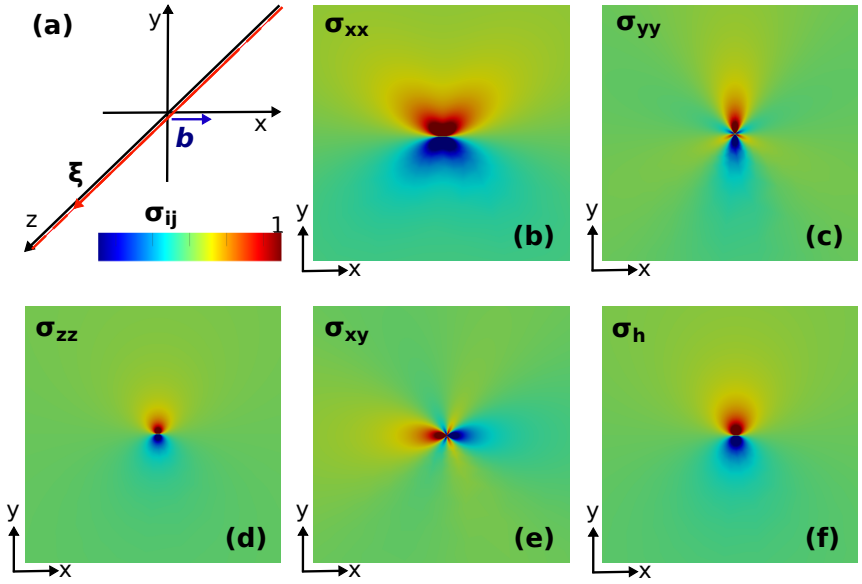

FIGURE 3.4: Stress tensor components for an infinite straight dislocation line $\boldsymbol{\xi}$ in a Si bulk material, parallel to the positive sense of the z direction with Burgers vector aligned to the x direction (edge dislocation), as sketched in (a). The stress tensor component (b-e) are plotted in a plane perpendicular to the dislocation line.

and the stresses associated with such displacements are:

$$\begin{aligned} \sigma_{xz} &= \frac{\mu b}{2\pi}\frac{y}{x^2+y^2} \\ \sigma_{yz} &= -\frac{\mu b}{2\pi}\frac{x}{x^2+y^2} \\ \sigma_{xx} &= \sigma_{yy} = \sigma_{zz} = \sigma_{xy} = 0 \,. \end{aligned} \tag{3.34}$$

In Fig. 3.3(b-c) the non zero stress tensor component induced by an infinite straight screw dislocation in a bulk material, as sketched in Fig. 3.4(a), are plotted in a plane perpendicular to the dislocation line. The color maps in Fig. 3.4 were obtained by substituting ν=0.27 and $b = 3.841$ $\AA$, which are the Poisson ratio and the Burgers vector expected in a Si bulk material in standard condition.

Edge dislocation

For an edge dislocation, the Burgers vector is parallel to one of the directions perpendicular to the dislocation line. Let us consider the Burgers vector in the x direction ($\boldsymbol{b} = \mathrm{b}\,\hat{\boldsymbol{x}}$), and $\boldsymbol{xi}$ oriented as the positive z axis, as shown in Fig. 3.4(a). In this case the displacement field in a bulk material induced by such an edge dislocation is:

$$\begin{aligned} u &= -\frac{b}{2\pi}\left[\arctan\frac{y}{x} + \frac{\lambda+\mu}{\lambda+2\mu}\frac{xy}{x^2+y^2}\right] \\ v &= -\frac{b}{2\pi}\left[\frac{\mu}{2(\lambda+2\mu)}\log\frac{x^2+y^2}{C} + \frac{\lambda+\mu}{\lambda+2\mu}\frac{y^2}{x^2+y^2}\right] \\ w &= 0 \,. \end{aligned} \tag{3.35}$$

The C coefficient is inserted to adjust the units of the argument of the logarithmic term. Since both the strain and the stress tensors depend on the derivatives of the displacement field, an arbitrary value of C can be assigned. The stresses associated with the same edge dislocation are given by:

$$\begin{aligned}
\sigma_{xx} &= \frac{\mu b}{2\pi(1-\nu)} \frac{y(3x^2+y^2)}{(x^2+y^2)^2} \\
\sigma_{yy} &= -\frac{\mu b}{2\pi(1-\nu)} \frac{y(x^2-y^2)}{(x^2+y^2)^2} \\
\sigma_{xy} &= -\frac{\mu b}{2\pi(1-\nu)} \frac{x(x^2-y^2)}{(x^2+y^2)^2} \\
\sigma_{zz} &= \nu(\sigma_{xx}+\sigma_{yy}) = \frac{\mu\nu b y}{\pi(1-\nu)(x^2+y^2)} \\
\sigma_{xz} &= \sigma_{yz} = 0 \, .
\end{aligned} \tag{3.36}$$

In Fig. 3.4(b-e) the non zero stress tensor component induced by an infinite straight edge dislocation in a bulk material, as sketched in Fig. 3.4(a), are plotted in a plane perpendicular to the dislocation line. The hydrostatic stress field, i.e. the trace of stress tensor $\sigma_h = 1/3 \, \mathrm{Tr}\, \boldsymbol{\sigma} = 1/3(\sigma_{xx}+\sigma_{yy}+\sigma_{zz})$, is plotted in Fig. 3.4(f); this is a key quantity to visualize the actual stress field, since it is invariant with respect to the reference system choice. In the color map the red color indicate an expansive region, while the blue color indicate a compressive one. The color maps in Fig. 3.4 were obtained by substituting ν=0.27 and $b = 3.841$ $\AA$.

Mixed dislocation

Let us now consider a general straight dislocation, characterized by $\boldsymbol{\xi}$ parallel to the positive z axis and $\boldsymbol{b}$ forming an arbitrary angle β with $\boldsymbol{\xi}$. The Burgers vector can thus be decomposed in a screw component $\boldsymbol{b_s}$ parallel to the dislocation line and in an edge component $\boldsymbol{b_e}$ perpendicular to it. By the superposition principle, holding in linear elasticity theory, the expressions of stresses, strains and displacements of the mixed dislocation can be written as the sum of the component's solution.
As an example of a mixed dislocation, we considered a 60°dislocation, typically observed in epitaxial Si-Ge systems, as sketched in Fig. 3.5(a). The dislocation line $\boldsymbol{\xi}$ is parallel to the [110] direction (here z) and lie in a plane perpendicular to the [001] direction (i.e. the interface normal). The Burgers vector is $\boldsymbol{b} = b[10\bar{1}]/\sqrt{2}$. The x and y directions are parallel to the $[\bar{1}10]$ and the [001] directions. In Fig. 3.5(b-h) the stress tensor components and the hydrostatic stress field σ_h induced by an infinite straight 60°dislocation in a bulk material, are plotted in a plane perpendicular to the dislocation line. In the color map the red color indicate an expansive region, while the blue color indicate a compressive one. The color maps in Fig. 3.5 were obtained by substituting ν=0.27 and $b = 3.841$ $\AA$.

It is interesting to notice that directly from the mathematical form of the dislocation displacements (or stresses) we can derive the limit of elasticity theory in describing dislocations. In fact, by looking at Eqs. 3.33-3.36, it is clear that both the displacements and the stress components induced by the dislocation diverge when the distance from the

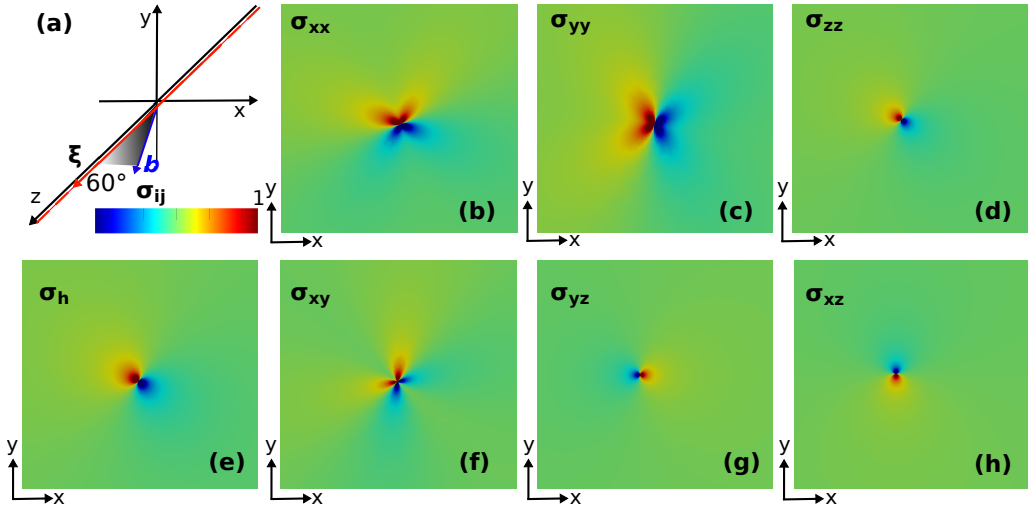

FIGURE 3.5: Stress tensor components for an infinite straight dislocation line $\boldsymbol{\xi}$ in a Si bulk material, parallel to the positive sense of the z direction and having Burgers vector oriented so as to form a 60°angle with the dislocation line, as sketched in (a). The stress tensor component and the hydrostatic stress field are plotted in a plane perpendicular to the dislocation line.

dislocation line ($d = \sqrt{x^2 + y^2}$) is close to zero. One of the assumptions in linear elasticity theory is that $|\boldsymbol{u}| \ll 1$. Thus, linear elasticity theory is inadequate to descibe the displacements in the proximity of the dislocation line. In that region the atomistic nature of solids can not be neglected and atomistic simulations are needed to capture the actual atoms position close to dislocation lines ($d \lesssim 5b$).

3.3.2 Dislocation elastic energy

A solid undergoing a deformation accumulates elastic energy. The elastic energy induced by the deformation field of a dislocation is also called dislocation *self energy*. In general, a dislocation induces in a crystalline material an extended deformation field. Its self-energy is given by the integration of the elastic energy density (see Eq. 3.18) in the entire body. This calculation is not always straightforward, due to the complexity of the dislocation or the solid body geometry. However, in few simple cases it can lead to an analytical expression of the dislocation self-energy.

Let us consider a straight dislocation line, as described above, in an isotropic and homogeneous elastic medium, in a region bounded by a cylindrical surface of radius r_c and an other coaxial cylinder with radius $R \gg r_c$, being the dislocation parallel to the axis of the cylinders and having all length L. It is found that the elastic energy per unit length is given by:

$$\frac{E_{self}}{L} = E(\beta) \log \frac{R}{r_c} = \frac{\mu b^2}{4\pi} \left(\cos^2 \beta + \frac{\sin^2 \beta}{1 - \nu} \right) \log \frac{R}{r_c} \tag{3.37}$$

where $E(\beta)$ is called *prelogarithmic energy factor* which depends on the angle between the dislocation line and the Burgers vector, b is the Burgers vector length and r_c is a parameter called core radius. Eq. 3.37 diverges for the two limits $r_c \to 0$ and $R \to \infty$. The divergence

for $r_c \to 0$ arises from the limit of linear elasticity theory to describe the deformation in the proximity of the dislocation line. In such a core region, characterized by highly distorted or dangling bonds, stresses are large and an accurate atomistic description is needed being at distance similar to the bonds length. As a result, equations derived by linear elasticity theory are restricted in a region outside a cylinder of radius r_c, called core radius, around the dislocation line. The total energy is found by adding an additional energy core term. When the core energy of a dislocation is known, for example from atomistic simulations, this term can be included in the elastic energy expression by choosing a smaller r_c values so as to make Eq. 3.37 to give the total energy. In particular, $r_c = b/\alpha$ is usually taken, and α is adjusted to match atomistic calculations for the core energy. In Si crystals, r_c is usually set by assuming $1 < \alpha < 4$. In this work we assumed α=2.7 as in Ref. [3, 26]. The divergence for $R \to \infty$ shows that the elastic energy of the dislocation depends on a characteristic size of the crystal that contains the dislocation. For a solid with arbitrary shape a good choice of the cut-off radius R is the shortest distance between the dislocation and the free surface. At larger distances, image stresses cancel the dislocation stresses. Similarly, the presence of other dislocations (with both signs) may cancel such stresses. In this case, the cut-off radius can be reasonably assumed to be equal to the average distance between dislocations.

3.3.3 Force on a dislocation

The force on a dislocation is defined as the force arising from the change in the free energy W associated with a dislocation displacement, which induces a variation in the dislocation line ℓ:

$$\frac{F}{L} = -\frac{\partial(W/L)}{\partial \ell} \ . \tag{3.38}$$

Let us consider the case of a straight dislocation line that moves at each point by $\delta \boldsymbol{r}$. If a uniform stress field $\boldsymbol{\sigma}$ exists at the dislocation position, the work done to move the dislocation line by $\delta \boldsymbol{r}$ under $\boldsymbol{\sigma}$ is

$$\begin{aligned} \frac{\delta W}{L} = \frac{\boldsymbol{F}}{L} \cdot \delta \boldsymbol{r} &= [\boldsymbol{\sigma} \cdot (\boldsymbol{\xi} \times \delta \boldsymbol{r})] \cdot \boldsymbol{b} \\ &= (\boldsymbol{b} \cdot \boldsymbol{\sigma}) \cdot (\boldsymbol{\xi} \times \delta \boldsymbol{r}) \\ &= [(\boldsymbol{b} \cdot \boldsymbol{\sigma}) \times \boldsymbol{\xi}] \cdot \delta \boldsymbol{r} \ . \end{aligned} \tag{3.39}$$

where $\boldsymbol{\sigma} \cdot (\boldsymbol{\xi} \times \delta \boldsymbol{r})$ is the force produced by the stress tensor $\boldsymbol{\sigma}$ on the surface $\boldsymbol{\xi} \times \delta \boldsymbol{r}$. Consequently, the force per unit length is

$$\frac{\boldsymbol{F}}{L} = (\boldsymbol{b} \cdot \boldsymbol{\sigma}) \times \boldsymbol{\xi} \ . \tag{3.40}$$

Eq. 3.40 represents the force acting on a dislocation line due to a given stress field $\boldsymbol{\sigma}$ existent at the dislocation position, that can be an external stress field applied to the solid or can be induced by an other dislocation or defect present in the solid. Such force is commonly called the *Peach-Kohler* force. In case of curved dislocations an additional force due the dislocation interaction with itself, the so called *line tension*, should be added.

3.3.4 Resolved shear stress

Dislocations move in crystalline materials in the favorable glide planes, as discussed in Section 1.1.2. Such a motion is driven by the action of a shear stress in the dislocation glide plane, while the component of the stress field normal to this plane does not influence the glide motion. Hence, to quantify the effective force for dislocation glide one must consider the shear stress resolved in the glide plane and in the slip direction, i.e. in the Burgers vector direction. Once the stress field $\boldsymbol{\sigma}$ acting on a dislocation is known, the force per unit dislocation length can be evaluated by the *resolved shear stress* (RSS):

$$RSS = (\boldsymbol{b} \cdot \boldsymbol{\sigma}) \times \hat{\boldsymbol{n}} \, . \tag{3.41}$$

where $\boldsymbol{b}$ and $\widehat{\boldsymbol{n}}$ arethe Burgers vector and the glide plane normal of the dislocation. This quantity shows the effective stress that drives the dislocation nucleation and glide motion. A large positive value of the resolved shear stress means high probability of dislocation nucleation or large forces promoting the dislocation motion in the glide plane of the selected dislocation [3]. Thus, the RSS allows one to determine which slip systems are expected to be activated under an external stress field or the sites where dislocations are expected to preferentially nucleate in an system characterized by an heterogeneous stress field. Together with the temperature, the resolve shear stress determines the dislocation motion.

3.4 Dislocation modelling in nanostructures

Different strategies have been developed to deal with dislocations in thin films or in other nanostructures. We have seen that dislocations can be described either with a discrete approach, by considering the atom displacements from the perfect crystal positions, either with a continuos method, by defining a deformation field at each point of the solid containing such defects. Atomistic simulations can be carried out in order to obtain the atom configurations around dislocation lines, core geometries and energies (e.g. Ref. [111]). The main disadvantage of this approach is the long computational time required for atomistic simulations. In fact, only prototypical systems, with reduced sizes with respect to the typical length scale observed in experiments, can be simulated and even considering simplified systems the simulation times are considerably long. A continuum approach, instead, provides an accurate description of stress and strains, except for the core region surrounding the dislocation line. The most challenging issue to address plastic relaxation in nanostructures, is how to handle the interactions between dislocations and surfaces. In a restricted number of configurations the dislocation-surface interaction can be solved analytically by using image dislocations. However, in order to investigate structures with arbitrary shape and dislocation geometry, the numerical solution of the elasticity equations by FEM is the most adequate tool. This approach allows for a precise calculation of the dislocation stress field (except for the core) and the exact solution of the boundary value problem in complex systems. Additionally, this technique requires short simulation times. This method has been successfully tested by Gatti et al. in Ref. [82], where this approach is discussed in details, to investigate dislocation formation in epitaxial SiGe islands.

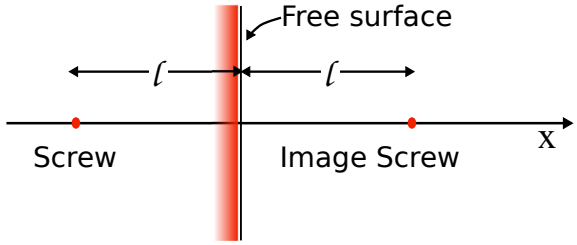

FIGURE 3.6: A screw dislocation parallel to the free surface and its image dislocation.

3.4.1 Analytical approach: image dislocations

For few simple dislocation geometries it is possible to solve the boundary value problem by using the so called *image construction*. Let us consider the case of a straight screw dislocation in a semi-infinite continuous medium, parallel to the free surface and aligned to the z axis. If the distance between the dislocation line and the free surface is l, the boundary condition $\sigma_{ij}n_j = 0$ is satisfied by superposing to the bulk stress field of the real screw dislocation the stress field of an imaginary screw dislocation, of the same strength but opposite in sign, which is at the mirror position outside the solid, as sketched in Fig. 3.6. In this case, an analytical expression for the dislocation stress field at a distance l from the free surface (which is given by $\boldsymbol{\sigma}_{screw} + \boldsymbol{\sigma}_{image}$) and for the force exerted by the surface to the dislocation is provided. The latter is given by substituting in the expression of the Peach-Kohler force (Eq. 3.40) the stress field produced by the image dislocation at the real dislocation position. In general, the image construction does not provide an exact solution of the boundary value problem. In fact, if we only consider an edge dislocation parallel to the free surface, instead of a screw one, the condition $\sigma_{ij}n_j = 0$ is not met anymore. An analytical solution for the stress field of an edge dislocation in a semi-infinite solid and parallel to the free surface was provided by Head in Ref. [112]. By combining the image construction for a screw dislocation and the analytical expressions proposed by Head, it is possible to exactly calculate stresses, strains, force and elastic energy of a general straight dislocation parallel to a flat free surface in a 2D layer. This can be very useful, to study the energy and the interactions of straight misfit dislocations in planar films. Still, if we are interested in the stress field of a dislocation with arbitrary shape in multifaceted structures, no analytical solution is provided. To this aim, we decided to use a FEM code to numerically solve the boundary value problem of a dislocation in a multifaceted nanostructure.

3.4.2 Numerical approach: finite element method

The problem of finding the stress field of a dislocation in an arbitrary shaped nanostructure has been addressed in this work by following the methodology reported in Ref. [82], where the onset of plastic relaxation in epitaxial SiGe islands has been determined by FEM calculations and successfully compared with experimental results. This approach is based on the superposition method, discussed in more details for example in Ref. [113, 122]. Let us start with of the calculation of the stress field due to a dislocation segment in a

solid body Ω, with boundary $\partial\Omega$. Equilibrium equations can be written in a boundary value problem, as for the case of a coherent nanostructure, and the solution to elastic problem can be solved numerically by FEM by applying the proper initial conditions. The superposition principle allows one to write the total stress field σ_{ij}^{tot} as the sum of different contribution to it. In particular, starting form the bulk solution or the dislocation stress field, the total the stress field in the finite size body Ω can be written as

$$\sigma_{ij}^{tot} = \sigma_{ij}^{surf} + \sigma_{ij}^{int} + \sigma_{ij}^{disl} \tag{3.42}$$

where σ_{ij}^{disl} is the dislocation stress field in bulk condition, σ_{ij}^{surf} is the correction due to the interaction between the dislocation and free surfaces (i.e. the correction needed to satisfy the boundary conditions at the free surfaces), while σ_{ij}^{int} is the correction due to the interaction between the dislocation and the interface (i.e. the correction needed to satisfy the boundary conditions at the internal boundaries among different materials). Analytical expression for the bulk solution of the dislocation stress field are available and can be used as initial condition to solve the boundary value problem. In particular, we used the non-singular expressions derived by Cai et al. [110], that reproduce the stress tensor components as derived in the classical dislocation theory [3], removing the singularity in correspondence of the dislocation line position. Once the initial condition is defined, the contribution to the total stress field induced by the free surfaces and by the interfaces is obtained by FEM, that allows one to numerically solve the boundary value problem.

In any epitaxial system, both the elastic field due to lattice misfit with the substrate and to the dislocations are present. The superposition principle allows one to simply sum the two initial stress fields and solve one unique boundary value problem. The initial strain condition is then given by imposing simultaneously the eigenstrain condition for the epitaxial field and the bulk dislocation stress field:

$$\begin{cases} \sigma_{ij} = & C_{ijkl}(\varepsilon_{ij} - \varepsilon_m) + \sigma_{ij}^{disl} & \text{epilayer} \\ \sigma_{ij} = & \sigma_{ij}^{disl} & \text{substrate} \end{cases}$$

The same boundary conditions described in Section 3.2.3 are then applied to solve the elastic problem, obtained accurate values of the stresses, strains, displacements and consequently the elastic energy in the examined nanostructures.

3.5 Dislocation dynamics simulations

The FEM method presented above, is a very useful tool to study static configurations of dislocations in realistic nanostructures and to compare the energetics and the strain state in few relevant geometries. However, it is not adequate to predict the microstructure formed by a large density of dislocations in epitaxial layers and to analyze the dynamic process of plastic relaxation, that eventually lead to dislocation pattern formation in strained nanostructures. In order to achieve this, it is fundamental to accurately describe the 3D shape of dislocation lines, their motion and their interactions in realistic-shaped nanostructures. Dislocation formation and motion is a complex phenomenon that involve the

breaking and distortion of atomic bonds close to the dislocation line, but also the deformation of an extended crystal region where the atoms are slightly displaced by their equilibrium positions. In the previous sections, we have seen that the description of such defects in the linear elasticity framework allows one to describe both the energetics and deformation field induced by dislocations into the crystal lattice. In order to provide a good description of dislocation motion, it is necessary to take into account also atomic scale features. 3D dislocation dynamics (DD) simulations can capture the fundamental aspects of dislocation evolution in time and space, by using a continuum framework to describe the dislocation stress field and by including atomistic features that govern dislocation motion and interactions as input parameters of the simulations, as taken from experiments or atomistic simulations. This technique is a unique tool that allows one to establish a connection between atomistic properties of dislocations and plastic behavior at the mesoscale and to directly compare the simulation results with experiments. This simulation method has been demonstrated to give accurate results in many problems of crystal plasticity including plastic relaxation in micro and nanometers size objects [115–117]. In the past 20 years, varius research groups have been developed different 3D-DD codes[118–124]. All of them are based on the following steps. First, the dislocation lines in a given configuration are discretized in smaller segments. The forces on the segments, mainly defined by the applied stress field and by the dislocation segments interactions, are calculated. The velocity of each portion is determined by applying a mobility law and the segment positions are updated according to a time step. This procedure is repeated to obtain the trajectory of dislocation lines and the resulting plastic behavior. Different DD codes may differ in the approximation adopted, for example in the discretization procedure, the core treatment the dislocation interactions, etc ..., and they all present advantages and disadvantages. In this work, we employed the *microMegas* code[1], developed at the Laboratoire d'etude des Microstructures (LEM) in Châtillon (France). This code was originally developed by Kubin and Devincre [118, 119], who presented the very first 3D-DD code, and further improved to include original features in the past years. A review article about this code can be found in Ref. [115], while a more general discussion on the DD technique compared with other simulation methodologies can be found in Ref. [5]. The dislocation dynamics simulations presented in this work were obtained in collaborations with Dr. B. Devincre and Dr. R. Gatti, presently working at the LEM, by using the microMegas code and by implementing a new procedure to handle dislocation nucleation in time.

In this section we present the methodology used in DD simulations to describe the motion and interactions of dislocations under an applied stress field. In particular, we summarize the key features of the microMegas code, highlighting its peculiar features with respect to other DD codes, when it is the case, and we describe the relevant elements to study plastic relaxation in thin films and nanostructures.

[1]see mM home page at: http:zig.onera.frmm_home_page

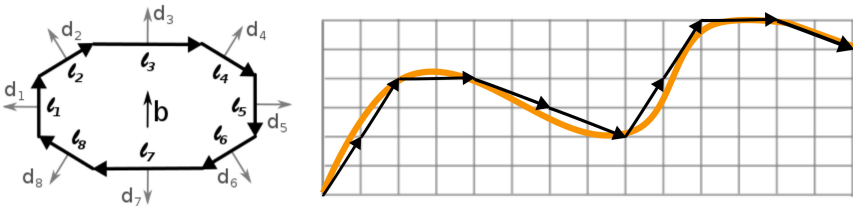

FIGURE 3.7: (a) Schematic representation of the elementary vectors used for each slip system to discretize dislocation lines in microMegas. The vectors ℓ_{1-8} (in black), are used for the definition of the segments directions and the vectors d_{1-8} (in grey) for the corresponding displacement directions. (b) Discretization of a continuos dislocation line on the discrete lattice.

3.5.1 The dislocation dynamics code microMegas

The microMegas code has been originally developed to study plastic behavior of crystalline bulk materials, but DD simulations in epitaxial thin films [117, 121] and nanoislands [125] demonstrated that this simulation tool is suitable to address plasticity also in objects with typical lengths in the order of tens or hundreds nanometers. Like usual DD simulations, 3D curved dislocation lines are discretized into a finite number of straight segments and the dislocation configuration is updated by moving each of them at discrete time steps. The main peculiarity of the microMegas code is that also the space is discretized. This means that the origin and the end of dislocation segments are positioned on a discrete simulation lattice. The latter should in principle be homothetical with respect to the real lattice of the investigated material (FCC,BCC,HCP,...). By scaling the simulation lattice it is possible to describe systems from the nanometer to the micrometer range. DD codes where the space positions are discretized are also referred as discrete dislocation dynamics (DDD) codes. Like in most DD simulations, the microMegas code treats perfect dislocations. Also, the motion and interactions of dislocations is restricted inside the glide planes. Thus, only the glide motion is allowed in our DD simulations. We remind that dislocation climb typically occurs at a different time scale with respect to glide, which is orders of magnitude faster, and, contrary to glide motion, it requires point defects or atoms diffusion. For these reasons, the two kind of motion are generally treated separately in literature. Also, at the typical growth conditions of epitaxial films and nanostructures glide is expected to be the dominant mechanism for dislocation motion, so that we can reasonably neglect the climb mechanism.

The materials we are dealing with in this work, are Si, Ge or Si-Ge alloys. Thus, in the following we will used as a reference simulation lattice the FCC one, since these materials can be described as a FCC lattice characterized by a basis of two atoms at each lattice point. Also, the slip systems considered for the glide motion of dislocations are the $\langle 110 \rangle \{111\}$, which are the favorite ones in FCC crystals and the most commonly observed in Silicon and Germanium.

Dislocation line discretization

As stated above, curved dislocation lines are described as the sum of elementary straight segments in a DD simulation. In microMegas, the positions of the segments are defined by the coordinates of the origin of the segment and by its vectorial length. Since each segment is restricted to start and finish at a simulation lattice position, the dislocation segments must be lattice vectors. In particular, only a finite set of lattice vectors is used to described the whole dislocation microstructures. In our DD simulations, curved dislocations lines, lying in the {111} planes of an FCC structure, were described by using a set 8 elementary directions (two screw,two edge and four 60°character) for each slip system, as shown in Fig. 3.7(a). This number is sufficient to accurately describe the dislocation lines with a reduce number of segments and to treat of the most important dislocation reactions in the FCC crystal symmetry. In the microMegas code, when the elementary cell matches the size of the real lattice a,the length of the elementary screw dislocation is exactly the modulus of the Burgers vector. Since we are considering only the $\langle 110 \rangle \{111\}$ slip systems, there are four possible {111} glide planes and three Burgers vectors for each of them for a total number of 12 slip systems and 96 elementary directions (8 segments for each slip system). The dislocation lines are typically described by a sequence of segments that are multiple of the elementary directions. The length of the dislocation segments are close to an average value which is a parameter of the simulation, called the *discretization length* ℓ_{disl}, and can be suitably tuned to accurately describe dislocations in a given geometry with a specific length scale. In Fig. 3.7(b), it is illustrated how a curved dislocation can be approximated by the sum of the elementary directions. It is easy to show, that the smaller are the segments, the more the discrete dislocation description resembles a continuum dislocation line (orange line). However, the smaller is the discretization length the larger is the number of segments needed to describe the whole dislocation length and, consequently, the number of computation operations required to model the dislocation evolution. Since the dislocation shape (length and curvature) evolve with time, the discretization procedure is applied at each time step and segments can be added or removed at the beginning of a time step to better describe the updated dislocation configuration.

Force calculation

The formation and motion of dislocations in a crystal structure is driven by the reduction of the total elastic energy. As derived in the classical dislocation theory [3], the force exerted on a dislocation can be expressed as the elastic energy variation due to an infinitesimal modification of the dislocation line configuration. This force per unit length is given by the Peach-Koehler (PK) force, as reported in Eq. 3.40, and by a local line tension correction τ_L. In a DD simulation the calculation of the forces is the most important step. Once the forces acting on the dislocation segments are determined their displacements, and consequently the updated dislocation microstructure, is found accordingly to a mobility law, as we will see below. In the microMegas code, the forces acting on each segment are computed at their middle point, except for segments close to a discontinuity (e.g. a discontinuity in the curvature of the dislocation line). In these peculiar cases the forces are calculated at a distance λ_c (typically set $\lambda_c \approx 10b$)from the singularity defined in the

simulation parameters.

The Peach-Koehler force acting on each dislocation segment is given by two contributions. The first derives from the applied stress field ($\boldsymbol{\sigma_{app}}$) driving dislocation motion, which in our case is the epitaxial stress field of the coherent structure. Whereas the second one arises from the whole dislocation microstructure ($\boldsymbol{\sigma_{int}}$). The stress field $\boldsymbol{\sigma_{int}}$ is found by summing up all the individual contributions to stress field produced by all the segment in the simulated volume except for the considered segment and the neighboring ones. Several analytical expressions for calculating these interaction stresses have been derived in the isotropic linear elasticity framework. In the microMegas code, the stress field produced by a dislocation segment is calculated with the formulation given in Ref. [109]. These expressions are mechanically correct only for closed dislocation loops in bulk materials. Hence, the correct expression of the stress field of dislocation lines ending at free surfaces in finite simulation volumes should be considered [113, 126] or corrected by using suitable approximations [121]. The PK force expressed in Eq. 3.40 can be rewritten by highlighting the two stress contributions:

$$\boldsymbol{F}_{PK} = \boldsymbol{b} \cdot (\boldsymbol{\sigma}_{app} + \boldsymbol{\sigma}_{int}) \times \boldsymbol{\xi} \tag{3.43}$$

where $\boldsymbol{b}$ and $\boldsymbol{\xi}$ are respectively the Burgers vector and the dislocation line direction of straight segment i.

The local line tension contribution $\boldsymbol{\tau}_L$ takes into account the local line curvature close to the segment considered and, in some cases, an image correction arising from the presence of surfaces and interfaces. Since the stress field that a curved dislocation exerts on itself diverges at short distances, as derived by elastic dislocation theory [3], a regularization procedure is typically adopted to avoid this artificial stress singularity in the force calculation. Therefore an alternative expression, called the local line tension, is used to calculate the force induced by the segment itself and by its neighbors, replacing the calculation of the Peach-Kohler force on a segment induced by itself and by the neighboring ones. In literature, different expressions have been proposed to describe this self-interaction and most of them are proportional to $1/R[\ln(R/r_c) + O(1)]$ [127–130]. R is the local radius of curvature, r_c is the core radius tipically set $r_c \approx |b|$ and $O(1)$ takes into account additional first-order geometrical terms. As we have seen in Section 3.3, the choice of the the core radius, used to take into account the core energy, leads to significant errors. It is worth to notice, that all the expressions derived in the continuum framework to substitute the atomistic core structure with an approximated treatment of the self-interaction lead to errors up to 20%, when R/r_c approaches unity, i.e. in case of simulations at the nanometer scale. In the microMegas code four different expressions for the line tension have been already implemented and can be used. All the results presented in this work were obtained by using the expression derived by Foreman [128].

In order to compute the effective force on a dislocation segment, the Peach-Kohler force must be projected on the glide plane of the segment ($\boldsymbol{\tau}_{PK}$). The total effective force acting on the straight segment i in the glide plane then becomes:

$$\boldsymbol{\tau}_{eff,i} = \boldsymbol{\tau}_{PK,i} + \boldsymbol{\tau}_{L,i} \ . \tag{3.44}$$

Mobility law and time integration

Once the forces on the segments are known, their velocities are assigned according to a *mobility law*. The latter takes into account the resistance that the lattice opposes to the dislocation motion. This may give rise to thermally activated motion, simple dissipative motion or takes into account some peculiar mechanism at the atomic scale. Also a character dependent mobility law can be assigned. In this work, we assumed that dislocations move everywhere with a velocity which is directly proportional to the local force:

$$\boldsymbol{v}_i = \frac{\tau_{eff,i} b_i}{B} \tag{3.45}$$

where B is a viscous drag coefficient. Although in the present work we used a simple velocity equation, in general, and especially in materials with an high lattice resistance like Si, the mobility is strongly dependent on the temperature [35, 131]. Also, at low temperature, the dislocation glide motion in Si is typically thermally activated since it depends on complex kink pairs nucleation and propagation mechanisms, which is characterized by high activation barrier [132, 133]. The constant proportionality factor between the forces and the velocities adopted here, can be justified by the fact that we are interested in Si-Ge nanostructures grown at high temperatures and subjected to very high stresses, larger than $\sim$ 1GPa, arising from the lattice mismatch between the substrate and the epilayer. We notice that in the microMegas code the entire segment move as a whole in the same direction.

Since inertial effects can be usually neglected and dislocations glide with a steady state velocity (dislocation mass is small and the line energy very large), the segment positions $\boldsymbol{x}_i$ are updated by using the explicit Euler forward method (which is the standard integration method in DD simulations):

$$\boldsymbol{x}_i(t) = \boldsymbol{x}_i(\Delta t) + \boldsymbol{v}_i \Delta t \tag{3.46}$$

where $\boldsymbol{x}_i(t)$ is the position at the time t and Δt is the time step chosen to run the simulation. In the simulations presented in this work the time step was set to be $\sim 1 \times 10^{-12}$ s. We finally notice, that even if the segment positions are defined on a discrete lattice, the displacements are performed in a continuum space. In particular, the discretized positions ($\boldsymbol{x}_i(t)$) are defined on the lattice sites nearest to the positions in the continuum calculated using the real coordinates ($\boldsymbol{r}_i(t)$) and are used to efficiently detect the other segments or obstacles encountered by the segments, during their displacements.

Dislocation reactions and interactions

In the microMegas code elementary dislocation mechanisms that involve core process, such as cross slip, contact reactions (junctions formation, annihilations) or interactions between dislocations, are taken into account during the dynamics, thanks to local rules implemented in the code. When two dislocations come close to each other, their elastic field interact affecting their dynamics. Depending on the two dislocation types and on their reciprocal orientation, their interaction can be attractive, leading to dislocation annihilation at the contact position, junction formation or the formation of a cross state,

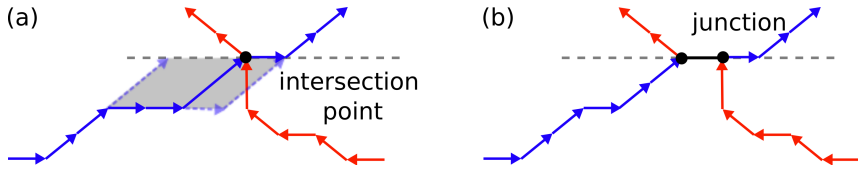

FIGURE 3.8: Illustration of ajunction formation in the microMegas code. (a) In the area swapped by a segment during its displacement an other dislocation segment is present. The intersection point between the two is found and the first segment is stopped exactly at the intersection point. (b) If the junction formation is favorable, it results by the lateral motion of the dislocation segments belonging to the different dislocation lines (indicated in blue and red), that promote the elongation of the two dislocation lines along the junction direction (dashed grey line), i.e. the intersection between the glide planes of the two dislocations.

where no reaction is taking place but their interaction affect the dislocation configuration. In microMegas, the discretization of the space allow to deal with dislocation reaction, even of non-coplanar segments, in a quite simple way. In fact, once the segment displacements are predicted, the code test if during an elementary displacement the segment encounters an other dislocation segment in the area swapped. In this case, the segment is stopped in correspondence to the second dislocation position. A junction is formed if the force drives the elongation of the two dislocation along the junction direction, as illustrated in Fig. 3.8. Otherwise, the two dislocations move apart, without reacting with each other. In the microMegas code junction segments are considered immobile, so that junction formation (or removal) is controlled by the dynamics of the segments adjacent to a junction. Annihilation reactions consists in the overlapping of two segments with opposite Burgers vector along the intersection of the glide planes of the two moving dislocations (dashed grey line in Fig. 3.8). In this case, the segments along this line are removed and the two dislocations involved in the reaction are connected to each other.

Cross-slip

Cross-slip is a process that allows a dislocation to change glide plane from its original glide plane to an other allowed glide plane, called cross slip plane. This process is possible when a dislocation segment sufficiently long is aligned to the screw direction, so that in this configuration the segment belongs to two possible glide planes (i.e. two possible slip systems characterized by the same Burgers vector). If the dislocation experiences a larger resolved shear stress on the cross slip plane with respect to the original one, the dislocation can *cross slip* and propagate in the new glide plane.This process usually involve a core transformation and it is thermally activated in most experimental conditions. However, in case of high stress, cross-slip is mostly mechanically activated. The rules for cross-slip in FCC crystals were reported for example in Ref. [115]; since the cross-slip process is not crucial for the interpretation of the simulation results of this work we will not go into the details of this mechanism.

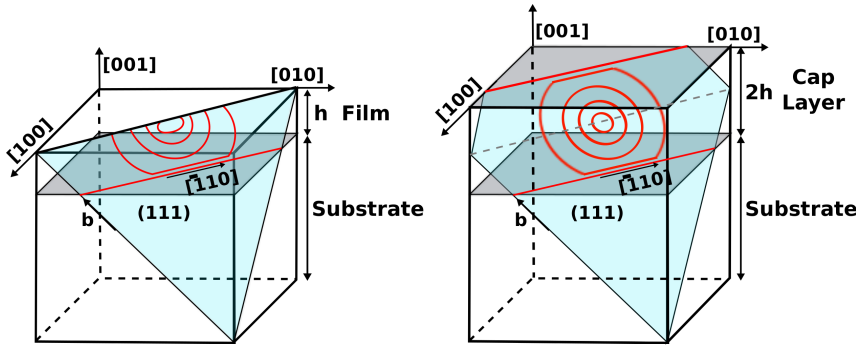

FIGURE 3.9: Illustration of the cap layer approximation to model the effect of the free surface. A planar film with a free surface of thickness h (h) is replaced by a layer bounded by two specular interfaces with thickness $2h$ (b).

3.5.2 Dislocation dynamics in nanostructures

The microMegas code is certainly a robust technique to model plasticity in bulk conditions. This is achieved by applying periodic boundary conditions (PBCs) at the boundaries of the simulation box. By reducing the size of the simulated systems the elastic interaction of dislocations with surfaces becomes important. As we seen in Section 3.4.1, in a first approximation the influence of the surface on the dislocation stress field can be described by introducing image dislocations. The effect of the surface is inversely proportional to the distance between the dislocation and the free surface, so that this contribution is expected to be important in systems with linear dimensions smaller than 1 μm. Since we are dealing with nanostructures, as thin films and nanowires, it is important to include such contribution in the DD simulation. In the case of planar thin films, the effect of the free surface can be considered by using the so called cap-layer approximation. The latter consists in substituting a thin film with a planar surface at a distance h from the interface with a layer of thickness $2h$ bounded by two equivalent interface, as shown in Fig. 3.9. This approximation is similar to the image construction and provides a a correction to the elastic field of a dislocation in a bulk mimicking the effect of the free surface. Such an approximation has been proven to be useful to model the plastic relaxation in planar thin films, giving accurate results in agreement with analytical model available in few simple cases and to experiments [116]. The disadvantage of this approach is that it cannot be easily extend to geometries different from the planar 2D film. However, in many cases it is possible to describe effect of the surfaces by using a simpler approximation. As discussed in in details by Schwarz [120, 121, 125], it can be sufficient to correct the force acting on the segments touching the free surfaces to describe the motion of dislocation in thin films or nanostructures. When the applied stress field is high compared to the stress field induce by the dislocation microstructure, the modification of the stress field due to image effect can be neglected as it only modifies the velocity of the threading segments. However, a second effect arises from the presence of the free surface. In particular, the surface maintain the contact angle of a dislocation segment emerging at the free surface constant with respect to surface normal. A physical approximation, provided by classical dislocation

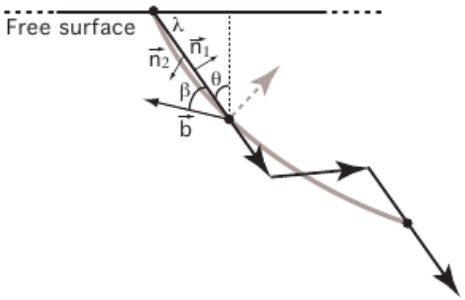

FIGURE 3.10: Projection of a segment touching a free surface on its glide plane. Two competing forces act on this segment. One arises from image forces. It depends on the angle θ and tends to rotate the segment towards the normal to the surface. The second one depends on the character via the angle β and tends to rotate it towards the screw direction. [115]

theory [3] and first employed by Schwarz in DD simulations[120, 125], takes into account the two competing forces arising from the interaction with surfaces and determining the configuration of the dislocation segments touching a free surface, as illustrated in Fig. 3.10. The first term tends to rotate the dislocation perpendicularly to the free surface and takes into account that the shorter the dislocation length, the lower is the elastic energy induce by the dislocation into the system. On the contrary, the second term tends to rotate the dislocation segment parallel to the screw direction, which is the lowest energy orientation, as can be easily deduced by Eq. 3.37. These two contributions can be taken into account by substituting to classical expression of the local line tension τ_L the following equation for the segments touching a free surface:

$$\tau^{fs} = \frac{1}{\lambda}\frac{\mu b^2}{4\pi(1-\nu)}\left[\hat{\boldsymbol{n}}_1|(1-\cos^2\beta)\tan\theta| + \hat{\boldsymbol{n}}_2|(2\nu\cos\beta\sin\beta)|\right] \tag{3.47}$$

Here, $\hat{\boldsymbol{n}}_1$ and $\hat{\boldsymbol{n}}_2$ are the unit vectors parallel to the surface normal and to the Burgers vector, forming, respectively, an angle of θ and β with the dislocation line orientation of the segment touching the free surface. In Eq. 3.47, λ is the distance from the point at which the dislocation segment intersects the free surface to the point of the segment where the modified line tension contribution is applied. is appliedλ is a parameter of the simulation and was tuned in order to reproduce the critical thickness for plastic relaxation in epitaxial flat films [117], as calculated in Ref. [26]. It is worth to notice that τ^{fs} is typically small compared to the total force acting on most segments, especially when the applied stress field is large. However, it corrects the orientation of the threading segments, influencing the interactions and reactions with other segments. Thus, it is a key contribution to define the final dislocation microstructure. For the systems investigated in this work, the modified line tension approximation is the most suitable one, as we have to deal with complex geometries bounded by many free surfaces. Improvements have been made in the last ten years to accurately take into account different boundary conditions. This has been possible by coupling DD simulations with FEM codes to numerically solve the mechanical equilibrium condition. We notice, that coupling with a FEM code would

increase significantly the computation time needed to run DD simulations, limiting the dimension of the simulated volume.

3.5.3 Dislocation nucleation procedure

Dislocation dynamics simulations typically start from a fixed number of dislocation sources and predict the evolution of such an initial configuration driven by an applied stress field and taking into account dislocation interaction with other dislocations, surfaces and interfaces. In epitaxial growth experiments, dislocations nucleate in epilayer at different times, so that the number of mobile threading segments increases during the early stages of the growth process. In order to reproduce such a behavior, the microMegas code has been modified to include a simple stochastic procedure to nucleate small dislocation loops, periodically in time, during DD simulations. In particular a constitutive local rule has been added, that simply tests the possibility to expand a new dislocation loop with a small initial radius R at a random position of the simulated volume under the applied stress field. More precisely, at a predefined time periodicity Δt, we randomly select the coordinates of a nucleation site inside the simulated volume. Secondly, the resolved forces on the segments discretizing the elementary loop are calculated in the dislocation glide plane. If the resulting forces act, on average, to expand the loop, we create effectively the loop and leave it free to evolve together with the other existing dislocations. Otherwise, the procedure is repeated until a favorable site for the loop expansion is found. The initial circular loop shape is defined inside the dislocation glide plane and it is discretized in 8 segments forming an octagon. These segments were chosen to be for simplicity parallel to the 8 eight elementary vectors used in the code to discretize the whole dislocation microstructure. This procedure is particularly useful to investigate plastic relaxation in structures characterized by a non-uniform stress field and to predicted the preferential sites for dislocation nucleation and propagation.

By testing in the simulation volume only dislocation loops belonging to a selected slip system, it is possible to investigate separately the formation and evolution of dislocation belonging to different slip systems. This approach has been employed to study the formation mechanism of dislocation in core-shell nanowires, as discussed in Chapter 6. The nucleation procedure can also be applied to assess simultaneously the preferential sites of dislocations of different slip systems in an heterogeneous stress field, as has been done to analyzed the plastic relaxation process in thin film grown on pit-patterned substrates and discussed in Chapter 4. This procedure may be further modified to include new features of the nucleation process as derived by experiments or atomistic simulations.

4

Dislocation engineering by substrate nanopatterning

Single crystalline, semiconductor SiGe films have been extensively studied in the past decades because of their crucial importance in the micro- and opto-electronics industry. In the electronic field, the development of SiGe heterojunctions bipolar transistors and strained Si/SiGe CMOS technology have promoted a large research aimed to control the SiGe layer growth and to tailor the desired material properties. [134] However, the possibility to use thick SiGe or Si layers is hindered by the nucleation of dislocations, which have been demostrated to be detrimental to device performances in diamond and zincblende semiconductors. This is true also for metastable layers, which eventually evolve dislocations because of subsequent thermal treatments. Pseudomorphically strained, semiconductor heterostructures, are also important for the fabrication of optoelectronic devices. Even though in low mismatched material systems, such as AlGaAs/GaAs or InGaAsP/InP the interfacial strain can be elastically accommodated. In heterostructures characterized by a larger mismatch, such as Si/Ge or InAs/GaAs, defects, are typically observed after the deposition of only few nanometers of the epilayer material. Among them, the generation of interfacial misfit dislocations is typically observed with the increasing layer thickness. These defects are often charged and act as non-radiative recombination centers and electrical shorts and can rapidly degrade the operation of light emitting diodes or lasers.

It is clear, that in the epitaxial integration of Ge or different semiconductor materials on Si(001), controlling and possibly confining dislocations in pre-defined regions, would allow for device positioning in selected areas far from the detrimental dislocations. Moreover, defined access to the electrical conductivity of dislocations [135] and electroluminescence measurement [136, 137] are other fields that would benefit from the possibility of governing the position of dislocations on a nanometric scale. However, this goal has always been hindered, because heterogeneous nucleation of dislocation loops at unpredictable defects on the surface of the growing film prevents any meaningful control.

In this Chapter, we first summarized the main features of the plastic relaxation process

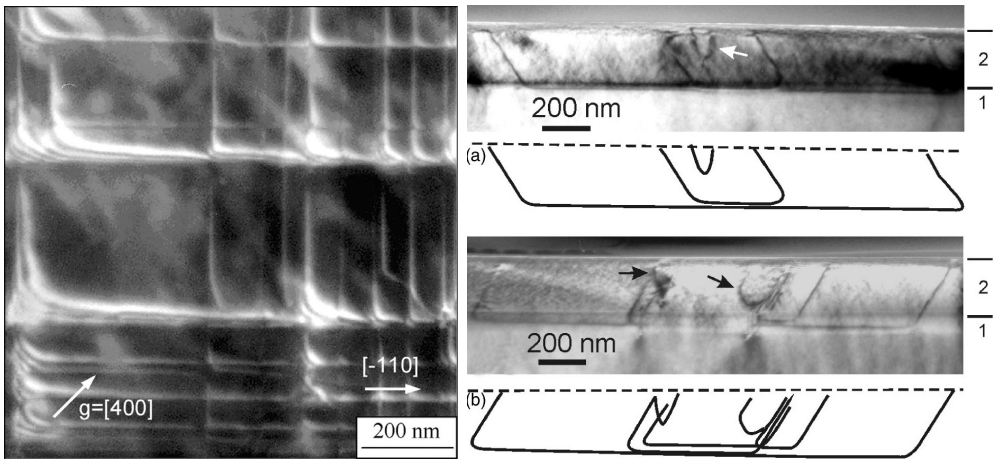

FIGURE 4.1: (Left) Plan-view dark-field TEM of 100 nm $Si_{0.7}Ge_{0.3}$ on (001) Si showing orthogonal arrays of misfit dislocations. The curved features at the dislocation intersections are moiré fringes due to superimposed diffraction from the layer and the substrate [138]. (Right) TEM image of the cross-section (110) of the GeSi/Si(001) heterostructure after annealing at 350°C during 10 min. The schemes below show misfit dislocations with threading branches and dislocation half-loops propagating from the surface. 1-Si substrate, 2-GeSi film. Two-beam condition, g=[$\bar{2}$20]. [139]

in low-mismatched films and the advantages and limitations of several techniques existing in literature aimed to govern dislocations in epitaxial semiconductor two-dimensional (2D) layers. Then we present a novel strategy for efficient dislocation engineering. In particular, we demonstrate that by suitably patterning Si(001) substrates with {111} trenches or pits, it is possible to select preferential nucleation and positioning sites for dislocations and confine them in pre-determined $Si_{1-x}Ge_x$ film areas. Finite element calculations and dislocation dynamics simulations are presented in order to prove this concept and are successfully compared with tailored experiments of SiGe deposition on nanopatterned Si(001) substrates, performed at the University of Linz in the group of Prof. F. Schäffler.

4.1 Plastic relaxation in heteroepitaxial films

4.1.1 Threading dislocation reduction

In heteroepitaxial films most of the dislocations are located at the interface, so as to relieve the misfit strain, but a certain density of misfit dislocations will have segments that 'thread' from the substrate, and interfaces to the surface and into the epitaxial layer region. These segments are the so called threading dislocations. Some of these are visible in the image in Fig. 4.1 (right panel). Over the past decades, several approaches have been proposed that aim to reduce the threading dislocation density or to segregate dislocations in non-active areas of the devices. For example stepped graded layers allow to relax the misfit strain by dislocation formation at the different interfaces, reducing the threading dislocation density close to the surface where the device is placed [140, 141]. Recently, Ge [142] or GaAs [143] selective area deposition in oxide windows, or on small SiGe or GaAs

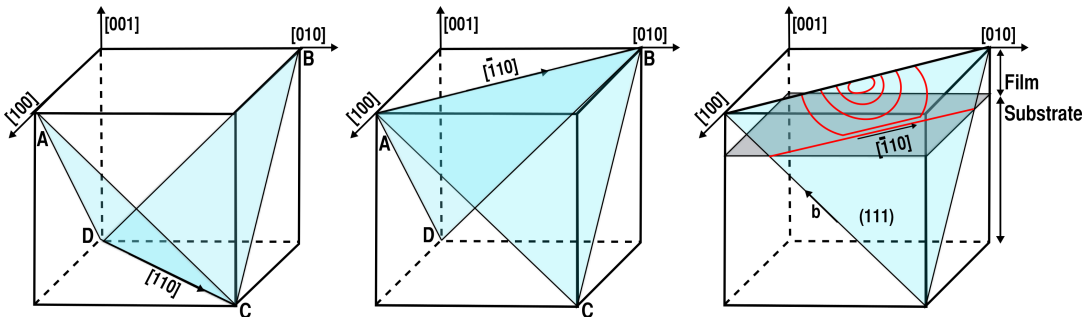

FIGURE 4.2: Dislocation geometries in Si/Ge films grown on top of Si(001) substrates. Dislocations with ⟨110⟩ Burgers vectors, (AC, AD, BC and BD), propagate in the {111} slip planes that intersect the (001) interface along the [110] (a) and [$\bar{1}$10] directions. (c) Dislocations are expected to nucleate as half-loops at the film surface, propagate in one (111) slip plane and deposit a 60°misfit segment at the film/substrate interface.

mesas [144, 145], have allowed the blocking of threading dislocations. Still, the nucleation sites are hard to control and the growth on oxide regions provides defects or polycrystalline material.
The goal of the following work is to propose a new strategy for efficient dislocation engineering and to fabricate large film areas free of detrimental dislocations, without using non-connected substrates or growing the epitaxial layer in oxide windows.

4.1.2 Dislocations in heteroepitaxial SiGe films

In low misfit SiGe films on Si(001) substrates, 60°dislocations are commonly observed at the substrate/epilayer interface. This is in good agreement with the prediction that, in materials with FCC or zinc blend crystal structures, the favorite dislocations are characterized by ⟨110⟩{111} slip systems, i.e. they have Burgers vector in the ⟨110⟩ directions and {111} slip planes. These defects propagate by glide in the low energy {111} slip planes, eventually depositing a misfit segment at the intersection between their slip planes and the (001) interface, as drawn in Fig. 4.2. As a consequence, a network of 60°misfit dislocations along the [110] and the [$\bar{1}$10] directions is produced. An example of such dislocation pattern is shown in the transmission electron microscopy (TEM) image in Fig. 4.1. The presence of a dislocation network usually results in a characteristic undulating surface morphology known as cross hatch that is readily observed by Atomic Force Microscopy (AFM), allowing for preliminary experimental characterization without employing destructive techniques. This behavior and morphology occurs in many lattice-mismatched semiconductor systems including SiGe/Si and various III–V compound heterostructures [146–151].

In a perfectly flat epitaxial film, there are no preferential sites for dislocation formation, because the stress field is homogeneous in the entire volume. Consequently, dislocations nucleate at unpredictable positions, most probably, where a defect coming from the substrate, a heterogeneity in composition or a surface step is present [152, 153]. Point defects, resulting from contamination of the substrate surface and agglomeration of impurities, as SiC precipitates [154], crystalline inclusions and Ge-rich platelets [139, 155], can be active

dislocation sources [39], especially in the very low temperature growth regime. These defects can be reduced by optimization of the growth process and surface preparation prior to epitaxial deposition, in order to avoid dislocation nucleation at random heterogeneities (growth defects) positions. Nucleation of dislocation half-loops at the film surface is an other competitive mechanism for dislocation formation, as confirmed by several experimental observations [156, 157]. In particular, this mechanism is expected to be dominant during the deposition of epitaxial layers close to the thermodynamic conditions (low rates and high growth temperatures may help in this direction) and by using substrates with a small defect densities. In Fig. 4.2(c) this process is schematically described. First a small dislocation half-loop nucleates at the surface. If the loop reaches a critical size [24], it expands in its slip plane under the epitaxial stress field and eventually deposits a misfit segment at the film/substrate interface. The misfit segment length increases through the motion of the two dislocation segments connected to the surface (threading dislocations), further promoting the plastic relaxation. Even though, in low misfit films, the predicted nucleation barrier for homogeneous nucleation is considerably high [158], atomistic simulation of dislocations emitted by a surface step on the (100) surface of Si and parallel to $\langle 011 \rangle$ directions under uniaxial stress (tension or compression) have demonstrated that the nucleation barrier can be reduced in correspondence of a surface step [159–161]. This strongly supports the mechanism of dislocation nucleation from surface steps.

4.2 Dislocation trapping by substrate nano-patterning

The nucleation of dislocation loops or semi-loops at a surface or interface or at a heterogeneous site, relies on the formation of critical-size loops. The critical size for loop expansion depends on the magnitude of the stress field. The higher is the stress field, the smaller is the critical loop size and the energy barrier for dislocation nucleation [158, 162], as can be also deduced form Eq. 2.9. In particular, stress concentrations are demonstrated to be preferential nucleation sites for dislocations [40, 162–165]. The main idea at the base of our strategy to confine dislocations, is to produce regions, at regular positions in the epitaxial layer, where the magnitude of stress field is locally higher than in the rest of the film volume, so as to induce preferential dislocation nucleation at controlled sites. In particular, we show that this result can be achieved by growing an epitaxial film on top of a Si(001) substrate patterned with a regular array of {111} trenches or pits. Moreover, by elastic energy calculations it is possible to demonstrate that {111} interface planes are preferential sites, with respect to the {001} planes, not only for dislocation nucleation, but also for their positioning. By exploiting stress induced nucleation at predetermined sites and preferential positioning on {111} interface planes, we expect to trap dislocations in selected areas, leaving large film regions, free of detrimental defects and suitable for device integration.

In this work, we will consider low misfit SiGe films. These are characterized by a lower dislocation density, with respect to high misfit layers, and can be used to determine some features of the processes of dislocation formation, propagation and trapping by performing computationally less expensive simulations. Also, in high-mismatched systems, islands nu-

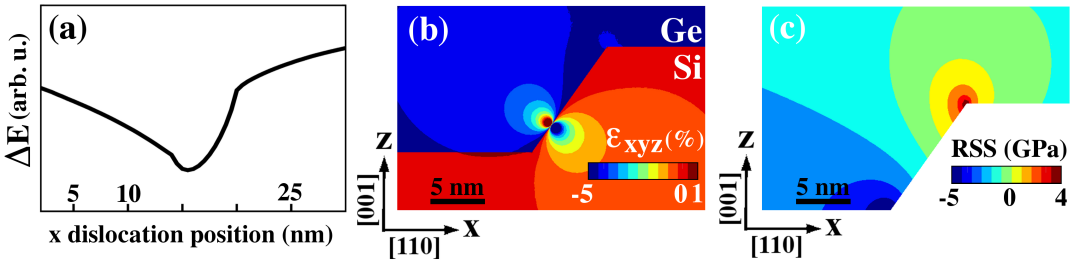

FIGURE 4.3: (a) Elastic energy of a 60°MS parallel to the $[\bar{1}10]$ direction with $\mathbf{b} = a_{Ge}[011]/2$ as a function of the x position along the Ge/Si interface. (b) Hydrostatic strain map of the dislocation in its energy minimum. Nucleation of such dislocations is favorable at the upper edge of the $(\bar{1}\bar{1}1)$ plane, where RSS is maximum (c).

cleate after the deposition of few monolayers. However, the dislocation trapping behavior presented below is expected to be quite general, at least for $Si_{1-x}Ge_x$ and III-V epitaxial films on patterned Si (001) substrates, leading to a confinement of detrimental dislocations in selected regions.

4.3 Dislocation trapping in {111} trench arrays

As introduced in the previous section, in epitaxial SiGe planar films, there are no preferential sites for dislocation nucleation or positioning. This generally lead to a cross network of 60°misfit segments (MS) parallel to the [110] and $[\bar{1}10]$ directions and connected to the surface by threading dislocation (TD) segments at random positions in the film volume. The lattice deformation induced by a straight 60°dislocation is composed of an expanded and a compressed lobe, which are mirror symmetric with respect to the {111} plane. It is easy to show by suitable Finite Element Method (FEM) calculations [82, 166], that the lowest elastic energy is obtained when the MS lie on a {111} interface between SiGe and Si. In this configuration the Burgers vector lies in the interfacial plane and the relaxation of in-plane strain components is maximized. It is clear, that the strain relief induced by ⟨110⟩{111} MS is enhanced in {111} oriented flat films. Still, the film is homogeneous and no selective dislocation formation can be induced. However, by growing SiGe films on top of nano-structured substrates which expose {111} facets adjacent to the conventional (001) planes, it is feasible to create preferential sites for MS positioning. In Fig. 4.3(a), we report the elastic energy of a MS parallel to the $[\bar{1}10]$ direction, with Burgers vector $\mathbf{b} = a_{Ge}[011]/2$ (a_{Ge} is the Germanium lattice parameter), as a function of the x position along the Ge/Si interface, patterned as shown in Fig. 4.3(b). The pattern consists of two (001) and one $(\bar{1}\bar{1}1)$ oriented surfaces. The energy minimum corresponds to the MS in the $(\bar{1}\bar{1}1)$ interface plane, where the stress field generated by the dislocation enhances the total strain release. The map of the hydrostatic strain in such a position is shown in Fig. 4.3(b). Fig. 4.3(c) maps the variation of the Resolved Shear Stress (RSS) in a (110) cross section of the same pattern. The RSS is maximum at the upper intersection between the $(\bar{1}\bar{1}1)$ and (001) planes. Here, dislocations will nucleate [3] and eventually glide within the

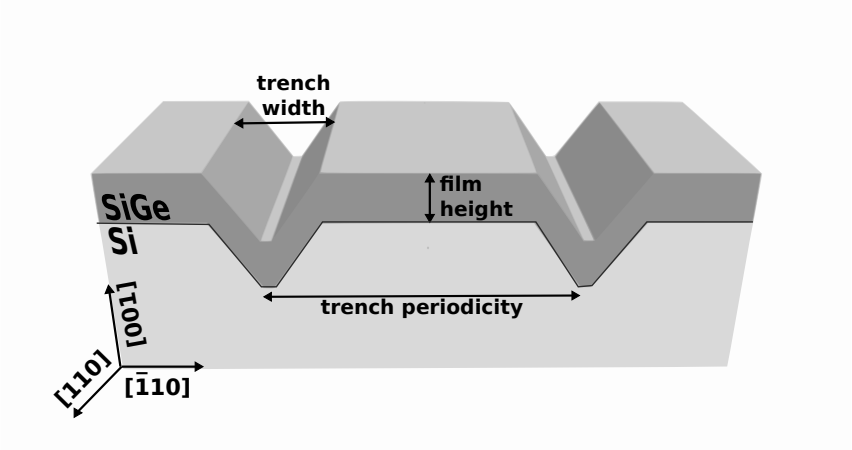

FIGURE 4.4: Trench pattern geometry. {111} facetted trenches, carved in the Si substrate, run parallel to the $\bar{1}10$ direction and are homogeneously spaced along the perpendicular [110] direction. A conformal SiGe film is deposited on top of it.

$(\bar{1}\bar{1}1)$ interface plane to the energy minimum position.

Starting from this behavior, we show that for low misfit SiGe films characterized by thicknesses far above the predicted thermodynamic [24, 26] and kinetic [33] critical values at the same Ge content, it is possible to find a suitable pattern geometry in order to confine such MS.

Let us consider a Si (001) substrate patterned with 350 nm wide trenches, periodically repeated along the [110] direction, and covered by a conformal, 160 nm thick $Si_{0.7}Ge_{0.3}$ film, as shown in Fig. 4.4. Since the trenches length is considerably larger than their width and periodicity, we have adopted a simplified 2D geometry. Both the trenches and the MS are assumed to be ideally infinite and parallel to the $[\bar{1}10]$ direction. We see from the FEM strain map in Fig. 4.5(a) that the presence of {111}-terminated trenches allows for a significant elastic relaxation of the ε_{xx} component in the epilayer even in the absence of dislocations. We found that in the coherent system with a trench spacing of 1.5 μm the average residual strain ε_{xx} in the epilayer is $\sim$-6.7·10^{-3}, i.e. much lower than expected for a $Si_{0.7}Ge_{0.3}$ film (1.2·10^{-2}). Moreover, the elastic strain field is highly modulated both in the x and z direction. Hence, we expect a reduced number of dislocation lines in the $[\bar{1}10]$ direction. Considering the same pattern geometry, we calculated the equilibrium configuration of multiple dislocations in order to demonstrate that substrate patterning with {111} trenches is a suitable strategy for confining MS. In particular, for a given number of dislocations and their initial positions, we can calculate the force acting on each of them using the Peach-Koehler equation, as defined in Eq. 3.40:

$$\boldsymbol{F} = (\boldsymbol{\sigma}(\boldsymbol{r}) \cdot \boldsymbol{b}) \times \boldsymbol{\xi}(\boldsymbol{r}) \,, \tag{4.1}$$

where $\boldsymbol{b}$ and $\boldsymbol{\xi}$ are the Burgers vector and the line vector of the dislocation, respectively, and $\boldsymbol{r} = (x, y, z)$ is the dislocation position. $\boldsymbol{\sigma}(\boldsymbol{r}) = \boldsymbol{\sigma}_{epi}(\boldsymbol{r}) + \boldsymbol{\sigma}_{disl}(\boldsymbol{r})$ is the position-dependent stress tensor given by the superposition of the FEM-calculated epitaxial stress field $\boldsymbol{\sigma}_{epi}$ and the elastic field provided by all the dislocations in the system $\boldsymbol{\sigma}_{disl}$. The latter was

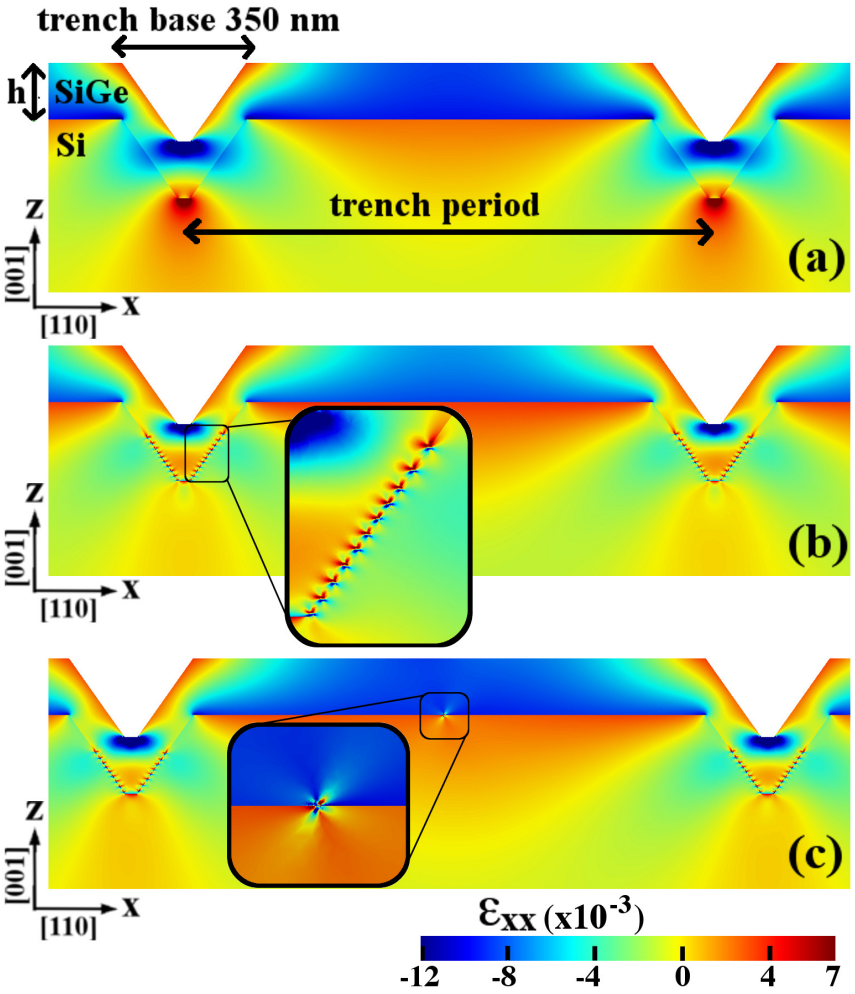

FIGURE 4.5: Map of the strain ε_{xx} in the xz-plane for the coherent (a) and dislocated (b) system with a trench period of 1.5 μm and a film thickness h of 160 nm. Up to trench periods equal to 1.5 μm all dislocations (21 for the reported periodicity) are confined inside the trenches (b), while for larger periods (here: 1.8 μm), a few dislocations are expected between the trenches (c).

calculated using the analytical formulation given in Ref. [110]. In the forces computation, the surface-dislocation interactions have been neglected. This assumption is quite good, considering that this contribution is less than 1% of the total force when the dislocation is tens of nanometers far from the surface and the here considered film thickness is greater than 100 nm. The equilibrium configuration was computed by using the steepest-descent algorithm. A random distribution of dislocations is generated, forces are calculated using Eq. 4.1, and dislocations are moved along the force directions in the film volume, until the forces acting on each of them is zero. The equilibrium configuration is then obtained by repeating the elastic energy minimization for different initial dislocation positions and increasing their number up to the maximum allowed by the film thickness and trench periodicity.

In the minimum energy configuration the dislocations are distributed exclusively in the

{111} interfaces inside the trenches, as long as the trench period is $\leq$1.5 μm, (Fig. 4.5(b)). When the trench period exceeds 1.5 μm, full dislocation confinement in the trenches is lost. For a trench period of 1.8 μm, for instance, we predict that a few dislocations are also located in the (001) interface between the trenches, as highlighted in the inset in Fig. 4.5(c). Thus, by varying both pattern geometry and Ge content it is possible to tune the range of trench periods where misfit dislocations become entirely confined inside the trenches.

Interpretation of MBE deposition experiments of SiGe on {111} trench patterned Si(001) substrate

The validation of our model predictions by tailored experiments, performed at the University of Linz and published in Ref. [167], is presented below. Moreover, we reported the analysis of the RSS for MS perpendicular to the trench length, that allowed us to interpret some of the experimental observations described above.
Trenches with well-defined {111} facets, with a periodicity of 2 μm (i.e. slightly beyond the critical value obtained by the above described simulations) were fabricated by following a similar procedure as described in Ref. [168]. Regular arrays of trenches oriented along the [$\bar{1}$10] direction were defined by electron beam lithography on a Si (001) substrate covered with 70 nm of SiN_x. The pattern was transferred into the SiN_x layer via reactive ion etching to provide a hard mask for the subsequent anisotropic Si etching in Tetramethylammonium Hydroxide at 80°C. Since the etching rate in the Si <001> directions is $\sim$ 0.3 μm/min whereas the one for Si <111> is as small as $\sim$ 0.01 μm/min, trenches with well defined {111} side facets result [169]. The width and the depth of these trenches were defined by the size of the hard mask openings, here 350 nm and 250 nm, respectively, to match the model assumptions. The patterned substrates were then chemically pre-cleaned with a final dip in hydrofluoric acid and transferred to a Riber SIVA 45 solid source molecular beam epitaxy (MBE) system. After in-situ annealing at 700°C for 45 minutes, a 45 nm thick Si buffer layer was deposited at a rate of 0.6 Å/s at a temperature that was ramped up from 450°C to 550°C. An overcritical [26, 33] 160 nm thick $Si_{0.7}Ge_{0.3}$ layer was subsequently grown at T_{Ge}= 550°C, with rates of 0.18 Å/s and 0.41 Å/s for Ge and Si, respectively.

Fig. 4.6(a), shows an AFM image taken at the boundary of the trench patterned area. Evidently, most of the [$\bar{1}$10] oriented dislocations propagate as bundles from the sidewall areas of the trenches into the non-patterned area. Since the AFM measurements are only sensitive to the surface-footprint of several bunched dislocations, TEM investigations were carried out to identify individual misfit and threading segments. Also in this case, the region between the patterned and the non-patterned areas was analyzed . In Fig. 4.6(d) one can see that most dislocations parallel to the [$\bar{1}$10] direction are confined along the trenches and extend into the non-patterned area, confirming the model predictions and supporting the interpretation of the AFM results. As predicted, only few [$\bar{1}$10] oriented dislocation lines are observed between trenches, since we are slightly overcritical with respect to the 1.5 μm trench spacing. Both the AFM and the TEM images also reveal that perpendicular to the trenches MS run from trench to trench as a dense network with

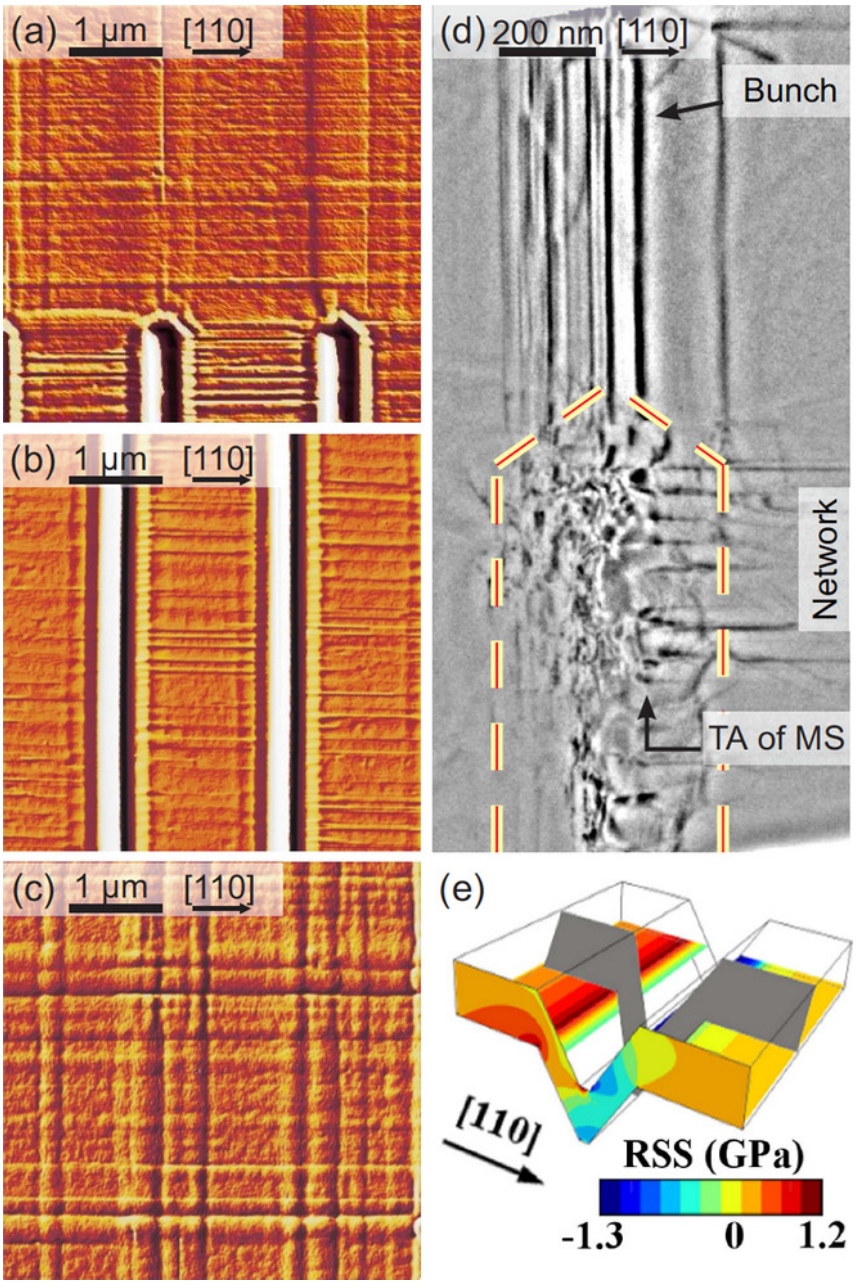

FIGURE 4.6: AFM images of the areas, where the {111} trench pattern ends (a), from the middle of the patterned (b) and non-patterned field (c), obtained after deposition of 160 nm $Si_{0.7}Ge_{0.3}$. Color coding corresponds to surface sensitive derivative. TEM image of the end of a trench (d), where dislocations are confined in bunches along the trench. Trenches are outlined to guide eye. (e) RSS calculated for a 60°dislocation perpendicular to the trenches (parallel to the [110] with $\mathbf{b} = a_{SiGe}[011]/2$ and $(1\bar{1}1)$ glide plane). [167]

narrow, rather regular spacing, (Fig. 4.6(b,d)). This is probably due to the high RSS at the upper trench edges, which provides preferential sites for homogeneous dislocation nucleation in the patterned area. In Fig. 4.6(e) the RSS calculated for a 60°straight dislocation parallel to the [110] direction (i.e. perpendicular to the trenches), with Burgers vector $\mathbf{b} = a_{SiGe}[011]/2$ (a_{SiGe} is the $Si_{0.7}Ge_{0.3}$ alloy lattice parameter), is plotted. Since the RSS reaches its maximum at the upper trench edge where it is much higher than in flat films, we expect dislocations to be more easily nucleated in films grown on such patterned substrates. This effect allows for the formation of a homogenous distribution of dislocations perpendicular to the trenches. In contrast, in the non-patterned area, Fig. 4.6(c), an irregular network of bundles of dislocations is observed, giving rise to a superficial cross hatch morphology along the [110] and the $[\bar{1}10]$ directions[170]. We see that most TDs are located in the trenches, where they end on a sidewall surface, Fig. 4.6(d). The area between the trenches has a much lower density of TD. Their occurrence is mainly associated with occasional stacking faults caused by not-yet optimized growth conditions on the {111} sidewalls of the trenches.

x_{Ge}	trench width	film thickness	max. periodicity
0.10	700 nm	200 nm	3.0 μm
0.15	250 nm	160 nm	1.5 μm
0.30	300 nm	160 nm	0.8 μm

TABLE 4.1: Maxmimum trench periodicity predicted to lead to full MS confinement inside the trenches obtained by varying both the geometrical parameters (trench width and film thickness) and the Ge content x in $Si_{1-x}Ge_x$ films grown on a {111}trench-patterned Si (001) substrate.

In conclusion, the predictions based on our simplified 2D model and the presented experimental results clearly suggest that substrate patterning with {111}-terminated trenches is an effective method for trapping MS parallel to the trenches. Their density is low, because the trench geometry allows for a significant elastic strain relaxation. In contrast, the strain component along the trench direction is plastically relaxed by a quite regular array of misfit segments that run from trench to trench. The threading dislocations are effectively trapped on the open sidewalls of the trenches. Even though the model does not capture the evolution of dislocation lines in 3D, our approach can be used to predict the expected maximum periodicity which allow for full MS (parallel to the trenches) confinement inside the trenches, varying the pattern geometry (trench width, film thickness) and the epilayer Ge content. In Tab. 4.1 we summarized some of these calculations. As a result, by tuning Ge content, film thickness and trench periodicity, it is possible to tailor the residual ε_{xx} strain in the large film areas ($\sim$1 μm^2) free of threading dislocations between the trenches. In Section 4.4, we present 3D discrete dislocation dynamics simulations, in films conformal to pit-patterned substrates, that fully capture the evolution of dislocations in 3D structures and confirm our predictions based on 2D FEM calculations.

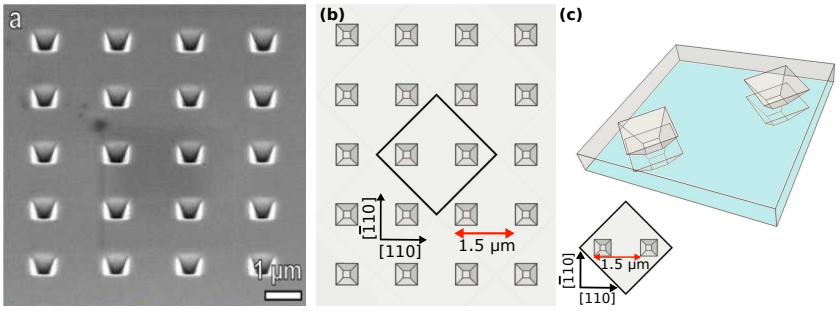

FIGURE 4.7: (a) Scanning electron microscopy image of a Si(001) template patterned with an array of pits with 111 side facets. (b) Pit pattern geometry used in the simulations. The periodicity is 1.5 μm. (c) DD simulation cell. The SiGe/Si interface is colored in blue.

4.4 Dislocation ordering induced by pit-patterned substrates

In Section 4.3, we have shown by FEM predictions that {111} faceted and ⟨110⟩-oriented trenches in Si (001) substrates are favorable trapping sites for MS parallel to the trenches in conformal low misfit SiGe films. In addition, we investigated the formation of dislocations at the Si/SiGe interface and orthogonal to the periodic trench array, which form a rather regular network minimizing elastic energy. The latter dislocations are found to start and end at the trenches ($\sim$2 μm apart), because the calculated resolved shear stress (RSS) at the trench edges is considerably higher than in the rest of the film, hence promoting preferential dislocation nucleation and stress trapping sites. However, for virtually infinite trench arrays, only MS parallel to the trenches were successfully confined and no planar region free of dislocations was ever produced, as suitable for device integration.

In order to achieve dislocation gettering along both the two orthogonal [110] and [$\bar{1}$10] directions we studied dislocation evolution in SiGe films grown on top of Si(001) substrates patterned by a regular array of {111}-faceted pits. These are similar in size and spacing to the trench case, and oriented in a square network along ⟨110⟩ directions. If the heterogeneity induced by the pits in the epitaxial stress field is as effective as for the trenches in producing large stresses at the pit edges, a pattern of dislocations confined along the pit lines is expected. This pattern should ideally leave squared areas in the order of one-two microns per side free of misfit segments. As the pit array is expected to produce a complex inhomogeneous strain field in the SiGe film, it is not easy to predict the extent of the dislocation gettering process. To this end, three-dimensional dislocation dynamics (DD) is the natural tool to access the evolution of a large density of dislocation lines.

Pit induced epitaxial stress field in SiGe films

Before investigating dislocation propagation in SiGe films grown on pit patterned substrates, let us analyze the epitaxial stress field produced by such a structure. The elastic field solution for a plastically unrelaxed structure, as sketched in Fig. 4.7(c), was calculated by FEM. Here, a conformal 250 nm thick $Si_{0.85}Ge_{0.15}$ film grown on a {111}

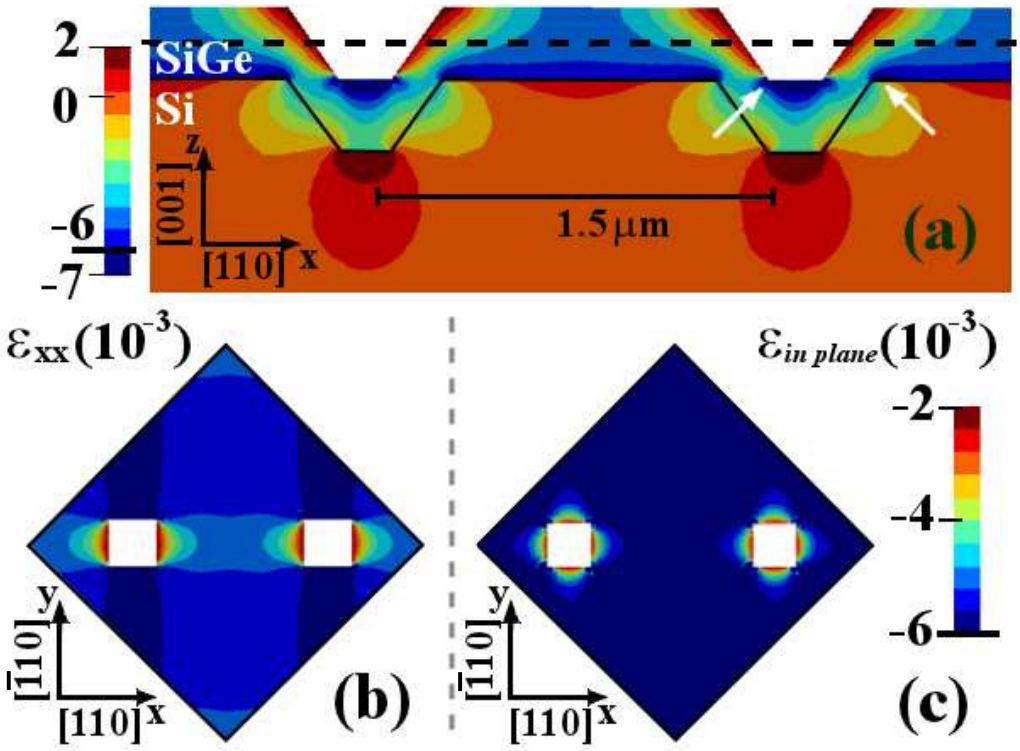

FIGURE 4.8: Elastic strain field in a conformal, $Si_{0.85}Ge_{0.15}$ film grown on {111} pit patterned substrate. The strain component ε_{xx} is plotted (a) in a plane orthogonal to the $[\bar{1}10]$ direction (y axis), which cut in two halves the pits, and (b) in a plane perpendicular to the [001] direction (z axis), 125 nm deep from the top (001) surface. (c) The in-plane strain ε_{in} in a plane perpendicular to the [001] direction (z axis) as in (b).

pit-patterned Si(001) substrate has been considered. The pits are 540 nm in width and 250 nm in depth, and the pattern periodicity is 1.5 μm. Pits are regularly repeated along the [110] and the $[\bar{1}10]$ directions. These parameters were selected in order to compare our results to tailored MBE deposition experiments of SiGe films on top of Si(001) substrates patterned by a regular array of {111}-faceted pits.

The heterogeneity of strain in the film is visualized in Fig. 4.8(a-b), where the ε_{xx} strain tensor component is plotted in a $(\bar{1}10)$ plane (the y axis) and in (001) plane (the z axis), respectively. In the two cutting planes, we see that the pit surfaces allow for a partial elastic relaxation of the in-plane strain close to the pits, while in the other film regions, ε_{xx} is almost equal to the value expected in a flat film with the same Ge content ($\sim -6 \times 10^{-3}$). Similar conclusions can be extracted by looking at the biaxial strain map, in Fig. 4.8(c), plotted in a (001) plane. In Tab. 4.2, we compared the average values of the biaxial strain, the ε_{xx} strain tensor component and the elastic energy density in a 250 nm thick $Si_{0.85}Ge_{0.15}$ film grown on a flat and on a pit-patterned (as described above) Si substrate. By looking at the values in Tab. 4.2, it is evident that the total elastic relaxation induced by the pits is weak and large areas in the film are as strained as in the flat film case. However, a second important effect associated to the existence of the

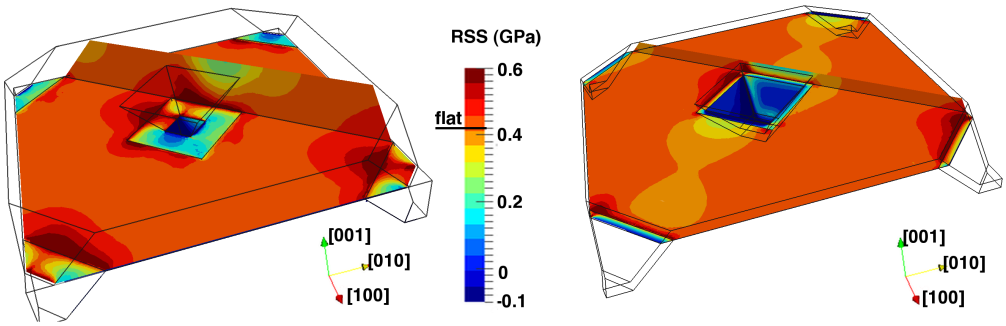

FIGURE 4.9: Variation of the resolved shear stress (RSS) calculated for the $[011](1\bar{1}1)$ slip system, in a conformal 250 nm thick (a) and 60 nm thick (b) $Si_{0.85}Ge_{0.15}$ film, at the (001) film/substrate interface and in a $(1\bar{1}1)$ possible dislocation glide plane of the film.

pits can be realized in the two stress maps. Some edges at the top and bottom surface of the pits induce stress concentrations and provide in the film very high stress sites where dislocation nucleation and multiplication is going to be more favorable.

	flat	pit-pattern (periodicity 1.5 μm)
$\bar{\varepsilon}_{xx}$	-6.0 $\times 10^{-3}$	-5.5 $\times 10^{-3}$
$\bar{\varepsilon}_{biaxial}$	-6.0 $\times 10^{-3}$	-5.5 $\times 10^{-3}$
$\rho_{elastic}$ (eV/nm^3)	4.0 $\times 10^{-2}$	3.8 $\times 10^{-2}$

TABLE 4.2: Average values of the biaxial strain, the x strain component and the elastic energy density of a 250 nm thick $Si_{0.85}Ge_{0.15}$ grown on a flat substrate and grown on the {111}pit-pattern geometry with periodicity of 1.5 μm both in the [110] and the $[\bar{1}10]$ direction. The pit base is 540 nm.

To better quantify such an effect, we plot in Fig. 4.9(a), for one of the active slip system experimentally observed ($[011](1\bar{1}1)$), the variation of its resolved shear stress (RSS) at the (001) film/substrate interface and in a $(1\bar{1}1)$ dislocation glide plane cutting the film close to a pit. From this figure, it is clear that the RSS is maximum in the proximity of the pit edges, while it is considerably lower in the remaining film volume (approximately equal to the value expected for a flat $Si_{0.85}Ge_{0.15}$ film, $\sim$ 0.42 GPa). Therefore, close to the pits a small area exists where dislocations on the tested slip system should be preferentially nucleated. Similarly to Fig. 4.9(a), we show in Fig. 4.9(b) the variation of the RSS for the $[011](1\bar{1}1)$ slip system, calculated for a 60 nm thick film. We observe that with the decreasing film thickness, the areas where the RSS is high become more localized close to pit edges. Thus, selective dislocation nucleation should be effective from the very beginning of the film growth, provided that the critical thickness for dislocation nucleation is overcome [159, 162]. Similar results were obtained for the other active slip systems.

Dislocation dynamics simulations
Enhanced dislocation loops evolution from the pit sites

To prove that the stress field modulation induced in a film by {111}pit substrate patterning leads to dislocation trapping along the pit lines, dislocation dynamics simulations were performed. This simulation method is known to give accurate results in many problems of crystal plasticity including plastic relaxation in micro and nanometer size objects [115–117]. Following the approach first proposed in Ref. [125] for epitaxial islands, we addressed the evolution of the dislocation microstructure in a pit patterned film by applying the epitaxial strain field calculated above by FEM, as external load in the DD simulations. For the simulation results presented in this section we considered the $Si_{0.85}Ge_{0.15}$ film geometry used for the FEM calculations (see Fig. 4.7(c)). Periodic boundary conditions are applied in the [100] and [010] directions to reproduce the pit pattern periodicity.

As the early stages of dislocation nucleation from atomic defects cannot be reproduced at the DD simulations scale, we explore the film volume by testing the possibility to expand a new dislocation loop with a small initial radius R_c corresponding to a reference critical stress for nucleation. In a homogeneous flat film, a dislocation half-loop nucleated at the surface, will evolve in the film provided that it reaches the critical size R_c. [24, 26] In particular, neglecting kinetic limitations, a half-loop will expand and deposit a misfit segment, when its radius R is such that the following relation is satisfied:

$$R \cdot sin\phi \geq R_c \cdot sin\phi = h_c$$

where ϕ is the angle between the glide plane and the (001) interface plane (here ϕ=54,7°, $sin\phi = \sqrt{2/3}$) and h_c is the thermodynamic critical layer thickness for dislocation formation as derived in Ref. [26] and reported in Eq. 2.7. Similarly, in an overcritical film dislocation loops with radius $R \geq R_c$ will expand and deposit a misfit segment, while loops with radius $R \leq R_c$ will collapse on themselves. In our simulations we exploited the equivalence of these two criteria in order to test where dislocation loops would preferentially nucleate in the highly heterogeneous stress field, as for epitaxial SiGe films deposited on top of pit-patterned substrates. In Fig. 4.10, 4.11 and 4.12, we show the evolution of a random distribution of dislocation loops with different loop size. Results obtained by inserting loops with radius R of 32, 30 and 25 nm, are shown in Fig. 4.10, 4.11 and 4.12 respectively. The three values were chosen in order to study the evolution of dislocation loops with an over-critical, critical and sub-critical radius for dislocation formation in a flat $Si_{0.85}Ge_{0.15}$ film. As we can see in Fig. 4.10, evolution of dislocation loops with $R \geq R_c$ is similar to the results obtained for a flat film: all the loops expand in time creating a random network of misfit (along the [110] and [$\bar{1}$10] directions) and threading dislocation segments. Decreasing the loop radius R until the critical value R_c, we observe that some loops in between the pits do not expand themselves, because the stress field is slightly reduced there, thanks to the elastic relaxation induced by the pit free surfaces (see Fig. 4.8 and Fig. 4.9). Still, a random network of dislocations is observed, as shown in Fig. 4.11. If we consider now the evolution of loops with a sub-critical radius, shown in Fig. 4.12, a different result is obtained. As expected, such dislocation loops expand only where the RSS is significantly higher than the RSS value obtained in a biaxially strained thin

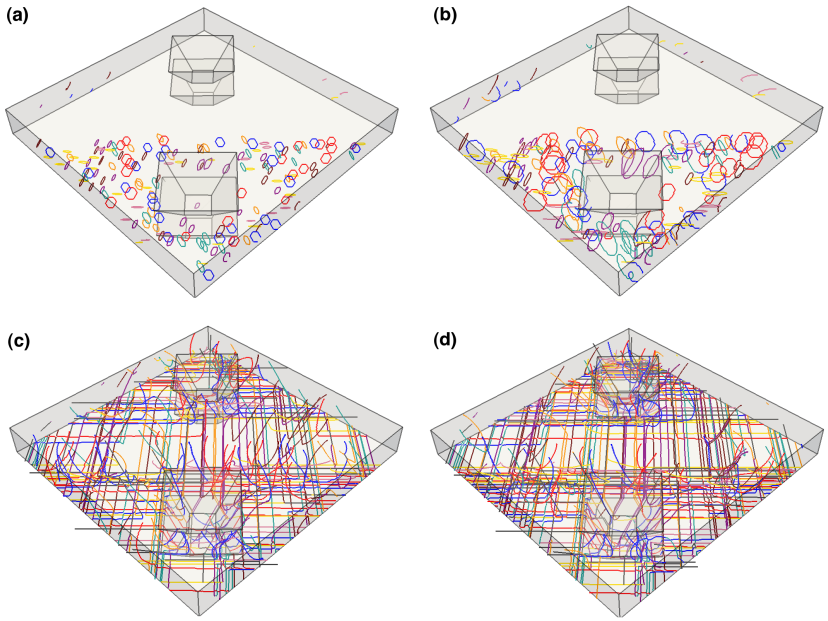

FIGURE 4.10: Dislocation evolution a different times in $Si_{0.85}Ge_{0.15}$ film grown on a {111} pit-patterned Si (001) substrate, starting from an initial random distribution of dislocation loops. The pattern periodicity is 1.5 μm in both the [110] and the [$\bar{1}$10] directions. The loop radii are larger than 30 nm.

film with the same Ge content. Thus, only dislocation loops close to the pit edges will expand. As a result, misfit dislocations are deposited only in between the pits, or parallel to the pit lines but close to the pit edges, leaving large areas dislocation free.

Dislocation dynamics simulations: progressive plastic relaxation with time and threading dislocation trapping

Dislocation dynamics simulations starting from a fixed number of dislocation sources demonstrated that nucleation and propagation of dislocations is favorable at the pit edges. In experiments, dislocations nucleate in time at different film sites eventually covering large distances before the mobile TD are effectively stopped, by interacting with other threading or misfit segments. In order to reproduce such a behavior, we employed the nucleation procedure, described in Section 3.5.3, to nucleate small dislocation loops, periodically in time, and describe the progressive plastic relaxation process in thin films. In this case the nucleation rule applied can be summarized as follows. At predefined time intervals Δt, we randomly select the coordinates of a nucleation site inside the simulated volume. First, a loop discretized in eight elementary segments is defined in its glide plane. Second, the forces on each segment are calculated and resolved in the dislocation glide plane. These two steps are repeated repeated for all the active slip systems and the dislocation loop undergoing the maximum forces is selected. If the resulting forces act, on average, to expand the loop, we effectively insert it in the simulated volume and leave it free to evolve

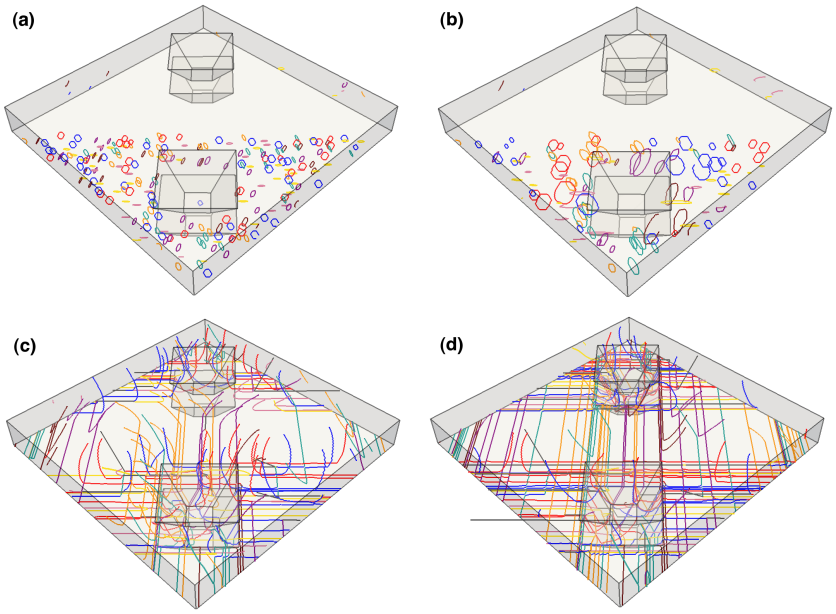

FIGURE 4.11: Dislocation evolution a different times in $Si_{0.85}Ge_{0.15}$ film grown on a {111} pit-patterned Si (001) substrate, starting from an initial random distribution of dislocation loops. The pattern periodicity is 1.5 μm in both the [110] and the [$\bar{1}$10] directions. The loop radii are equal to 30 nm.

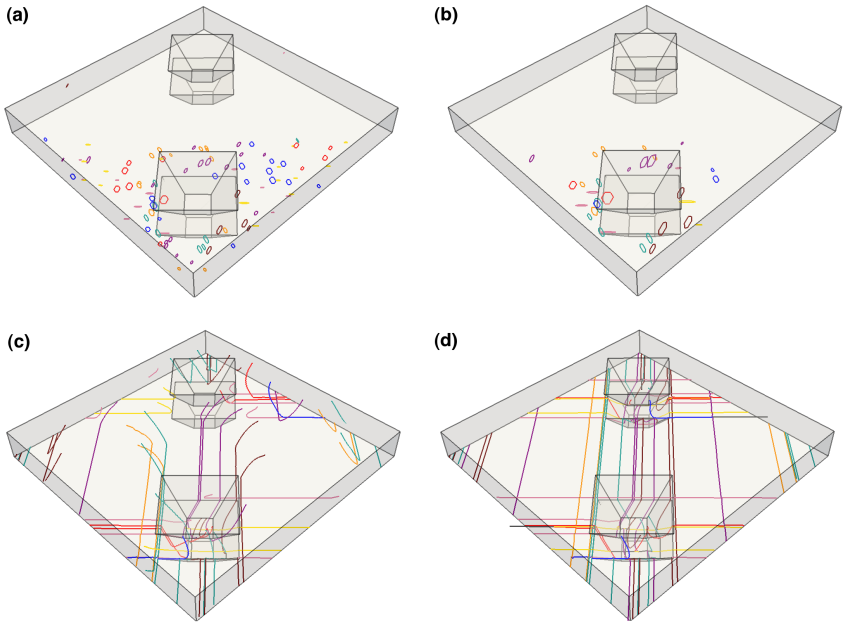

FIGURE 4.12: Dislocation evolution a different times in $Si_{0.85}Ge_{0.15}$ film grown on a {111} pit-patterned Si (001) substrate, starting from an initial random distribution of dislocation loops. The pattern periodicity is 1.5 μm in both the [110] and the [$\bar{1}$10] directions. The loop radii are equal to 25 nm.

together with the other existing dislocations. Otherwise, the procedure is repeated until one nucleation event is achieved. Plastic relaxation is achieved when no new dislocation loop can be nucleated and all the existing dislocations are immobile.
In Fig. 4.13, the results obtained by inserting dislocation loops of radius $R \sim$22 nm at time intervals $\Delta t = 1$ns, are presented. For the simulation the same $Si_{0.85}Ge_{0.15}$ film geometry used for the FEM calculations and the previous simulations was used (see Fig. 4.7(c)) and periodic boundary conditions were applied in the [100] and [010] directions. Dislocation nucleation is observed only in regions close to the pit edges, as illustrated by the small loop marked with an arrow in Fig. 4.13(a). This is why, misfit dislocations are deposited at the interface only in between the pits or close to the pit edges. The trapping of misfit dislocation in bundles between pits leaves the place for large areas free of dislocation in the partially relaxed film.
An other important result of the simulations is the following. All the dislocation loop radii we considered for the nucleation process in the simulation shown in Fig. 4.13 ($R \sim$22 nm) and for the evolution of the loop distribution in the simulation reported in Fig. 4.12 ($R \sim$25 nm), are lower than the corresponding solution in a flat $Si_{0.85}Ge_{0.15}$ film ($R \sim 28$ nm) as simply defined from classical theoretical models [24, 26]. This suggests that during the film growth, dislocation nucleation close to the pit takes place at earlier growth states than in a flat film or flat area. Hence, a large density of threading dislocations between pits have enough time to form before nucleation can take place in the other areas of the patterned film. This result justified the cross hatch morphology observed in the AFM images (Fig. 4.14(a-d)) and the dislocation microstructure found in the TEM characterization (Fig. 4.14(e-f)) of $Si_{0.85}Ge_{0.15}$ films deposited on top of {111} pit patterned Si(001) substrates, reported in the Section below. A last interesting feature indicated by the simulation is illustrated in Fig. 4.13(c). The mean free path of the dislocations nucleated at pits edges is relatively short. Indeed, mobile threading dislocation are found during the simulations to slow down or to stop in some regions close to the pit surfaces where the stress is much lower than in the rest of the film. This dynamical effect, explains why most threading segments terminate at the pit surfaces and justify the small density of threading segments observed between the pits in the experiments (see Fig. 4.14(e-f)).

Interpretation of MBE deposition experiments of SiGe on {111} pit patterned Si(001) substrate

In the following, we describe the experimental observations that further corroborate the possibility to use patterned substrates to confine dislocations. These experiments were performed at the University of Linz and published in Ref. [171].
The above presented simulations of dislocation evolution in SiGe films conformal to {111} pit patterned substrates shed light on the interpretation of such experimental findings.
Pits with {111} facets were defined on (001) oriented Si substrates, as shown in the scanning electron microscopy image reproduced in Fig. 4.7(a). Three different patterned samples with pits distanced by 1, 1.5 and 2 μm and aligned to the $\langle 110 \rangle$ directions were defined by following the technique described in Ref. [168, 171] and recalled in Section 4.3. The average pit area size (of quadratic shape) is $\sim 540 \times 540$ nm^2 and the corresponding

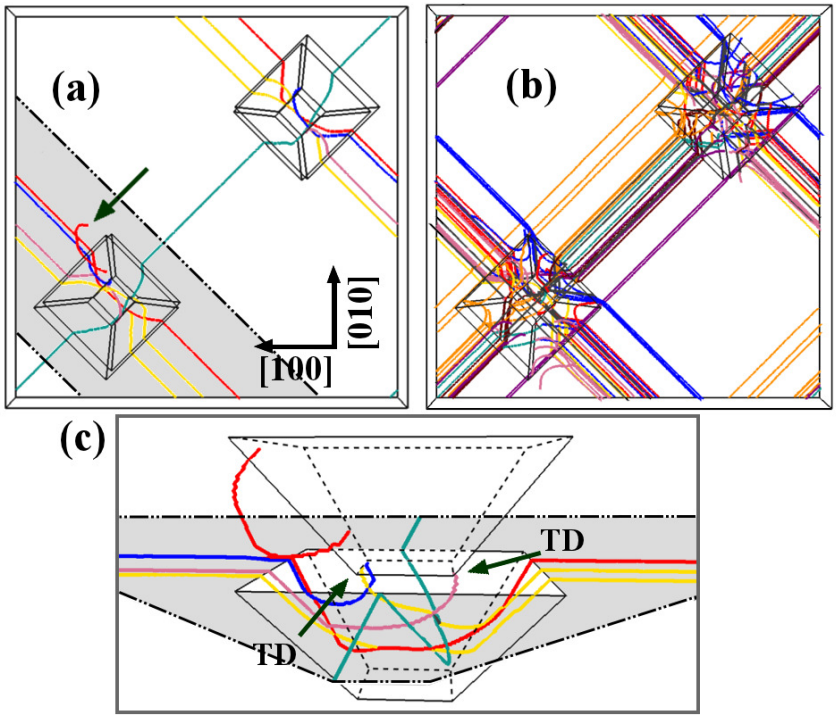

FIGURE 4.13: Intermediate (a) and fully relaxed microstructure of misfit dislocations (b) in a $Si_{0.85}Ge_{0.15}$ film grown on a {111} pit-patterned Si (001) substrate. Dislocation nucleation, as marked with an arrow in (a), are periodically tested in time. See the large area free of misfit dislocations in the final state (b). (c) A simulation magnification show that most threading dislocations (TD) in the microstructure end on the pit facets as indicated by arrows.

depth is ∼300 nm. On such substrates, first a Si buffer and then Ge is deposited by solid source molecular beam epitaxy and then a 250 nm thick $Si_{0.85}Ge_{0.15}$ layer was grown. Details on the pattering and growth processes can be found in [171].

In Fig. 4.14, are shown the AFM images taken from the sample characterized by a pit distance equal to 2 μm. Lines connecting the pit sidewalls are clearly visible, suggesting that most of the dislocations are bunched together and run from pit to pit [148]. Since the AFM measurements are only sensitive to the surface-footprint of bunched dislocations, and do not provide information about the type and origin of the surface roughness, TEM investigations were carried out to identify individual dislocations. In Fig. 4.14(e,f), plan view TEM images of the array with pits distanced by 1 μm are presented. One can see that most dislocations parallel to both the [110] and the [$\bar{1}$10] directions are confined along the pit lines, confirming our predictions and supporting the initial AFM interpretation. From the TEM analysis, additional information is obtained on the threading dislocations (TD) which bend to the surface. As observed in Fig. 4.14(e,f), most dislocations appear as running from pit to pit, hence suggesting that most of the TD terminate at the pit surfaces which creates large dislocation free areas. Many pits are also the origin of planar defects, such as multiple stacking faults and microtwins. This is probably due to the conformal growth on top of the {111} facets, which enhances Shockley partial dislocations formation, and thus the corresponding stacking faults. Examples of such extended defects can be seen in TEM cross section, as can be seen in Fig 4.14(e).

4.5 Dislocation engineering

In conclusion, our model predictions demonstrate that by suitably patterning the Si substrate with {111} pits, it is possible to introduce high stress concentrations in low misfit SiGe films, which operate as preferential sites for dislocation nucleation and threading dislocation trapping. This produces a regular array of misfit dislocations trapped along the pit lines, and provides large dislocation free areas, suitable for device integration. It is therefore possible to fabricate relatively large film areas (∼1 μm^2) free of detrimental dislocations, without using dielectric masks or non-connected substrates. Moreover, our approach can provide efficient dislocation engineering and can be exploited to conduct tailored experiments to directly assess optical and electrical properties induced by the dislocations. The fine level of agreement obtained between real and simulated dislocation microstructures proves the strength of the modelling methodology proposed here. We believe that our approach can be useful to investigate the full plastic relaxation process in different epitaxial structures, assessing the influence of the substrate patterning geometry on dislocation gettering, and to obtain at least qualitative insight into the relevant dislocation nucleation mechanisms.

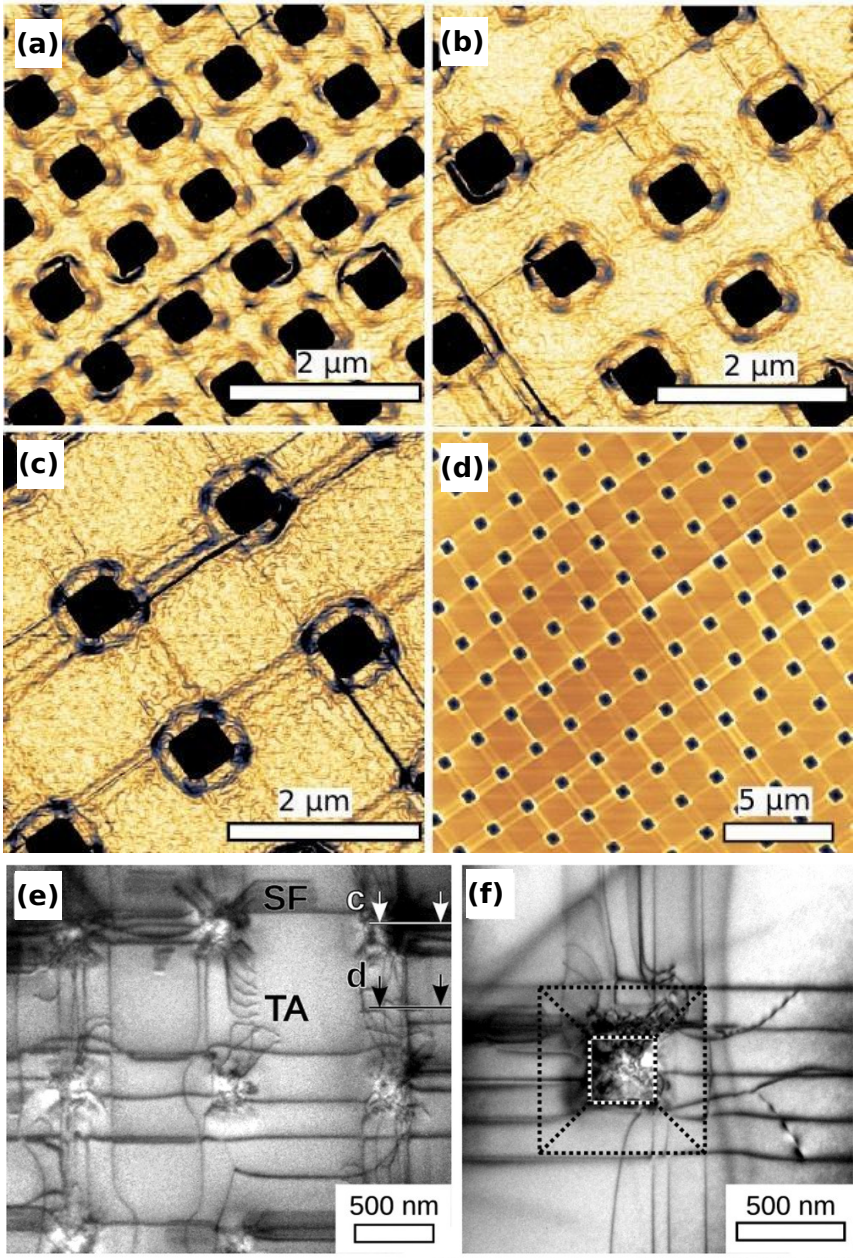

FIGURE 4.14: AFM inclination images showing the morphology of a 5 × 5 μm^2 areas of a Si template after deposition of a 250 nm thick $Si_{0.85}Ge_{0.15}$ layer. The pit pattern periodicity is 1 (a), 1.5 (b) and 2 μm (c). (d) 20 × 20 μm^2 area of the sample characterized by a 2 μm pit periodicity. The lines between the pits are the footprints of underlying dislocation bundles. (e) TEM plan view images of the 1 μm period sample. Dislocations parallel to the ⟨110⟩ directions run from pit to pit, leaving large areas dislocation-free. Examples of threading arms (TA) and of stacking faults (SF) are indicated. (b) Dislocation distribution in the vicinity of a single pit. The facets of the pit are highlighted in this plan-view image.

5

Plastic relaxation in nanoislands

Self-assembled nanoislands are three dimensional crystals with nanometric size that are in principle suitable for lots of applications within semiconductor technology. Due to their reduced size and their 0-dimensionality, nanoislands present new properties that cannot be achieved in higher dimensionality systems, that can be exploited, for example, in quantum-dot lasers , IR photo-detectors [172] and transistors [173]. The electronic and optical properties of nanoislands are strongly dependent on the morphology (volume, shape, composition). In the past years, a lot of effort has been devoted to govern the island growth process in order to tailor such properties. Moreover, crystal defects and in particular dislocations, have been shown to affect the opto-electronic response of nanoislands deteriorating the performances of potential applications. Hence, it is fundamental to determine the coherency limits in such nanostructures and establish how dislocations influence island growth and morphology. Among the different semiconductor heteoepitaxial system, Ge on Si(001) is considered a prototypical system to understand the Stranki-Krastanow growth and the strain relaxation mechanisms, which characterize also more complex systems, such as GaAs/Si(001) or other mismatched III-V or II-VI semiconductors. Shedding light on SiGe island plasticity, not only would allow to control island morphology and establish the coherency limits for growing such structures, but the modelling and the key mechanisms predicted for dislocation formation in the SiGe islands could probably be extended to other semiconductor systems, at least to diamond structure materials, allowing for coherent island growth that can be exploited as buffer layers for many applications.

In this Chapter, we first investigate plastic relaxation in SiGe islands grown on flat Si(001) substrates, addressing the self-ordering of misfit dislocations in such epitaxial nanoislands. The understanding of the organization of dislocations in an ordered pattern can be useful for dislocation engineering in other epitaxial structures. Moreover, a study on plastic relaxation in SiGe islands grown on pit-patterned Si(001) substrates is presented, aimed to establish the coherency limits of islands nucleated in pits and to develop a new strategy to delay the plastic relaxation onset in epitaxial islands by substrate nanopatterning.

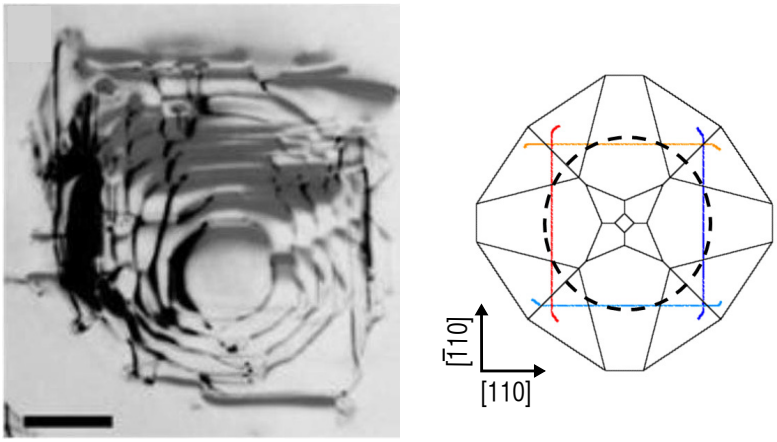

FIGURE 5.1: TEM image of a Ge island (dislocated dome) grown by UHV-CVD on Si(001) in situ in the TEM. This image has been obtained by superimposition of two dark field ($\boldsymbol{g}, 3\boldsymbol{g}$) weak bean images with $\boldsymbol{g} = \langle 220 \rangle$ and $\boldsymbol{g} = \langle \bar{2}20 \rangle$. [84] Right: Approximation of the dislocation line formed by the intersection of four 60°dislocation segments as a circular path.

5.1 Dislocations in SiGe nanoislands

The nucleation of misfit dislocations in heteroepitaxial 3D islands present some differences with respect to the case of continuous flat films. First, the shear stress (and consequently the resolved shear stress relevant for dislocation nucleation) at the base perimeter of Stranki-Krastanow (SK) SiGe islands, increases with island aspect ratio AR (height to square root of the base ratio) [80]. Thus, in "mature" islands (domes, barns), the basal borders are natural stress concentrations and are the expected dislocation sources. Second, because of the small island size, dislocations need to glide very short distances (10-100 nm) to deposit a misfit segment at the interface and reach their final configuration. The combination of reduced size of the islands (down to some tens nanometers in lateral size), and the significant variations in misfit strain (induced by the multifaceted free surface), increasing from top centre to the island edges [80, 174], in turn, generates the ideal site for homogeneous nucleation of dislocations [39]. Hence, whenever the island dimensions are sufficiently large to reach a critical elastic budget, dislocation nucleation should occur. In the $CoSi_2$/Si(111) system, it has been shown, by transmission electron microscopy (TEM) in situ investigations and dislocation dynamics simulations [125], that misfit dislocation segments effectively nucleate at the base borders of epitaxial $CoSi_2$ islands, and subsequently move by glide on the (111) plane towards the island base centre. In the case of Ge (or SiGe) on Si (001), no dislocation gliding is possible along the island base plane. Still an ordered pattern of misfit dislocation lines is observed, as shown by the TEM plan view image in Fig. 5.1. This pattern should be produced by the periodic incorporation of 60°dislocation segments at the island edges, as observed in Ref. [61, 78, 175]. The dislocation nucleation is accompanied by sudden lateral expansions of the island, at expense of the island thickness, and followed by a slow recovery of the original shape (and elastic budget), during accumulation of the deposited material at the top. This phenomenon

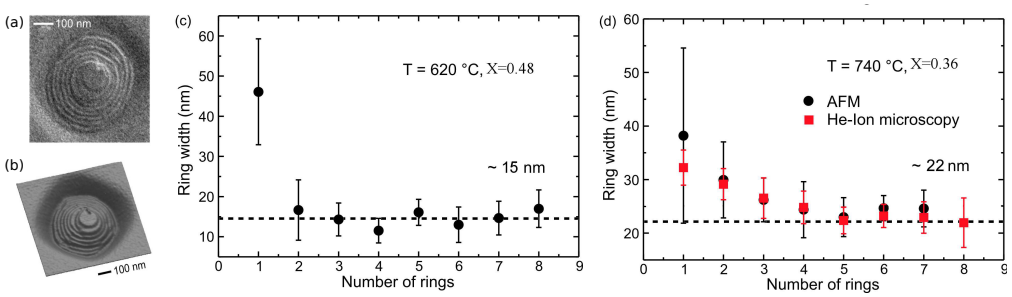

FIGURE 5.2: (a) He-ion image of the Si surface obtained after removal of a dislocated SiGe island grown at 740 °C showing a characteristic ring structure. (b) 3D view of an AFM image of a similar ring structure (the depth of the trench around the tree-ring is about 16 nm). (c), (d) Statistical analysis of the ring width as a function of number of rings obtained from AFM and He-ion microscopy images of several islands growth at 620 °C (c) and 740 °C (d). The average Ge content was estimated to be X=0.36 at T=740 °C and X=0.48 at T=620 °C, using AFM. [176]

was named *cyclic growth*[61] and it is expected at the usual growth temperatures ($T_g >$ 600°C) [175].

In the following, we explain the intriguing ordering of misfit dislocations, as obtained with no gliding rearrangements, by cyclic occurrence of the thermodynamic critical conditions for plastic events. Quantitative predictions by a simple analytical model, which includes the dependence on island shape and composition in the generation of misfit dislocations, matched very well experimental measurements.

5.2 Self-ordering of misfit dislocations

5.2.1 Dislocation spacing in nanoislands

Ordering of misfit dislocation segments in a regular pattern at the base of SiGe epitaxial islands on Si(001) has been also indicated by the regular spacing of the footprint carved in the Si substrate by the plastic events, observed by atomic force microscopy (AFM) [83]. A very interesting result is found by analyzing these structures escaveted in the substrate during islands growth. In Fig. 5.2, we show the tree-ring structures imaged by AFM (a) and by helium-ion microscopy (HeIM) (b), obtained after molecular bean epitaxy (MBE) deposition of Ge/Si(001) and subsequent selective etching experiments that selectively remove $Si_{1-X}Ge_X$ over Si. Details on the growth and etching experiments leading to the results plotted in Fig. 5.2 can be found in Ref. [176]. As described in Section 2.5.2, the surface morphology, imaged after the selective etching, reveals the footprints left on the surface by large dislocated islands, consisting in a central Si plateau surrounded by a staircase of several nearly concentric rings. These are produced during the island cylic growth. In fact, as the deposition proceeds, islands accumulate material on top, increasing their AR and meanwhile carve a progressively deeper trench in the Si substrate at the perimeter of the island base. After selective SiGe etching, this stage corresponds to a short steep profile in the AFM scan of the Si substrate. As the critical

conditions for one dislocation nucleation are met, sudden lateral expansion of the island has been observed [78], providing a full coverage of the trench bottom line. This stage corresponds to a small plateau in the etched samples. Periodic repetition of these two stages gives rise to a clear stepped profile in the Si substrate, which appears in form of a tree-ring structures of concentric steps in the surface morphology [83], as shown in Fig. 5.2. From the microscopy images, the distances between subsequent rings (ring width) has been measured, starting from the central plateau and moving towards the periphery of the islands along two orthogonal directions [176]. Fig. 5.2(c) and (d) display the average ring width measured over many islands for two different growth temperatures. The AFM results are shown in black circles, while the values obtained by HeIM are shown in red squares. The measured ring width shows a slight decrease from the island centre to the island borders, in the range of 20 to 10 nm for the sample grown at 620°C and between ∼30 and ∼20 nm for the sample grown at 740°C, converging to an almost constant value, 15 and 22 nm, respectively, for the two samples. The average island composition determined using AFM is X ∼0.36 and X ∼0.48 at 740°C and 620°C, respectively.

5.2.2 Multiple dislocation modelling

In order to interpret the experimental findings, we propose an analytical modelling of multiply dislocated islands, similar to the one commonly used in the calculation of thermodynamic critical thickness for flat films [26], and recently adopted in the calculation of the critical dimension for the first dislocation nucleation in SiGe islands on Si(001)[82], in InGaAs islands on GaAs(001)[81] and nanowires[177]. This simple approach fully captures the essential energetics of the system, just assuming circular paths (representing the misfit dislocation lines forming concentric polygons at the interface), which are nucleated right at the perimeter of the growing island. Obviously, the real dislocation microstructure is more complex: 60°misfit segments along the [110] and the [$\bar{1}$10] direction nucleated at the different island edges and their threading arms produce the concentric dislocation lines, as shown in Fig. 5.1. However, our geometrical simplification is able to capture the average dislocation length and density, which is the essential feature in an energetic analysis. In Fig. 5.1, we show the expected dislocation lines forming the pattern (color full lines) and the circular path (dashed line) used to approximate such a dislocation geometry.
At the typical deposition temperatures of Ge on Si(001), islands with a different Ge concentration are found because of the alloying taking place during the epitaxial growth [65, 73]. This issue will be addressed by considering $Si_{1-X}Ge_X$ islands with a different Ge concentration compatible with the typical alloying observed (X=0.3-0.6) in the relevant temperature range for deposition of Ge on Si(001) (T_g=550-750 °C).

Analytical model for misfit dislocation spacing in nanoislands

The model we propose simply consists in the calculation of the critical condition for introducing a new misfit dislocation line, in a $Si_{1-X}Ge_X$ island. This condition is obtained when the energy cost for creating a new n-th dislocation $E_{cost}^{(n)}$ matches the energy gain

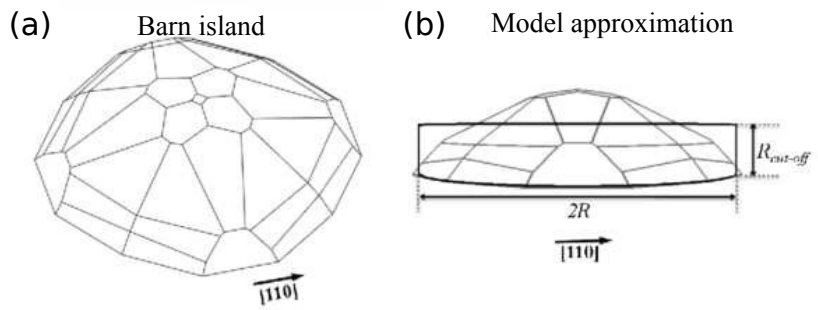

FIGURE 5.3: (a) Schematic representation of a barn island. The barn shape is built using experimentally reported facets [58, 59] ({15 3 23}, {1 1 3}, {1 0 5} for domes; {1 1 1}, {4 20 23}, {3 15 23}, {1 1 3} {1 0 5}, for barns) arranged to yield the typical experimental average aspect ratio, resulting in close similarities with the observed shapes. In the analytical model used here, islands are approximated by a cylinder with the same base area and volume of a realistically shaped island (a), as shown in (b).

$E_{cost}^{(n)}$, due to the strain relaxation induced by the dislocation itself:

$$E_{cost}^{(n)} + E_{gain}^{(n)} = 0 \; . \tag{5.1}$$

The estimation of the critical island dimension for the nucleation of the n-th dislocation is then obtained by calculating the two energy contributions as a function of the island volume V and finding the value of V for which Eq. 5.1 is satisfied. In the following we illustrate how $E_{cost}^{(n)}$ and $E_{cost}^{(n)}$ have been evaluated.
Here, we considered a $Si_{1-X}Ge_X$ island with an aspect ratio AR=0.3 and barn shape, as shown in Fig. 5.3, but the model can be more generally applied to any island shape by suitably changing the geometrical parameters.
An analytical expression for the misfit strain energy stored in the island and in the substrate can be formulated in analogy to the case of a continuous film [81, 82]:

$$W_n = \frac{\mu}{1-\nu} F(AR, X)(\varepsilon_{xx}{}^2 + 2\nu\varepsilon_{xx}\varepsilon_{yy} + \varepsilon_{yy}{}^2)V \; , \tag{5.2}$$

where μ is the shear modulus, ν is the Poisson ratio, ε_{xx} and ε_{yy} are the in-plane strain tensor components, V is the island volume, and $F(AR, X)$ is the reduction factor of the elastic energy stored in the three-dimensional island and substrate, as compared to the flat film case. In particular, $F(AR, X)$ is given by the ratio between the elastic energy stored in island and substrate divided by the island volume and the elastic energy density in a biaxially strained two-dimensional layer. $F(AR, X)$ depends on the island shape and decreases significantly when AR increases. Here $F(AR, X)$ was numerically evaluated for a barn shaped island with an aspect ratio AR=0.3 (Fig. 5.3) and for different compositions by FEM. Assuming the elastic constants of a Si-Ge alloy can be linearly interpolated between the bulk values of pure Ge and Si, we found that $F(AR, X)$ depends on the Ge content X by $F(AR, X) = a(AR) + b(AR)X$. Notice that in this analytical model islands are approximated by a cylinder with equal base area and volume[82]. The realistic geometry shown in Fig. 5.3 was used to define the relaxation function $F(AR, X)$ and the

geometrical ratio V/r^3, where V and r are the island volume and base radius, respectively. The values of $a = 0.32$ and $b = 0.030$ were evaluated for islands with barn shape as drawn in Fig. 5.3.

The decrease in energy ($E^{(n)}_{gain}$) due to the misfit strain reduction provided by a new n-th dislocation is given by

$$E^{(n)}_{gain} = W_n - W_{n-1} \ , \tag{5.3}$$

where W_n is the elastic energy stored in an island when n dislocations are present. W_n can be calculated by evaluating the misfit strain reduction due to the n dislocations. Here, we considered the x and y axis parallel to the [110] and the [$\bar{1}$10] directions, respectively. For a coherent island, $W_n = W_0$ is obtained by substituting $\varepsilon_{xx} = \varepsilon_{yy} = f$ in Eq. 5.2, being f the lattice misfit strain between the island and the substrate. For a dislocated island, W_n is found by substituting in Eq. 5.2 the in-plane strain components $\varepsilon_{xx} = \varepsilon_{yy} = f - \varepsilon_{disl}(n)$, corresponding to the lattice misfit f, as reduced by the presence of the n circular dislocation lines by $\varepsilon_{disl}(n)$. Due to the decomposition of the circular shape into [110] and [$\bar{1}$10] misfit segments, each virtual curved portion can be interpreted as relieving $b_{eff}/2$ on the average, along the two orthogonal strain components, multiplied by an effective linear density of dislocations $\left(\sum_{i=1}^{n} \frac{\lambda_i}{\pi R^2}\right)$, where $\lambda_i = 2\pi R_i$ is the length of each dislocation nucleated at a different island base radius R_i. This simply means that, on the average, half dislocation length is parallel to the [110] direction and reduces the ε_{yy} strain tensor component, while the remaining half dislocation length is parallel to the [$\bar{1}$10] direction and relaxes the ε_{xx} component. R is the actual island base radius, $b_{eff} = b/2$ is the effective Burgers vector for a 60°misfit dislocation with Burgers vector $b = a_{SiGe}\sqrt{2}/2$ and λ_i is the length of each dislocation. Thus, the island misfit in presence of n circular dislocations is reduced by

$$\varepsilon_{disl}(n) = \frac{b_{eff}}{2} \sum_{i=1}^{2} \frac{\lambda_i}{\pi R^2} \ . \tag{5.4}$$

A second contribution to the total energy is the cost related to the lattice distortion provided by the dislocation itself. $E^{(n)}_{self}$ can be analytically calculated as for the case of a flat film, by considering again that each segment of the circular path is decomposed into two straight components, along the x and the y directions. In this case:

$$E^{(n)}_{self} = \lambda_i \frac{\mu b^2}{4\pi} \left(\cos^2\beta + \frac{\sin^2\beta}{1-\nu} \right) \log \frac{\alpha R_{cut-off}}{b} \tag{5.5}$$

where β is the constant angle between each dislocation component and the Burgers vector $\boldsymbol{b}$, α is the parameter taking into account the atomistic core energy (usually set to 2.7 for Si and Ge materials [26]). $R_{cut-off}$ is the cut-off radius of the dislocation strain field, i.e. the average distance of the dislocation line from the free surface, taken as the height of a cylinder equal in volume and in base area to the island [82], as shown in Fig. 5.3(b), so that $R_{cut-off} = V/(\pi R^2)$.

Except for the first dislocation, an additional increase in energy due to dislocation formation is also given by the interaction energy between the n-th dislocation and the other $(n-1)$ dislocations already present in the island. Here it is taken as the sum of the well

established pair-interaction energies between straight dislocation segments located near a free surface [178]:

$$E_{int}^{(n)} = \sum_{j=1}^{n-1} \frac{(\lambda_n + \lambda_j)}{2} E_I(d_{nj}) \tag{5.6}$$

where

$$\begin{aligned} E_I(d_{ij}) &= \frac{\mu b^2 \sin^2\beta \sin^2\phi}{4\pi(nu)} \left(\ln 4a^2 + 1 - \frac{4a^2(12a^2+1)}{(4a^2+1)^2} \right) \\ &+ \frac{\mu b^2 \sin^2\beta \sin^2\phi}{4\pi(1-\nu)} \left(\ln 4a^2 + 1 + \frac{4a^2(4a^2+3)}{(4a^2+1)^2} \right) \\ &+ \frac{\mu b^2 \cos^2\beta}{4\pi(1-\nu)} \left(\ln 4a^2 + 1 \right) \end{aligned} \tag{5.7}$$

Here d_{ij} is the separation distance between dislocations, $a = R_{cut-off}/d_{ij}$ and ϕ is the angle between the glide plane of either the two components of the misfit segment and the vertical [001] direction. Therefore, by summing the last two contributions into one "energy cost" term, one obtains:

$$E_{cost}^{(n)} = E_{self}^{(n)} + E_{cost}^{(n)} \, . \tag{5.8}$$

It should be noted that the change in the average Ge composition X of the island affects both the misfit f and the elastic constants entering the two terms of Eq. 5.1. Since we assumed that all the dislocation circles nucleate exactly at the island edge, the ring spacing (and the dislocation spacing) as a function of the number of dislocations in the island is obtained directly by subtracting subsequent critical base radii R, as obtained by solving the critical condition in Eq. 5.2. The dislocation spacing in a $Si_{1-X}Ge_X$ island is then evaluated by the difference in the radii of the circular paths adopted to describe the dislocations.

Equilibrium position of misfit dislocations in nanoislands

In Fig. 5.4 we report how the critical condition (Eq. 5.1) is periodically satisfied by increasing the dislocation number and island base radius for a barn with X=0.36 (black arrows), corresponding to the average value experimentally determined for samples grown at T_g=740 °C. From the left to the right in Fig. 5.4, the solid blue curves give the E_{gain} terms calculated increasing the number of dislocations from 1 to 5 as a function of the island radius. Similarly, the dashed red curves give the E_{cost} terms obtained by varying the dislocation number n from 2 to 5 (from left to right), while the dotted green line represents the E_{self} term. This curve increases monotonically because E_{self}, (see Eq. 5.5), depends just on the last length of the dislocations and on the cut-off radius Rcut-off, which in our model are both directly proportional to the island radius R. The first dislocation is nucleated when E_{self}(dotted line) is equal to E_{gain} (first solid line left), while all the others are nucleated when E_{cost} (dashed lines), including both the self energy and the repulsive term, crosses E_{gain} (solid lines). We note that the radial spacing between dislocations rapidly decreases to a nearly constant value, and that the repulsive term

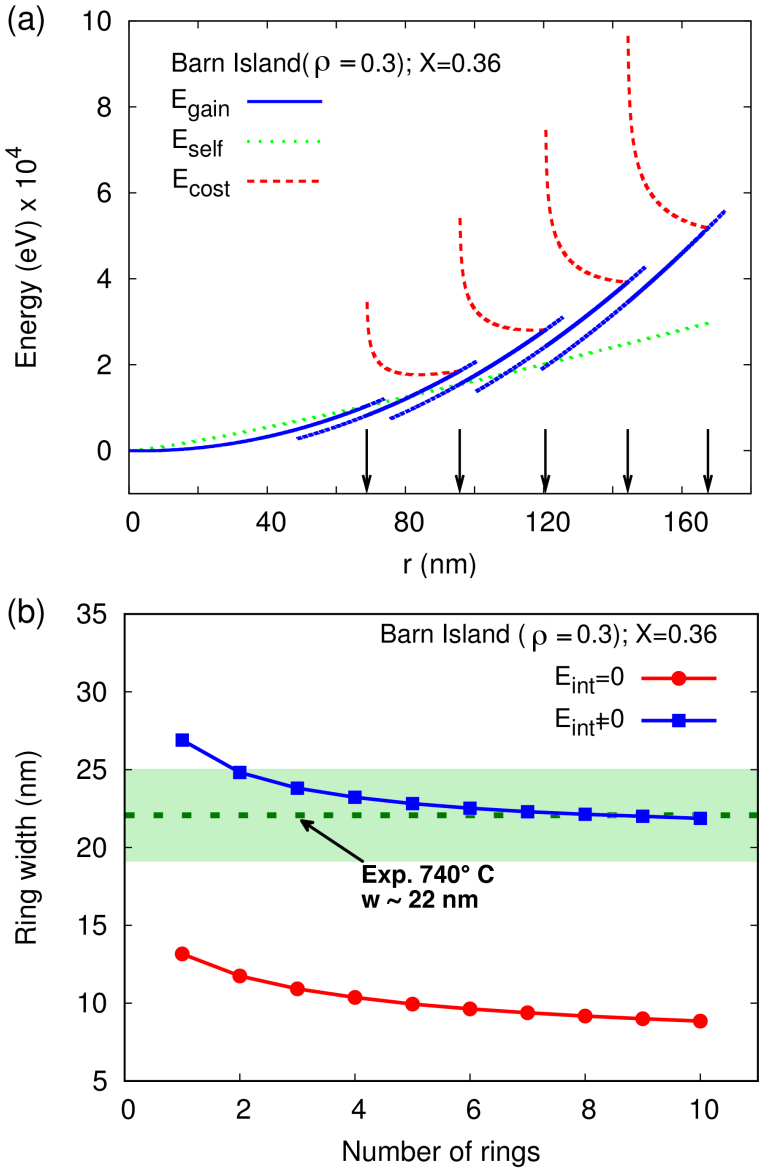

FIGURE 5.4: (a) Critical radii (arrows) for dislocation nucleation. The first critical radius is determined by the intersection of E_{gain} (solid, blue curve) and E_{self} (dotted, green curve), which is the only energy cost term. Subsequent critical radii are also influenced by dislocation-dislocation interaction (E_{int}). Plastic relaxation therefore occurs at the intersection between E_{gain} and the total energy cost E_{cost} (dashed, red curve), i.e. the sum of E_{self} and E_{int}. (b) Distance between dislocations (ring width) versus the number of rings, with (full boxes, blue) and without (full circles, red) including the E_{int} term. The ring width saturation value at T=740 °C is reported using a dashed line within a shaded rectangle representing error bars.

contributes significantly to the spacing. These issues are better seen in Fig. 5.4(b) and Fig. 5.5, where we report the ring width between two plastic events vs. the increasing number of rings for the same system. In Fig. 5.4(b), the ring width was calculated with (solid line with boxes) and without (dashed line with circles) the interaction term. We see that the solid curve correctly reproduces the experimental trend observed at 740 °C, as reported in Fig. 5.2(d), and converges to the ring width value of 22 nm, which is the experimental indication. The dashed curve obtained neglecting the repulsive term is shifted by a nearly constant value far below this experimental data, outside the relative error bar (grey band in Fig. 5.5(b)). The results in Fig. 5.5 show that the ring width initially decreases with the dislocation number, but after the nucleation of the very first dislocations the spacing between two subsequent circles becomes almost constant. The shape and the size of the island clearly affect the early plastic events, dislocations interact with free surfaces and with each other in small volumes, so the spacing between circles is larger than the value provided by the theory for the continuous film case[26]. Increasing the island radius the size effect is lost and the plastic relaxation events occur periodically. With or without the dislocation interaction, the calculation gives qualitatively the same behavior, but quantitatively different results, as highlighted in Fig. 5.4(b). Hence the dislocation interaction cannot be neglected in the thermodynamic balance, if we want an accurate prediction of the critical island radii and dislocation spacing. As one should expect, increasing the Ge content inside the island the elastic energy stored in the system is also increased and the dislocation spacing becomes smaller with the increasing misfit. In fact, by tuning the island Ge content x from 0.3 to 0.5, as reported in Fig. 5.5, a downward shift and flattening of the ring width curve is obtained, in agreement with the experimental trend observed by decreasing the growth temperature, outlined in Fig 5.2. In particular, we observe that at any Ge concentration the ring width quickly converges to a nearly constant value, which is lower for higher island Ge content. Together with the theoretical calculations at different island Ge concentrations we plotted in Fig. 5.5 the saturation ring width values (dashed lines) for the two growth temperature examined in Ref. [176] and shown in Fig. 5.2(c,d). Comparing the experimental ring width values with the theoretical curves, we see a good agreement between the ring width measured at 740 °C and 620 °C and the curve obtained for X=0.36 and X=0.48, respectively. Recently, the in-plane distance between two interfacial 60°dislocations is epitaxial $Si_{1-X}Ge_X$ islands has been measured in Ref. [179] by a *in situ* non-destructive method, based on x-ray diffuse scattering close to forbidden reflections. In this work, a decrease of the average in-plane distance between interfacial dislocations with increasing Ge volume deposited is observed, in good agreement with the values predicted by our model.

In conclusion, we have shown that the regular spacing of the misfit dislocation segments arranged in concentric polygons at the base of heteroepitaxial GeSi islands on Si(001) is a feature determined by periodically matching the thermodynamic critical conditions for plastic events onset. Due to the absence of glide rearrangement in the island basal plane it was an interesting issue to understand if and how the misfit dislocation repulsion acts in providing such regular spacing, especially because of the high dislocation density obtained in the limited island volume. By a quantitative agreement between experimental measurement of plastic event spacing and predictions of a very simple, fully analytical

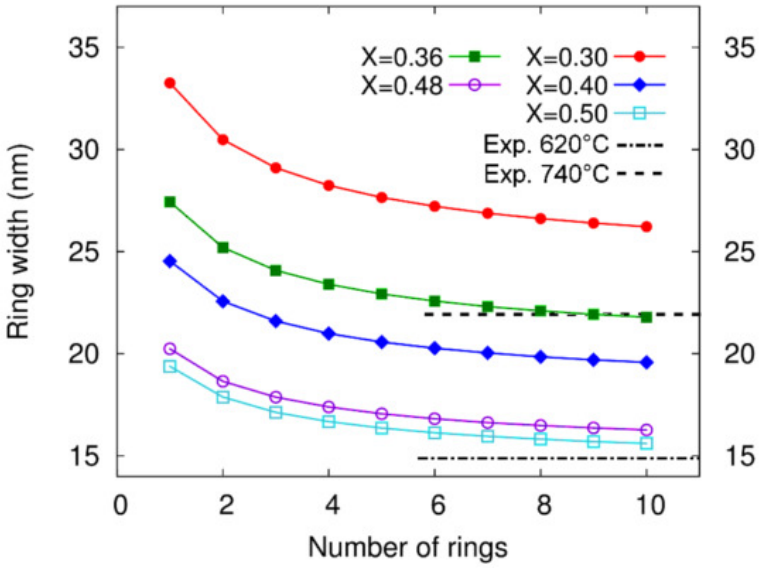

FIGURE 5.5: Distance between dislocations (ring width) versus the number of rings at different Ge content for a barn island (AR=0.3). Experimental results taken at both 620° C and 740° C (corresponding to an average island Ge content of x=0.48 and x=0.36, respectively) are well reproduced by the model, considering uncertainties in both concentration estimates and ring widths. [176]

model we have shown that the dislocation repulsion is important in determining the ring spacing, but the repulsion is not essential to generate the periodic pattern.

5.3 Nanoislands on pit patterned substrates

Deposition of Ge on Si(001) substrates leads to the formation of SK islands, as we have seen in Section 2.5. At low Ge coverage islands are small and coherent while proceeding with deposition, larger dislocated islands appear [61, 75]. Typically, islands nucleate at random sites on the exposed surface and a bimodal distribution of island sizes, due to the coexistence of shallow pyramids and steeper domes, is observed [180]. In view of exploiting islands for any application (e.g. in electronic devices as metal oxide field effect transistors MOSFETs [181]), two main issues must be tackled. First, islands should be homogeneous in size, shape and chemical composition, and must be laterally ordered. Second, plastic relaxation must be avoided. Growth on suitably-patterned Si(001) substrates allows to solve the first problem. As shown in Ref. [95], Ge deposition on substrates where an ordered array of pits is created by nano-lithography leads to extremely ordered islands positioning within the pits. Moreover, the island distribution is strikingly uniform in shape and size and islands in pits evolve in a more synchronized fashion [182]. If controlling nucleation inspired the idea of patterning substrates, a second advantage came out as an unexpected bonus. In Ref. [93] experiments showed that coherent islands in pits were still present for typical volumes where, instead, plastic relaxation was observed in islands grown on

planar Si(001) substrate. Preliminary calculations suggested that this observation could be linked to the higher degree of elastic relaxation due to the partially filled pit with the island ontop [183]. A direct proof of such extra-relaxation was recently given exploiting X-rays measurements [97]. However, no direct attempt of predicting the critical volume V_c for misfit-dislocation insertion in islands was provided.

In this work, we theoretically evaluate the critical volume for dislocation formation in SiGe islands nucleated in pits and we demonstrate that there is a delay in the plastic relaxation onset in epitaxial islands grown on nanopatterned substrates. Our predictions clarify the causes for the plastic relation delay in islands nucleated in pits and are successfully compared with a set of measurements of V_c in islands grown on a pit patterned Si(001) substrate after the deposition of Ge by MBE.

5.4 Plastic relaxation in nanoislands on pit patterned substrates

The plastic relaxation onset in epitaxial islands grown on flat Si(001) substrate have been investigated by several authors, considering simplified or realistic island shape for different semiconductor materials[75, 80–82]. However, we did not found any previous attempt to predict the critical volumes for dislocation formation in islands grown on pit-patterned substrates. This is of fundamental importance in order to obtain coherent islands at regularly spaced positions, that can be used as buffer layers for devices. Here we considered dislocations in the primary $< 110 >\{111\}$ slip systems, following the experimental evidences that this kind of defects (leading to the deposition of 60°misfit segments at the interface) are the most commonly observed, at least in the high T_g range. In this work, we investigate the critical condition for the introduction of the first dislocation in epitaxial islands nucleated in pits. To this aim, we adopted a more accurate method with respect to the simple analytical model used in Section 5.2.2 to explain the ordering of multiple dislocations in the Ge/Si(001) system. In fact, we believe that dislocation formation in islands nucleated in pits depends strongly on the heterogeneous epitaxial stress field produces by both the material filling the pit and the islands on top of it. For this reason, the onset of plastic relaxation, defined by Eq. 5.2, was found by calculating the elastic energy in coherent and dislocated islands by FEM, which is known to give accurate results for the elastic energy produced by complex 3D structures, as nanoislands, and by the dislocations therein. In the following, we first describe a set of experiments relevant for validating the model and for the discussion of the results obtained. Then we present our theoretical predictions for dislocation formation in islands grown on pit patterned substrates and finally we compared them with the experimental results performed at the University of Linz and reported in Ref. [184].

5.4.1 Critical volume measurement in nanoislands

Depositing Ge on Si(001) substrates patterned with pits, defined as described in [92, 184], on the pit-patterned fields, islands eventually nucleate in the middle of the pits (see e.g. Fig. 5.6(b)). The morphological evolution of SiGe islands grown on pit-patterned Si(001)

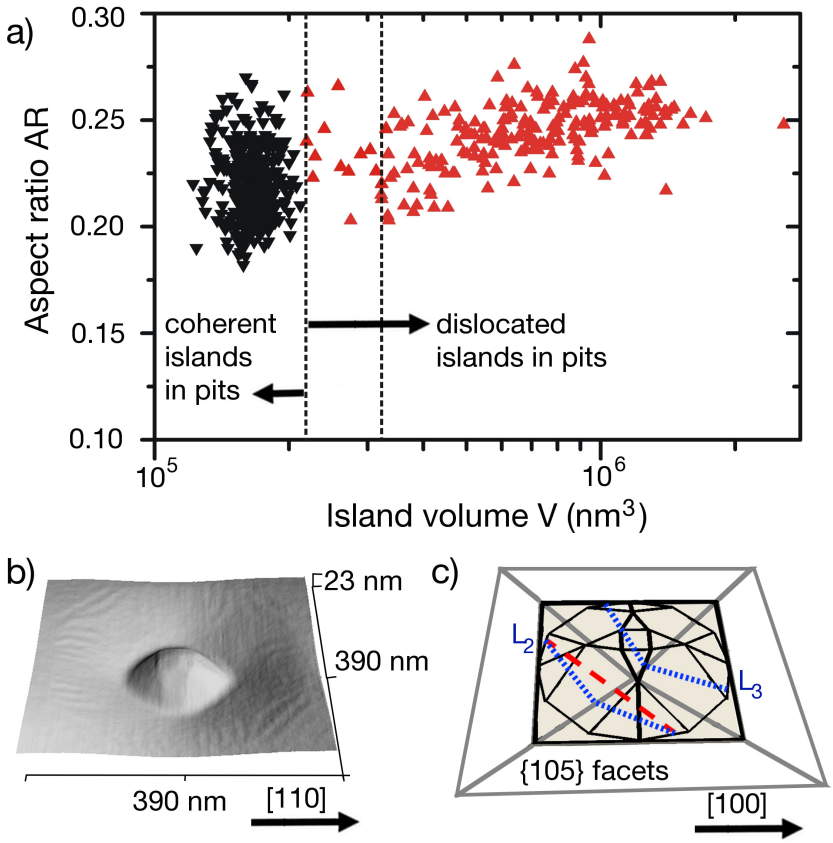

FIGURE 5.6: (a) AR vs. V plot of islands grown in pits at T_{Ge} = 690°C. Coherent (dislocated) islands are indicated as black downward triangles (red upward triangles). A volumetric gap between the two types where only few islands are found marks V_c. (b) 3D AFM image of a dome island nucleated in a pit (growth temperature: T_{Ge} = 650°C). (c) Geometry used to model a dome grown in a pit. Dashed and dotted lines indicate dislocation segments at the (001) dome/DP interface and at the DP/substrate interface, respectively. [184]

substrates and nucleated in pits is similar to the one observed on the same unpatterned flat substrates [94]. Islands in pits evolve augmenting their AR with their increasing volume in order to enhance the elastic strain relaxation. This trend changes when plastic relaxation occurs: islands continue to grow with no significant change in their AR and reduce their elastic energy by progressively nucleating new dislocations. In Fig. 5.6(a), it is shown a typical plot of the island AR (here calculated as the height to square root of the base ratio) versus the island volume (V) for islands grown on a Si(001) pit patterned substrate at 690°C and nucleated in the pits [184]. Two groups of islands can be identified in this plot. Coherent ones at low V (here reported by black downward triangles) and a "tail" of red upward triangles which represents the dislocated islands that have similar AR but significantly larger V. There exists a volumetric gap between these two groups of islands where only few islands are statistically found. Since islands quickly increase their volume as soon as a dislocation nucleate into the island, and further cyclic growth occurs for additional dislocations[61], the lower V of the volumetric gap can be taken as V_c. A representative AFM image of an island grown in the middle of a shallow pit is shown in Fig. 5.6(b). Such an island has an AR in the range $\sim$ 0.22-0.26 and exposes {105} and {113} facets typical of dome islands. The pit geometry can be described as a downward pyramid with {105} sidewalls, as can be seen in Fig. 5.6(b) or in Ref. [93]. In Fig. 5.6(c) we reproduced the experimental pit and island shape by using geometrical objects with well defined facets closely representing the observed morphology.

5.4.2 Modelling plastic relaxation in islands on pits

In order to model the onset of plastic relaxation for the typical dome-shaped islands grown in the pits, we considered a {105} pit (closely representing the experimental shape, see Fig. 5.6(b) half filled with a SiGe alloy, i.e. a downward {105} pyramid (DP) with a (001) base, hosting a dome island on top. This geometry is sketched in Fig. 5.6(c), and directly compared with the experimental AFM micrograph of a typical dome presented in Fig. 5.6(b).

We considered dislocations in the primary $\{111\}\langle 110\rangle$ slip systems, the most favorable one in the Si/Ge system [3], and the most commonly observed, when SiGe islands are grown at sufficiently high temperatures [78]. In particular, we selected one of such slip systems, characterized by $\{\bar{1}1\bar{1}\}$ glide plane and $\boldsymbol{b} = a_{SiGe}[011]\sqrt{2}/2$ Burgers vector, with $a_{SiGe} = a_{Ge}x_D + a_{Si}(1 - x_D)$, being a_{Ge} and a_{Si} the Ge and Si lattice parameters and x_D the dome island Ge composition. When such a defect nucleates in SiGe islands grown on flat Si(001) substrates, a 60° misfit segment is deposited at the (001) interface, along the [110] or the $[\bar{1}10]$ direction. Its equilibrium position lies between the center and the edge of the island [75, 185], as indicated by the dashed red line in Fig. 5.6(c) (referred as line L_1 in the following). Actually, it would be the expected position also when the DP composition is very rich in Si. When the island and the DP have the same Ge content, no real interface exists between these two domains. Thus, a misfit dislocation with $\{111\}\langle 110\rangle$ slip system is expected to eventually glide towards the DP/Si interface, depositing two joint misfit segments (threading arms are expected to be short for the present geometry, and will be neglected) at the intersection between the glide plane and the {105} DP facets.

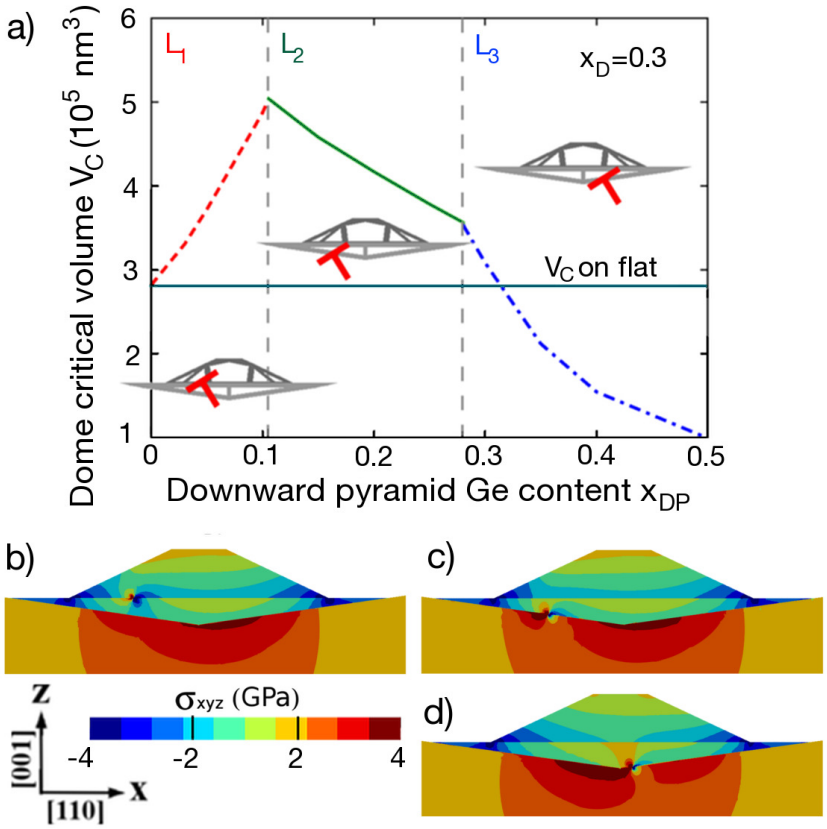

FIGURE 5.7: (a) Critical volumes V_c for plasticity onset in $Si_{0.7}Ge_{0.3}$ domes on pit-patterned Si(001) substrates as a function of the DP Ge content x_{DP}. For x_{DP}=0.2, we show the hydrostatic stress map in the xz-plane, perpendicular to the [110] direction, with the dislocation at the (001) dome/DP interface (b), where only the island is relaxed, and at the DP/Si interface, in its minimum energy position (c) and on the right handed pit side (d), where the dislocation relaxes mainly the DP. [184]

Selective etching experiments performed on SiGe islands grown at T=720°C, on analogous pit-patterned substrates revealed a DP Ge content ($\sim 10\%$) sensibly lower than the typical ones for the islands presented in this work (30-50%) [186]. Similar results confirming a lower DP Ge content (approximately 10%) with respect to the island one were presented in Ref. [184], where the experiments reported in the Section 5.4.1 are described in detail. Also the DP appears to be rather sharply separated from the dome shaped island on top.

To model plasticity in nanoislands, we followed the approach described in Section 3.4.2, where the combined effect of elastic and plastic relaxation is tackled using elasticity theory suitably solved by Finite Element Methods. In particular, the critical volume for plastic relaxation was evaluated as the minimum volume at which the energy of the system with a single dislocation was equal to the coherent one, for a suitable position of the dislocation segment as chosen among a grid of points built at both of the interfaces [82]. We notice that this condition is equivalent to the one expressed in Eq. 5.2, i.e. the energy cost required to insert the first dislocation $E^{(1)}_{cost}$ is counterbalanced by the energy gain in terms of strain relaxation $E^{(1)}_{gain}$:

$$E^{(1)}_{cost} + E^{(1)}_{gain} = 0 \Longleftrightarrow E^{(1)}_{disl} = E_{coh} + E^{(1)}_{cost} + E^{(1)}_{gain} = E_{coh} \ , \tag{5.9}$$

where E_{coh} and $E^{(1)}_{disl}$ are the total elastic energy of an epitaxial island before and after the formation of one dislocation. In particular, assuming that the dislocation can nucleate at the surface and move in the selected glide plane to reached the most favorable position (one of the two interfaces), the dislocation line configurations we considered, are found at the intersection between the dislocation glide plane and the two interfaces, as shown in Fig. 5.6(c). The elastic energy of the dislocated island has been calculated in these configurations, moving the dislocation line at both the dome/DP and the DP/substrate interfaces.

5.4.3 Pit composition dependent plastic relaxation

Let us now show how x_{DP} affects the favored dislocation position and, in turn, the critical volume for plastic relaxation onset. The critical volumes obtained for a Ge content x_D=0.3 in the dome are shown in Fig. 5.7(a) where both V_c and the optimal dislocation position are reported. For x_{DP}=0 we obviously find $V_c \simeq V_0$, the critical volume for a dome on flat Si(001), the dislocation position being analogous. By slightly augmenting the Ge content in the DP, V_c becomes increasingly larger than V_0. This is because the dislocation still remains at the dome (001) interface, but the island is less strained than on flat Si as due to the extra-relaxation effect provided by DP, as reported in Ref. [93] and further clarified by the calculations reported in Fig. 5.8. By increasing the Ge content above $x_{DP} \sim 0.11$, the dislocation position changes in order to relax also the DP. While it remains true that $V_c > V_0$, plasticity delay with respect to the flat case is reduced, since the total stressor volume is augmented. Upon increasing x_{DP} (beyond ~ 0.28), a third change in the optimal dislocation position is seen. The main stressor is now the DP, so that the dislocation position is the one maximizing the relaxation inside the DP. This is better understood by looking at Fig. 5.7(b-d), where the hydrostatic stress is reported for the case x_{DP}=0.2. By looking at the topmost island region, it is clear that the island strongly benefits by

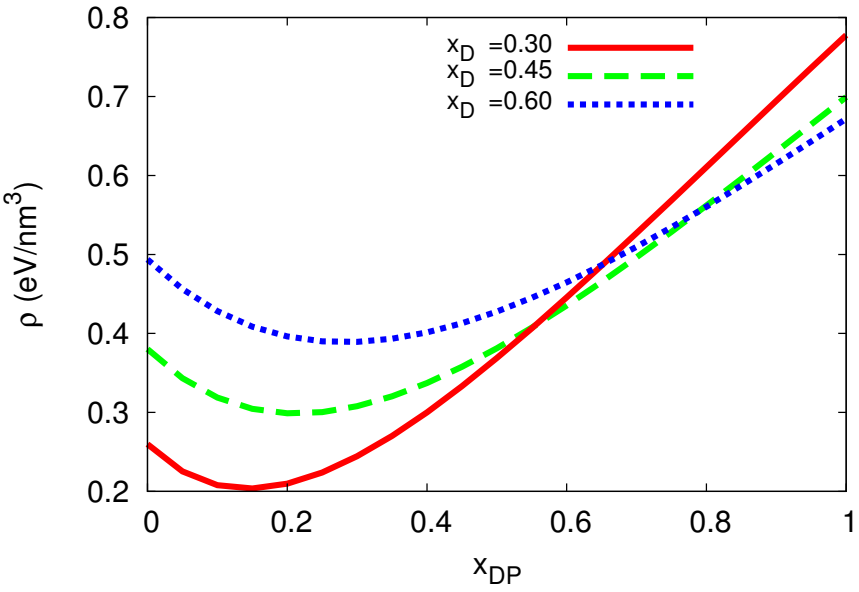

FIGURE 5.8: Elastic energy density in $Si_{1-x_D}Ge_{x_D}$ islands on pit-patterned Si(001) substrates as a function of the DP Ge content x_{DP}. The curves are calculated by considering dome islands with an avarage Ge content values x_D of 0.3, 0.4 and 0.5 respectively.

the dislocation presence when the latter is positioned as in Fig. 5.7(b) (equivalent to the dashed red line in Fig. 5.6(c), L_1). However, this requires further compressing the pit. At the other extreme, in the configuration of Fig. 5.7(d) (dislocation line L_3 in Fig. 5.6(c)), the DP relaxation is enhanced, at the expense of the island one. The best compromise for the analyzed Ge content is given by the configuration of Fig. 5.7(c) (dislocation line L_2 in Fig. 5.6(c)).

We have demonstrated that the interaction between the dislocation and the coherent stress field of the system is important in order to explain the equilibrium position for the dislocation in the system and the delay of plastic relaxation in islands grown on pit patterned substrates. In the following, we show how x_{DP} affects the elastic relaxation of the dome island and, as a consequence, the V_c values obtained. In Fig. 5.8, it is plotted the elastic energy density per unit of Ge volume, as a function of the x_{DP}. The elastic energy density per unit of Ge volume ρ_{Ge}, which is the total elastic energy of the system divided by the total Ge volume, is given by:

$$\rho_{Ge} = \frac{E_D + E_{DP} + \Delta E_{sub}}{V_{Ge}} = \frac{\int_V dE}{V_{Ge}} \tag{5.10}$$

Here E_D and E_{DP} are the elastic energy stored in the island and in the pit, ΔE_{sub} is the elastic energy introduced in the substrate due to the presence of both island and pit, V_{Ge} is total germanium volume and V is the total volume (dome, DP and substrate). As we can see from the curve in Fig. 5.8, starting from x_{DP}=0 (DP filled with pure Si), the elastic energy density ρ_{Ge} initially decreases with the increasing Ge content inside the {105} pit. The curve has a minimum when the SiGe alloy in the pit has a Ge content equal to 14%. Then the energy density increases, reaching the same value of ρ_{Ge} obtained for an island

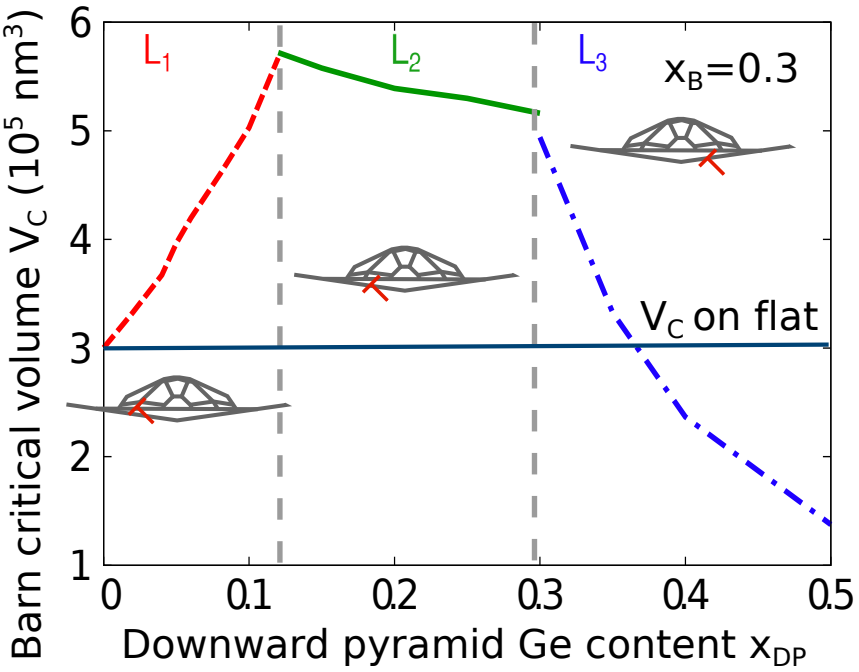

FIGURE 5.9: Critical volumes V_c for plasticity onset in barn-shaped islands (barn Ge content x_B=0.3) on pit-patterned Si(001) substrates as a function of the DP Ge content x_{DP}.

grown on a flat substrate, when the pit Ge content is $\sim 31\%$. Thus, whenever the pit Ge content is lower than the island one, the elastic energy density is reduced with respect to the flat case. This can be explained by the fact that, even if we augment the stressor volume in the system, the presence of a small Ge volume distributed in the DP allows for a large strain relaxation of the Ge rich island on top of the DP. The same trend is obtained when islands with a different avagare Ge content x_D are considered. The total elastic energy of islands on pits ρ_{Ge} initially decreases with the increasing DP Ge content. and a minimum is found approximately when $x_{DP} \sim x_D/2$. Notice that the minimum in the elastic energy density curve ($x_{DP} \sim 14\%$) in Fig. 5.8 is closed to the maximum in the V_c curve ($x_{DP} \sim 11\%$) in Fig. 5.7(a). Therefore, the elastic relaxation due to the difference in the Ge content between island and DP has a significant effect on the critical island size for the introduction of the first dislocation. This behavior is quite general and can be expected in the whole experimental island AR range (0.2-0.35), see Fig. 5.6(a). To demonstrate that the influence of x_{DP} on the critical volume V_c on x_{DP} does not depend on the details of the island geometry (in the relevant AR range 0.2-0.35) considered, we repeated the calculations of the critical volumes V_c and of the elastic energy density ρ_{Ge}, by considering a barn-shaped island (AR=0.3) with barn Ge content x_B=0.3, as shown in Fig. 5.3(a). In Fig. 5.9 and in Fig. 5.10, it is plotted V_c and ρ_{Ge} as a function of the DP Ge content x_{DP} for a barn island. The trends observed are qualitatively the same as the ones predicted for dome-shaped islands. We notice that larger values of V_c are found considering barns, since the barn geometry allows for a better strain relaxation than the dome one.

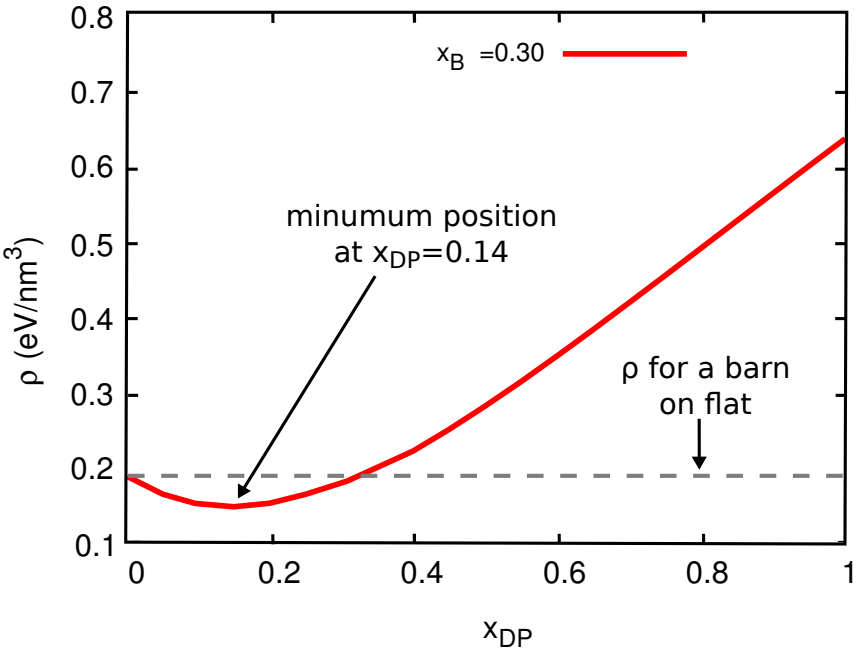

FIGURE 5.10: Elastic energy density in $Si_{1-x_D}Ge_{x_D}$ islands on pit-patterned Si(001) substrates as a function of the DP Ge content x_{DP}. The barn island Ge content is x_B=0.3.

5.4.4 Comparison between prediction and experiments

While the above analysis is particularly useful to understand the competition between dome and DP relaxation, in order to compare the predicted V_c values with experiments, as based on selective-etching measurements (see above and Ref. [186]), only results for low x_{DP} Ge content are relevant. We therefore repeated the calculation by setting x_{DP}=0.1 and varying x_D in the experimentally accessible range. Calculations repeated for x_{DP}=0.15 yielded analogous results, as shown in Fig. 5.11. While in the first case (x_{DP}=0.10) the dislocation equilibrium position is L_1 in almost the whole examined dome Ge content range ($x_D \gtrsim 0.3$), in the latter one, it correspond to line L_1 only for $x_D \gtrsim 0.45$. For the other pairs of x_D and x_{DP} values reported in Fig. 5.11, we found the dislocation line to assume the geometry denominated L_2 in its energy minimum. In the figure, filled circles (squares) represent experimental values for V_c on flat (pit-patterned) Si(001) substrates. The delay in plastic relaxation onset by patterning is quite evident in the whole T_{Ge} range also compared to a Ge content variation. We notice that V_c values in Fig. 5.11 refer to the dome island only. By considering the whole stressor volume (island+DP), comparison with the flat case would give an even larger delay. Theoretical results, reported in Fig. 5.11, correctly capture experimental trends, both in terms of larger V_c on patterned substrates and of dependence on the Ge content. For low x_D (high T_{Ge}) the model quantitatively reproduces experimental values. A tendency towards underestimating V_c for high x_D values is however found. This could be attributed to the simplifying assumption of a uniform SiGe distribution in the islands (resulting in an overestimate of the elastic budget, expected to be more critical at low temperatures [76]), and to kinetic

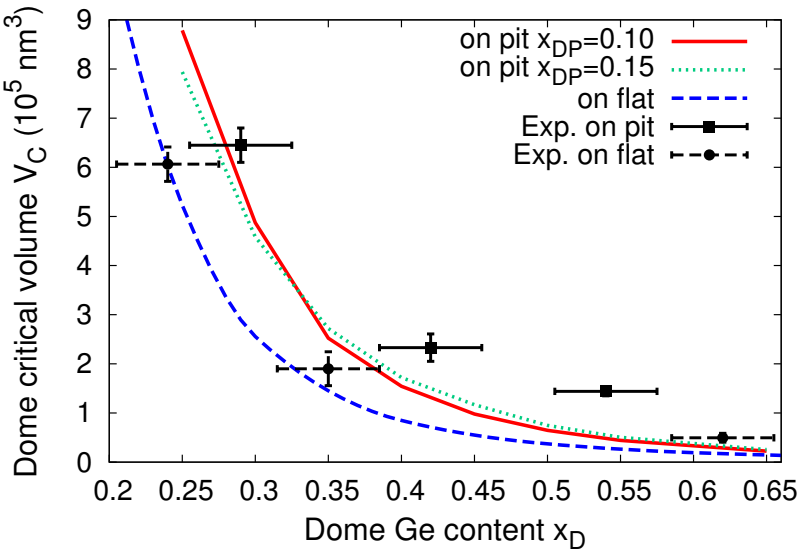

FIGURE 5.11: Critical volumes V_c for plasticity onset in $Si_{1-x_D}Ge_{x_D}$ islands on flat and on pit-patterned Si(001) substrates as a function of the dome Ge content x_D. [184]

limitations acting at lower temperatures, delaying the plasticity onset beyond the here-explored thermodynamic limit. Such effects seem to influence in the same way results for patterned and flat Si(001), leading in both cases to theoretical volumes ∼3 times smaller than experimental ones.

In conclusion we provide theoretical description of the role played by pit-patterning substrates in delaying plasticity onset in SiGe islands grown on Si(001). The critical volume V_c for islands grown in pits has been determined for the relevant island composition range and successfully compared to experiments. As attention was here focused on shallow pits, further research on optimal pit shapes/inclination could lead to growing even larger, fully coherent islands of potential interest as defect-free virtual substrates.

6

SiGe Nanowires

Semiconductor nanowires research is a flourishing field because of the unique properties of the nanowires, as their one-dimensional structure, their large surface to volume ratio, and the possibility of building advanced bottom-up architectures that are suitable for opto-electronic devices. Several research groups have demonstrated that nanowires can be exploited in different fields, as electronics, photonics and chemical sensors, allowing in the future to overcome the limits of the present technology. In the semiconductor research field, a lot of effort has been made in order to control the strain state in different heterostructures and to tailor the energy band-edge properties, as enhanced charge carrier transport [187, 188] and photoemission properties [189]. In growing such strained heterostructures, as two-dimensional films or islands, the plastic relaxation process is often an unavoidable strain-relief mechanism, as we have seen throughout the previous chapters. Nanowires represent a novel flexible geometry that can be exploited to obtained defect-free heterostructures with the desired properties. Obviously, dislocation formation remains a competitive strain relaxation mechanism also in these structures. For this reason, it is crucial to predict the critical condition for dislocation nucleation and to elucidate the mechanisms of their formation.

The work presented in this chapter is focused on a specific nanowire geometry, which is the core-shell heterostructure. In particular, we studied the Ge/Si material system. While there are several theoretical predictions for the coherency limit of both axial and radial nanowires [177, 190–196], the mechanisms for the nucleation and propagation of dislocations in core-shell nanowires are not yet clear. The strain relaxation in coherent and plastically relaxed core-shell Si/Ge nanowires has been analyzed and a possible mechanism for dislocation formation in such heterostructures has been proposed. We believe that most of the results obtained considering this system can be relevant also for other materials with zincblende structure, as III-V and II-VI semiconductors.

6.1 Core-shell Ge-Si nanowires

Core-shell nanowires of different material systems are currently object of interest [197–201]. Among them, the Ge/Si system is one of the most interesting from technological

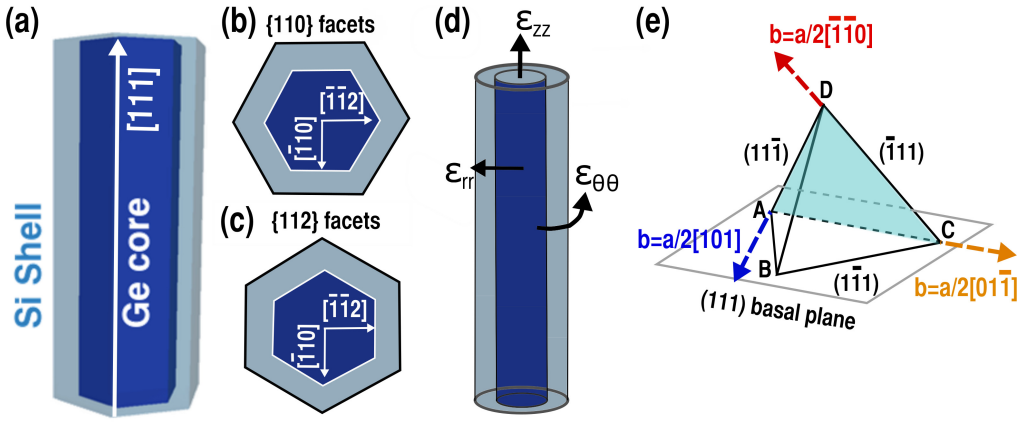

FIGURE 6.1: (a) Geometry of two nanowire configurations oriented along the ⟨111⟩ axis and hexagonal in base. (b) NW basal plane with {112} side facets and (c) with {110} facets. (d) Principal strain components in core-shell heterostructures: ε_{zz} along the axis of the NW, $\varepsilon_{\theta\theta}$ tangential to the NW circumference and ε_{rr} along the radius of the NW. (e) Tetrahedron bounded by {111} facets, indicating the orientation of the {111} slip planes with respect to the NW basal plane. The three possible Burgers vector lying in the ($\bar{1}$11) plane are indicated by the the arrows.

and basic band gap engineering perspectives [202–204]. Here Ge(core)/Si(shell) NWs grown on top of Si(111) substrates are investigated. Since the Ge/Si wires preferentially grow along the ⟨111⟩ directions, this substrate choice allows the alignment of the NWs perpendicularly to the substrate surface. The morphology of ⟨111⟩-oriented Si/Ge NWs is not well established. Some groups reported cylindrical NWs, with no discernible faceting observed in cross-sectional TEM imaging[205], while others observed NWs with six {112} [206] or {110} [207] side facets. It is worth to mention that for the Si/Ge system there are no stable facets parallel to the ⟨111⟩ growth direction, and surface roughness or sawtooth faceting [208] is typically observed on the NWs sidewalls. In this work we considered a simplified geometry of the NWs, with well defined sidewalls, as sketched in Fig. 6.1(a-c). In particular, we considered NWs aligned to the ⟨111⟩ direction and with hexagonal base in the two observed configurations, characterized by {110} and {112} side facets respectively. As can be seen in Fig. 6.1(b,c), these two NW geometries differ only in the orientation of the six sidewalls; the first one can be obtained by rotating the NW around its axis by 90° and vice versa.

6.2 Elastic relaxation in core-shell nanowires

Dislocations originate in semiconductor heterostructures because of the difference in the lattice parameter between two different materials. In order to understand the plastic relaxation processes in Ge/Si core-shell NWs it is important to quantify the strain state in the examined structures. In the previous chapters, we have analyzed SiGe islands and films grown on top of a Si substrate, where the misfit strain originates by the mismatch between the substrate and the epilayer. In core-shell NWs, due to the large height to

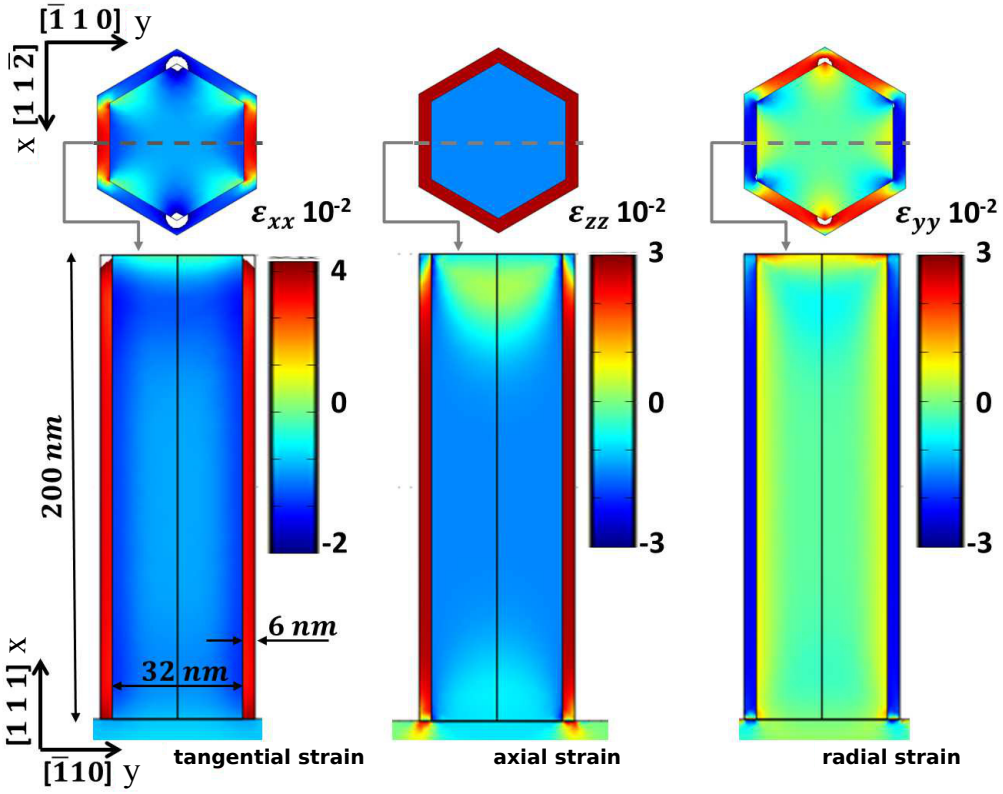

FIGURE 6.2: Maps of ε_{xx}, ε_{yy} and ε_{zz} strain components in a cross section of a Ge/Si core–shell NW perpendicular (top panels) and parallel (bottom panels) to the NW axis for a core radius R_{core}=32 nm and a shell thickness t_{shell}=6 nm. The x, y and z directions were set to be parallel to the tangential, radial and axial directions relative to the (11$\bar{2}$) facet. The maps were calculated by FEM.

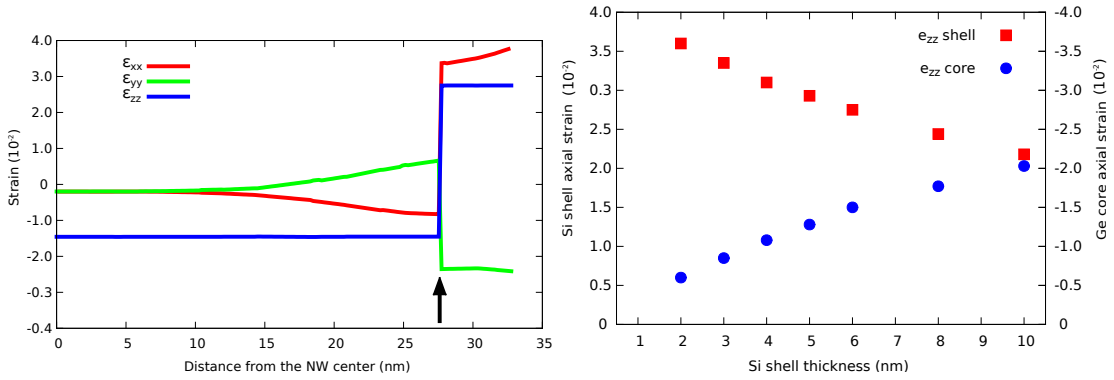

FIGURE 6.3: (a) Variation of the ε_{xx}, ε_{yy} and ε_{zz} strain components, along one of the radial direction ([$\bar{1}$10]), starting from the NW center to its surface. The x, y and z directions were set to be parallel to the tangential, radial and axial directions relative to the (11$\bar{2}$) facet. (b) Axial strain in the Ge core and the Si shell as function of the shell thickness. The core radius is set equal to 32 nm.

diameter ratio, strains arise by the mismatch between the core and the shell materials. In a first approximation, the misfit between the NW and the substrate can be neglected, because this strain only affects a small NW volume close to the substrate, due to the small NW base compared to its height. The three principal strain components in a simplified cylindrical core-shell geometry are the following: ε_{zz} along the axis of the NW, $\varepsilon_{\theta\theta}$, tangentially to the NW circumference, and ε_{rr} along the radius of the NW, as shown in Fig. 6.1(d). At each point of the NW, the first two components are parallel to the core-shell heterointerface, while the third one is perpendicular to it. While in the cylindrical geometry the tangential and radial directions change continuously, in NWs with hexagonal base, these directions remain constant for each NW facet and change discontinuously from one facet to the others. Let us analyze the elastic strain relaxation due to presence of the free surfaces. The misfit f_{Si} between pure Si and pure Ge is given by:

$$f_{Si} = \frac{a_{Si} - a_{Ge}}{a_{Ge}} \; ; \tag{6.1}$$

here we assumed $a_{Si} = 5.432$ Åand $a_{Ge} = 5.658$ Å, so that $f_{Si} = 0.042$.
In Fig. 6.2 the maps of the principal strain components ε_{xx}, ε_{yy} and ε_{zz} are plotted, assuming a reference system where z indicate the positive direction of the NW axis, x is parallel to the $[11\bar{2}]$ direction (tangential to the $[\bar{1}11]$ facet) and y is parallel to the $[\bar{1}10]$ direction (i.e. perpendicular to the $(\bar{1}10)$ NW facets. The strain field was calculated by FEM using the geometry sketched in Fig. 6.1(a,c); the core radius is 32 nm and the shell thickness is 6 nm. Isotropic elastic constants are assumed, so that the analysis of the strain components parallel and perpendicular to the selected facet, the $(\bar{1}10)$, can be extended by symmetry to the other facets. Also we can extend the strain analysis to the other NW configuration of interest, the one characterized by hexagonal base and {112} facets, as in 6.1(a) and (b). The three strain components shown at the top of Fig. 6.2 are plotted in a NW cross section parallel to basal plane and intersecting the NW center, while at the bottom of Fig. 6.2 are displayed in a cross-section parallel to the NW axis and perpendicular to the $[11\bar{2}]$ direction. As expected, the Si undergoes a tensile strain and the Ge core is under compression to partially relieve the misfit and to minimize the total elastic energy. Moreover, we observe no significant elastic relaxation of the tangential component, which is nearly equal to the misfit f_{Si} across the whole facet, except for the NW corners. On the contrary, the ε_{zz} strain component is $\sim$0.027, significantly lower than the 0.042 misfit value. In Fig. 6.3(a) we show the variation of the three strain components along the radial $[\bar{1}10]$ direction, starting from the center of the NW to the limit of the Si shell. The position of the core shell interface is indicated in Fig. 6.3(a) by an arrow. We notice that ε_{zz} is homogeneous across the core and the shell of the NW. In Fig. 6.3(b), we plot with blue circles (red squares) the variation of the axial strain in the NW core (shell) as a function of the shell thickness. From Fig. 6.3(b), it is clear that the thicker the shell the lower is the strain therein at expense of a larger core deformation. This is a consequence of the increased shell-thickness/core-radius ratio. When the shell volume is small compared to the core one, the strain is mainly accumulated in the thin shell. On the contrary when the shell volume becomes comparable or larger than the core one, the strain is redistributed between the shell and the core in order to minimize the total elastic

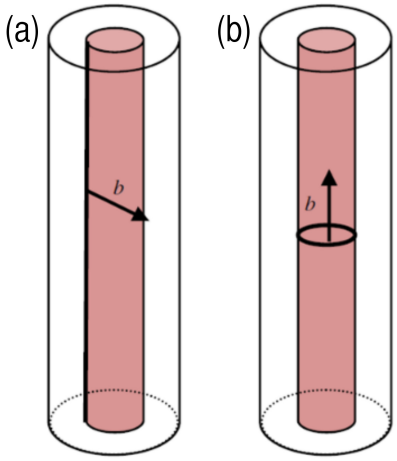

FIGURE 6.4: Diagram of dislocation lines and Burgers vectors for two possible geometries of the defects for core–shell nanowire heterostructures adopted in literature to calculate the critical shell thickness for dislocation formation. (a) The first, is a straight edge dislocation line parallel to the NW axis. The second is a Frank dislocation, i.e. pure edge or prismatic dislocation loop, around the nanowire core.

energy.

6.3 Plastic relaxation in core-shell nanowires

The deposition of the Si shell on the Ge core, causes initially the coherent growth of a thin Si layer which induces strain accumulation in both the shell and the core of the NW, as illustrated in the previous paragraph. As the deposition proceeds, the elastic energy accumulated in both the core and the shell layers eventually lead to defect formation in the NW. Previous works have considered edge dislocation lines or prismatic loops as possible sources of strain relief in core-shell heterostructured NWs. [191–196] The first set of dislocations is expected to lie within the shell parallel to NW axis, relieving the tangential strain, in the Burgers vector direction, as shown in Fig. 6.4(a), while the loops should follow the circumference of the NW core and relax the axial strain, as shown in Fig. 6.4(b). These two sets of dislocations can relax very efficiently the strain and several examples of pure edge dislocations observed in NW heterostructures are reported in literature.[209–211] However, such dislocations are unlikely to form by low energy glide processes, at least in the here examined NW structure, since their Burgers vector do not sit in low energy slip planes (the $\{111\}$ planes). In contrast, perfect dislocations with $b = a/2\langle 110\rangle$ Burgers vector can form through the glide of dislocation half-loops from the free surfaces to the core/shell interface. Reactions of two such dislocations have been used to explain the existence of pure edge dislocation lines in $\langle 001\rangle$-oriented ZB InAs-GaAs core shell NWs [212]. Recently, the critical shell thickness for plastic relaxation in ZB core-shell NWs has been investigated assuming the formation of a full misfit dislocation loop around the interface by glide but not demonstrating the formation mechanism.[213]

In this work, we theoretically predicted the formation of perfect dislocation segments in ⟨111⟩-oriented Si/Ge core-shell NWs, which is possible by gliding in the low-energy {111} slip planes, unlike the pure edge straight dislocations or the prismatic loops shown in Fig. 6.4. We determined the preferential nucleation sites and dislocation line directions of such defects and we demonstrated that the full loop formation by the gliding of a single dislocation is not favorable in the investigated system, as explained in the following paragraphs.

6.3.1 Resolved shear stress analysis

For [111] oriented NWs, there are three {111} slip planes {($\bar{1}11$), ($1\bar{1}1$), ($11\bar{1}$)} at angles of 19.5° from the growth axis and one parallel to the basal plane, the (111), (see Fig. 6.1(e)). A dislocation could nucleate on one edge of the NW and move in one of these slip planes by glide so as to deposit a misfit line at the Si/Ge interface. In order to elucidate the formation mechanism of perfect dislocations by glide and to identify the preferred nucleation sites, we first analyzed the heteroepitaxial stress field of the NW. The two simplified NW geometries characterized by {112} and {110} facets, as drawn in Fig. 6.1, were considered. The core radius and the shell thickness were set equal to 32 and 6 nm. The key quantity to identify the dislocation type (defined by slip plane and Burgers vector) which is favored in an existent stress field is the resolved shear stress (RSS), which is the stress resolved in the glide plane along the Burgers vector direction, as defined in Eq. 3.41. This is directly related to the force exerted by the external stress field on a given dislocation, moving in its glide plane. In Fig. 6.5(a-c), we plotted the resolved shear stress for dislocations having one of the three possible $a_{Si}/2\langle 110\rangle$ Burgers vectors lying on the ($\bar{1}11$) slip plane, indicated by the three arrows in Fig. 6.1(e), in a NW with {112} side facets. In the three panels, the RSS is visualized in a ($\bar{1}11$) plane across the NW and the three possible Burgers vectors are indicated by an arrow in the ($\bar{1}11$) planes. A large positive value of the RSS indicates a preferred site for dislocation nucleation and propagation. On the contrary, in case of zero or negative RSS the propagation of the same dislocation is hindered. Also, a negative RSS is found when the dislocation having the same slip plane but the opposite sign of the Burgers vector is favored. By looking at the RSS map in Fig. 6.5(a-c), we expect dislocations to nucleate at the NW corners where the RSS is maximum and to propagate in the Si shell volume where the RSS is positive, depositing a misfit line at the intersection between the glide plane and the Ge/Si interface, until it reaches the adjacent facet where the RSS assumes a negative or zero value. The RSS calculation for the $[01\bar{1}](\bar{1}11)$ and $[110](\bar{1}11)$, in the NW geometry characterized by {110} facets is reported in Fig. 6.6(a-b). The RSS map for the $[011](\bar{1}11)$ slip system is mirror symmetric to the one calculated for the $[110](\bar{1}11)$ slip system with respect to the [121] direction drawn in 6.6(b) and it is not reported here. Similarly to the previous case, we expect dislocations to preferentially nucleate at the NW corners and evolve towards the facets where the RSS is positive.

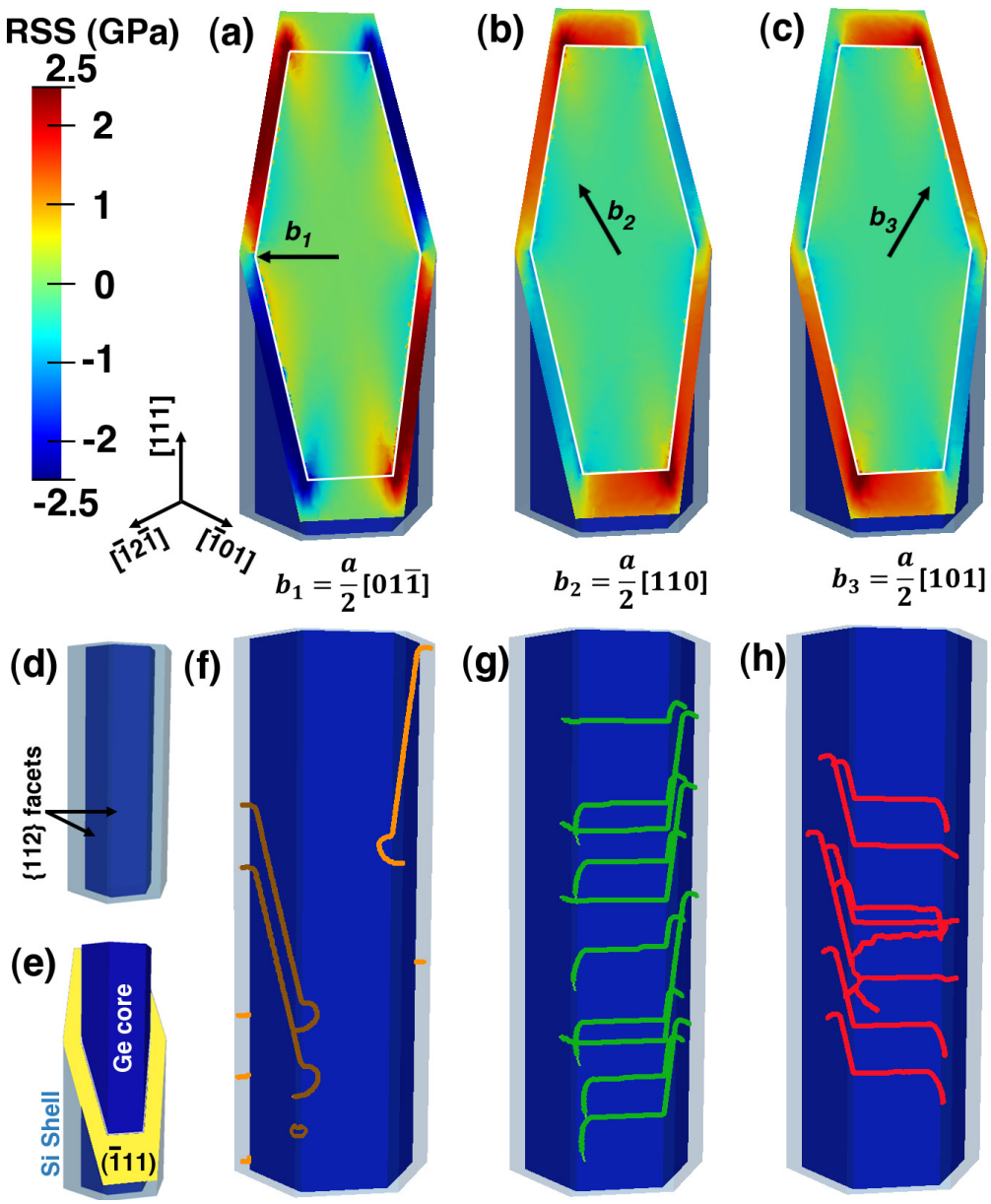

FIGURE 6.5: Resolved shear stress (RSS) variation in a ($\bar{1}$11) plane crossing a [111]-oriented NW with {112} facets for a dislocation with ($\bar{1}$11) slip plane and Burgers vector b_1 (a) and b_2 (b) and b_3(c). (d) Scheme of the NW geometry and (e) and a drawing of a ($\bar{1}$11) glide plane intersecting the Si shell (e). Equilibrium dislocation positions obtained by dislocation dynamics simulations through inserting small dislocation loops in the Si shell volume having ($\bar{1}$11) slip plane and Burgers vector b_1 (f) and b_2 (g) and b_3(h).

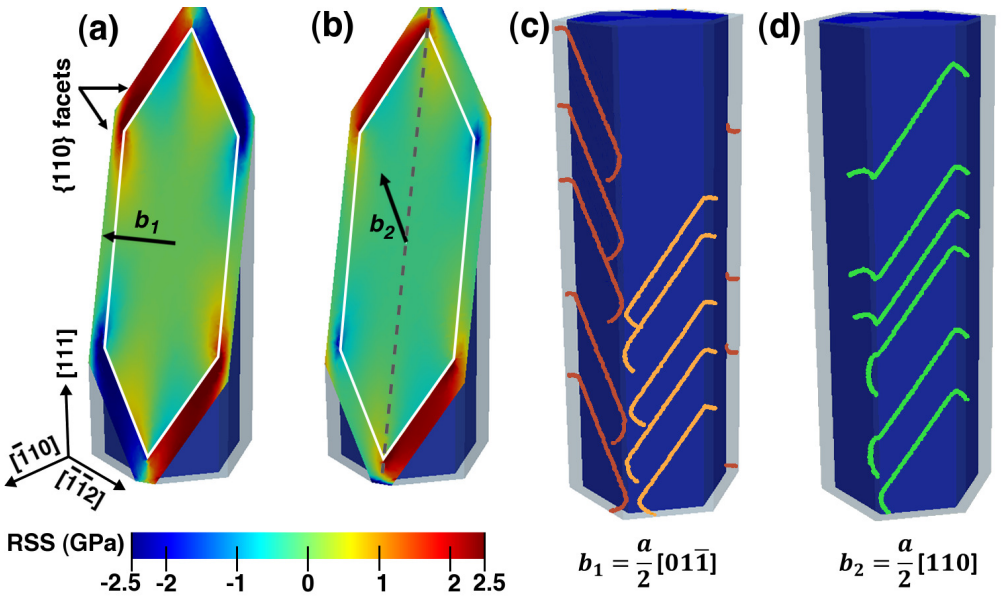

FIGURE 6.6: Resolved shear stress variation in a ($\bar{1}$11) plane crossing a [111]-oriented NW with {110} side facets, for a dislocation with ($\bar{1}$11) slip plane and Burgers vector b_1 (a) and b_2 (b). Equilibrium dislocation positions obtained by dislocation dynamics simulations through inserting small dislocation loops in the Si shell volume having ($\bar{1}$11) slip plane and Burgers vector b_1 (c) and b_2 (d).

6.3.2 Dislocation dynamics simulations

In order to support the shear stress analysis and to determine the equilibrium dislocation positions we performed dislocation dynamics (DD) simulations in the two NW configurations described above. The approach is similar to the one proposed for nanoislands in Ref. [125] and adopted for 2D thin films grown on pit-patterned substrates, reported in Chapter 4. First, the coherent stress field of the NW, calculated by FEM, is applied as external load in the simulations. Second, the dislocation-surface interaction is approximated by using the line-tension expression in Eq. 3.47, modified with respect to the typical bulk expression in order to mimic the force acting on segments touching the free surfaces [116, 125]. Finally the dynamics is solved by taking into account the epitaxial stress field, the line tension contribution and the stress field due to all the dislocations in the system. Dislocation loops with a 5 nm radius are periodically introduced in the DD simulations, following the procedure described in Section 3.5.3, testing at random position in the simulated Si shell volume if the newly introduced dislocation loop will expand in time in the actual stress field. Since we are interested in the mechanism of formation and evolution of a single gliding dislocations, we considered separately different slip systems and we stopped the simulations after the introduction and evolution of few loops. In Fig. 6.5(f-h) we show the simulation results in {112} facetted NWs, obtained by considering dislocations with $(\bar{1}11)$ glide plane and Burgers vector b_1 (f), b_2 (g) and b_3 (h). Results obtained for NWs characterized by {110} facets are shown in Fig. 6.6. In agreement with the RSS analysis, we observed the nucleation of dislocation loops preferentially at the NW corners, as shown in Fig. 6.5(f), where a small new loop is located at the NW edge position. Moreover, dislocations evolve from the NW corners in their slip plane, swapping the area in the Si shell where the RSS is positive, and depositing a misfit line at the Ge/Si interface. As a consequence, we observed some straight dislocation segments crossing a single NW facet, as in panel (f) in Fig. 6.5(f) and in Fig. 6.6(c,d), or dislocation segments that cross a NW corner depositing a misfit line on two adjacent facets, as in 6.5(g,h). Dislocations with $(\bar{1}11)$ slip plane and negative b_1, b_2 or b_3 Burgers vector are colored with dark lines. In agreement with the RSS calculations, these dislocation lines are found at positions where a negative RSS value is predicted.

In order to highlight the $\langle 110 \rangle \{111\}$ dislocation formation mechanism, we report in Fig. 6.7 several snapshots taken from a DD simulation and showing a dislocation loop evolution in a {112} facetted NW. The loop is nucleated on one NW corner (a); it expands under the tensile stress field touching the free surface (b). Then the two threading segments move towards the opposite sides further expanding the dislocation semi-loop (c) and depositing a misfit segment at the core-shell interface (d,e) until they reach the adjacent NW edges and they stop (f). Since the residual strain affects the optical and electronic properties of NW heterostructures, it is important to evaluate how efficiently the predicted dislocation segments can relieve the axial and the tangential strains in the NWs. To this aim, we calculated the effective Burgers vector component b_{eff} by projecting the edge component of the Burgers vector into the core-shell interface per each NW facet and the b_{eff} projections along the axial $b_{eff,z}$ and tangential $b_{eff,\theta}$ directions. In Tab. 6.1, we reported the predicted misfit line directions $\boldsymbol{\xi}$ and the b_{eff} values obtained by considering one of the

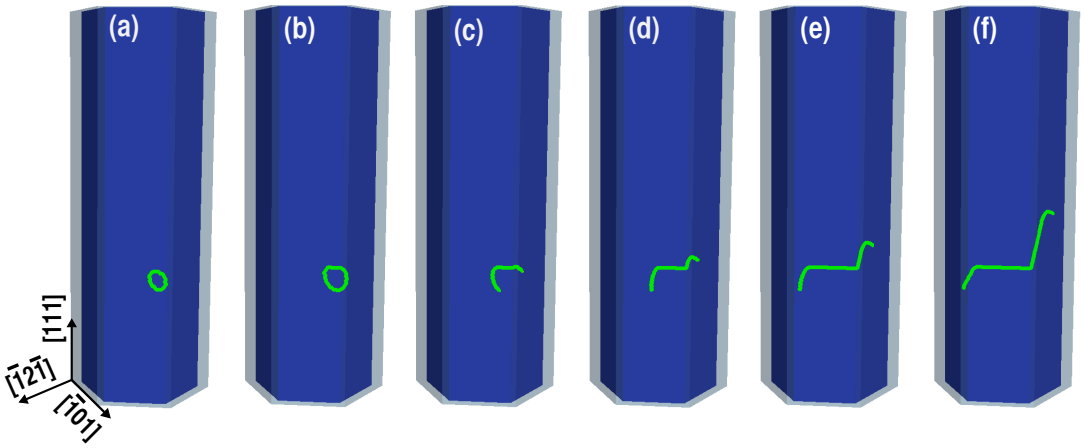

FIGURE 6.7: Snapshots showing the evolution of a dislocation loop with $[110](\bar{1}11)$ slip system by dislocation dynamics simulations in a [111]-oriented core-shell Ge/Si NW.

three oblique slip plane, the $(\bar{1}11)$, and the three Burgers vectors lying in such a plane. The misfit segments directions $\boldsymbol{\xi}$ are given by the intersection of the analyzed slip plane with the interface planes. The normal vectors to these planes are indicated in Tab. 6.1 by n_f. Moreover, we indicate with a + or a − the Burgers vector sign which is expected to relax the misfit strain in the Si volume adjacent to the facet n_f[1]. For NWs with {112} facets the misfit lines observed in the DD simulations are parallel to the $\langle 110 \rangle$ directions lying in the (111) basal plane or aligned with the $\langle 123 \rangle$ directions. The dislocation lines perpendicular to the NW growth axis, as shown in Fig. 6.5(g,h), have an edge component of the Burgers vector projected along the NW axis equal to $b_z = a_{Si}/3[111]$ (equal to 0.817 b) and relieve the maximum axial strain but not the tangential one. The position of the extra half-plane in the Si shell connected with such dislocation geometry is aligned to the $[\bar{2}11]$ direction, in excellent agreement with recent experimental observations [214] reported below. The oblique $\langle 123 \rangle$ segments can relax both the axial and the tangential strains. Of these dislocation types, we never observed in our DD simulations, dislocation lines which have the smallest b_{eff} value ($0.154b$), see Tab. 6.1, probably because the energy gain due to the strain reduction induced by this dislocation geometry is low compared the cost of creating such a defect. By looking at the $b_{eff,z}$ and $b_{eff,\theta}$ values we expect that NWs with {112} facets undergo a larger strain relaxation of the axial component compared to the tangential one. On the contrary, in NWs with {110} facets, the misfit lines as obtained by DD simulations are parallel to the $\langle 110 \rangle$ directions and relax more effectively the tangential strain component. By observing the results in Tab. 6.1, it is clear that a single perfect dislocation is not expected to form a full loop around the core, because it can effectively relax the misfit strain only at the interface of one or two adjacent NW facets. Thus, the threading dislocation motion, and consequently the deposition of a misfit segment, is stopped at the border of the NW interface facet where the dislocation geometry induce any strain relief in the NW heterostructure. This prevent the formation

[1]Keeping fixed the dislocation line direction $\boldsymbol{\xi}$

Dislocations with ($\bar{1}11$) slip plane						
[111]-oriented NW with {112} facets						
b	n_f	ξ	b_{eff}	$b_{eff,z}$	$b_{eff,\theta}$	b sign
$a_{Si}/2[01\bar{1}]$	$[1\bar{2}1]$	[321]	0.463 b	0.428 b	0.175 b	−
	$[2\bar{1}\bar{1}]$	$[01\bar{1}]$	0	0	0	none
	$[\bar{1}\bar{1}2]$	[312]	0.463 b	0.428 b	0.175 b	+
$a_{Si}/2[110]$	$[1\bar{2}1]$	[321]	0.154 b	0.058 b	0.143 b	−
	$[2\bar{1}\bar{1}]$	$[01\bar{1}]$	0.817 b	0.817 b	0	+
	$[\bar{1}\bar{1}2]$	[312]	0.310 b	0.117 b	0.286 b	+
$a_{Si}/2[101]$	$[1\bar{2}1]$	[321]	0.310 b	0.117 b	0.286 b	+
	$[2\bar{1}\bar{1}]$	$[01\bar{1}]$	0.817 b	0.817 b	0	+
	$[\bar{1}\bar{1}2]$	[312]	0.154 b	0.058 b	0.143 b	−
[111]-oriented NW with {110} facets						
b	n_f	ξ	b_{eff}	$b_{eff,z}$	$b_{eff,\theta}$	b sign
$a_{Si}/2[01\bar{1}]$	$[\bar{1}10]$	$[\bar{1}\bar{1}0]$	0.701 b	0.408 b	0.577 b	−
	$[\bar{1}01]$	[101]	0.701 b	0.408 b	0.577 b	+
	$[0\bar{1}1]$	[211]	0	0	0	none
$a_{Si}/2[110]$	$[\bar{1}10]$	[101]	0	0	0	none
	$[\bar{1}01]$	[101]	0.701 b	0.408 b	0.577 b	+
	$[0\bar{1}1]$	[211]	0	0	0	none
$a_{Si}/2[101]$	$[\bar{1}10]$	[101]	0.701 b	0.408 b	0.577 b	+
	$[\bar{1}01]$	[101]	0	0	0	none
	$[0\bar{1}1]$	[211]	0	0	0	none

TABLE 6.1: Misfit dislocation line directions χ and their effective Burgers vector b_{eff} values in [111]-oriented core-shell NWs with {112} and {110} facets. Dislocations with ($\bar{1}11$) slip plane and the three Burgers vectors b lying in such a plane are considered. n_f indicate the vector normal to each NW interface facet, χ the dislocation line direction deposited at the corresponding facets. $b_{eff,z}$ and $b_{eff,\theta}$ are the projections of the edge component of the Burgers vector on the NW interface planes n_f.

of a perfect dislocation loop around the NW core.

Dislocation evolution in the other two oblique slip planes $(1\bar{1}1)$, $(11\bar{1})$ led to similar dislocation line arrangements in the adjacent NW facets, that contribute to axial and tangential strain relaxation in the whole Si volume. On the contrary, no propagation of loops in the basal (111) plane was ever observed. This can be explained by considering that the possible Burgers vector $\boldsymbol{b}$ lying in the (111) planes can always be decomposed into two components, which are, respectively, parallel to the lateral NW facets (along the tangential direction) and parallel to the NW facets normal (along the radial direction). We notice that the $\boldsymbol{b}$ component parallel to the tangential direction is also aligned to the misfit dislocation direction at the core-shell interface; hence, it is screw in character and it cannot relieve the misfit strain. The edge component of $\boldsymbol{b}$ can only be parallel to the radial direction. Since this component is perpendicular to the core-shell interface, it does not

contribute to the interfacial strain relaxation. Hence, we do not expect such dislocations in the examined NW structures, as confirmed by our DD simulations.

A critical shell thickness for dislocation formation, can be extrapolated by the DD simulation results. We notice that, dislocation loop expansion, followed by misfit segments deposition, has been observed in the DD simulations by introducing small loops of radius R=5 nm. It follows that the critical radius R_c for loop expansion in the examined NW geometry (32 nm of Ge core radius), must be $R_c < R <$5 nm. From this information we can extrapolate an upper limit for the critical shell thickness by using Eq. 2.10, as derived in Section 2.4.3: $h_c = R_c \sin\phi$, where ϕ is the angle between the glide plane and the NW interface facets. In particular, for NWs bounded by {110} facets the angle between the oblique {111} glide planes and the {110} side facets is constant and we obtain: $h_{c,110} = R_c \sin\phi_{110} < Rsin\phi_{110} <$ 2.5 nm. Similarly h_c can be evaluated for different dislocation and NW geometries, facet orientations and misfit values, providing at least a rough estime of the expected critical shell thickness in the desire NW heterostructure.

6.3.3 Comparison with experiments

The theoretical predictions presented in this chapter, allowed us to interpret recent experiments performed by Dr. S. A. Dayeh and coworkers on Si-Ge core-shell NWs [214], where dislocation glide in {111} planes has been observed in [111]-oriented Ge/Si core-shell NWs, mostly characterized by {112} side facets. In particular, perfect dislocations with Burgers vector $a_{Si}/2\langle 110\rangle$ have been identified at the core-shell interface after post-annealing processes at 600 °C. Such dislocations were observed in NWs with a 16 nm core radius at a thickness of 3.2 nm up to 5 nm, and were by identified by the additional strain relieving Si (111) planes with respect to Ge, observed along the growth axis of the NW that had a projected component of the Burgers vector of $\boldsymbol{b_z} = a_{Si}/3[111]$, as shown in Fig. 6.8. The norm of the latter vector is $0.817b$, as expected for dislocations with $(\bar{1}11)$ slip plane and Burgers vector $a_{Si}/2[110]$ and $a_{Si}/2[101]$, as reported in Tab. 6.1, and dislocations with similar geometry but gliding in the other two oblique {111} slip planes. An example of a dislocation with such a geometry is shown in Fig. 6.5(g,h), where the dislocation segments parallel to the (111) basal plane have $b_{eff} = b_{eff,z}$=$0.817b$, fully compatible with the measured value. Moreover these predicted dislocation lines produce an extra half-plane in the Si shell perpendicular to the interface and along the dislocation line (in the direction defined by $\boldsymbol{\xi} \times \boldsymbol{b_{edge}}$), which is in agreement with the extra Si plane observed in the experiments and indicated by the red signs in Fig. 6.8. As we can see in Fig. 6.8(b), the extra Si planes associated with the dislocations are observed in the NW cross-section only at one surface of the Si shell on the same (111) plane orthogonal to the growth direction, which further confirms that these dislocations are not pure edge loop as the one sketched in Fig. 6.4(b) and considered in previous works [192, 193, 196]. Therefore, our predictions based on the resolved shear stress analysis and on dislocation dynamics simulations are in good agreement with experimental observations in core-shell Ge-Si NWs and shed light on nucleation sites, propagation, and termination of dislocations in the Si volume.

In conclusions, a mechanism for strain relief in core-shell Si-Ge nanowires via dislo-

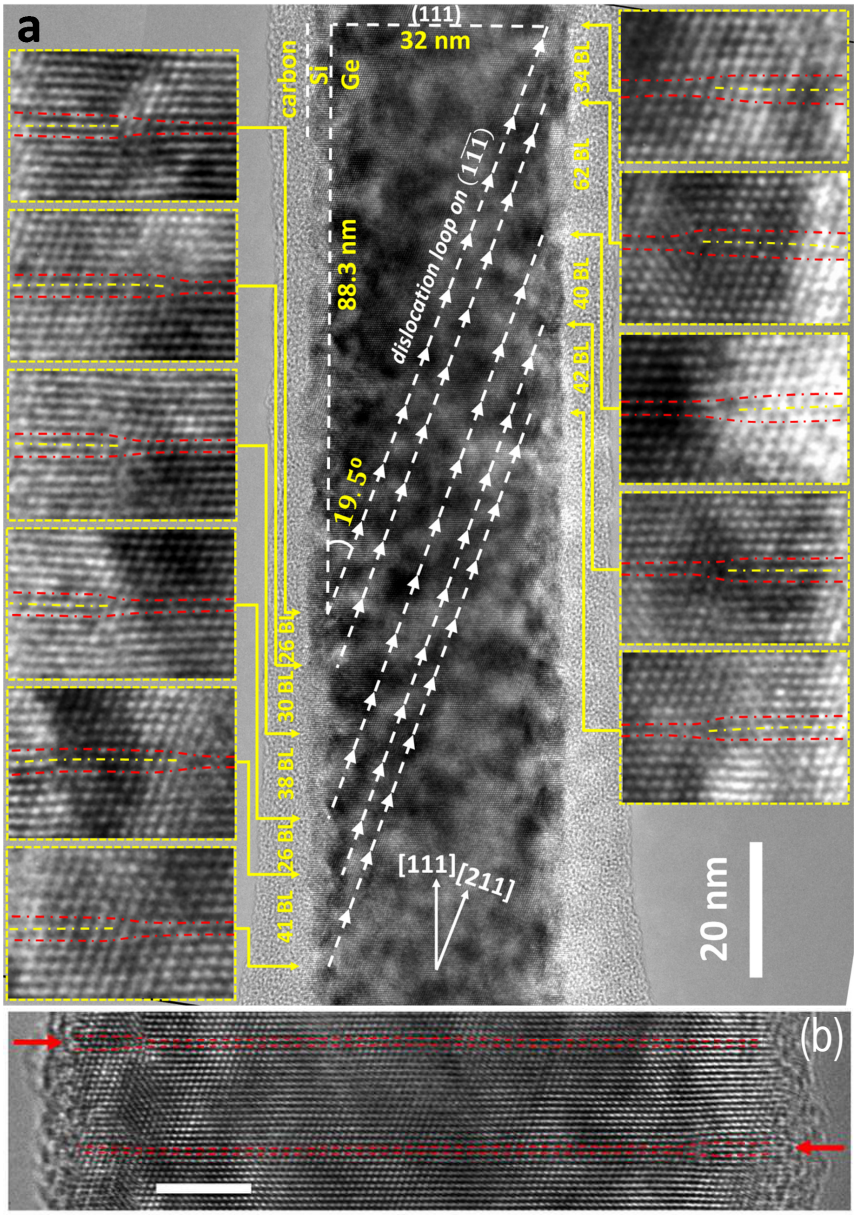

FIGURE 6.8: HRTEM images of Ge/Si core/shell NW imaged from a ¡110¿ zone axis. (a) Sideview image (beam direction $\langle 01\bar{1} \rangle$) over a sufficient axial distance to observe several $a_{Si}/2 < 110 >$ perfect dislocation segments formed by glide along the circumference of the NW. The insets are enlarged portions from the same image indicating the locations of extra Si (111) planes. (b) Nw cross section showing that the extra half-planes observed at one side of the NW are not present at the opposite side, confirming that no edge dislocation loops (Frank dislocations) parallel to the (111) NW base exist in the NW. Scale bar is 5 nm. Courtesy of S. A. Dayeh.

cation nucleation and glide on {111} planes is presented. The latter should lead to the development of a periodic pattern of misfit segments deposited at the core-shell interface with a different orientation depending on the specific facet where the dislocation nucleate. These dislocation segments contribute differently to the axial and tangential strain relaxation. The critical shell size for dislocation formation has been evaluated in the analyzed configuration, but further investigations can lead to the determination of the coherency limits in core-shell nanowires characterized by different misfit values and core radii.

Conclusions

Plastic relaxation in different epitaxial nanostructures has been investigated by using a continuum approach. In particular, finite element calculations allowed us to determine the strain state and the energetics of coherent and dislocated epitaxial heterostructures. As a consequence, we found the equilibrium configuration of dislocations in thin films grown on trench-patterned Si substrates, in epitaxial islands nucleated in pits and in core-shell Ge-Si nanowires. Also the stress field analysis in epitaxial films grown on pit and trench patterned substrates and in core shell nanowires allowed us to determine the preferential nucleation sites for dislocations in such nanostructures. Dislocations dynamics simulations have been performed to confirm this analysis and to determine the dislocation pattern expected in the same nanostructures.

The predictions obtained from our models on plastic relaxation in SiGe film, demonstrated that by suitably patterning the Si substrate with {111} trenches or pits, it is possible to introduce high stress concentrations in low misfit epitaxial films grown conformally to the template. These operate as preferential sites for dislocation nucleation and threading dislocation trapping. In particular, by using trench patterned substrates, misfit dislocations parallel to the trenches are effectively confined at the {111} sidewalls. Moreover, threading segments running perpendicularly to the trenches are found to be stopped at the trench facets. By using pit patterned substrates, a regular array of misfit dislocations running along the pit lines is found, providing large dislocation free areas, suitable for device integration. It is therefore possible to fabricate relatively large areas free of detrimental dislocations, without using non-connected substrates or selective area deposition in oxide windows.

Investigation of dislocation formation in nanoislands allowed us to explain the ordering of misfit dislocation segments at the base of heteroepitaxial SiGe islands on planar Si(001) substrates, by using a simple analytical model. This is determined by the periodic matching of the thermodynamic critical conditions for dislocation formation in the island. A theoretical description of the role played by pit-patterning substrates in delaying plasticity onset in SiGe islands grown on Si(001) was provided. The critical volume for islands grown in pits has been determined for the relevant island composition range and successfully compared to experiments. Further investigation of different pattern geometries, could lead to the growth of fully coherent and even larger islands, that can be exploited as defect-free virtual substrates.

A framework for understanding strain relaxation in core-shell nanowires was provided. In particular, we have verified the possibility to form perfect dislocations via nucleation

and glide on the low energy {111} slip planes. This leads to a periodic pattern of misfit segments at the interface, with orientation dependent on the specific nanowire facet where the dislocations nucleate. The formation of these misfit dislocation segments can lead to different degree of axial and radial strain relaxation. It follows, that it becomes conceivable to tailor axial and tangential stresses separately, opening new possibility for strain and band-gap engineering. Finally, the coherency limits for core/shell nanowires was evaluated in the specific nanowire configuration we analyzed, but further investigations can lead to the prediction of the critical shell thickness for different core radii and misfit values.

Our predictions on films, islands and nanowires were successfully compared with experiments. The accurate level of agreement obtained between real and simulated dislocation microstructures in all the systems investigated proves the strength of the modelling methodology here proposed. We believe that our approach can be useful to investigate the full plastic relaxation process in different heteroepitaxial architectures addressing key issues, such as determining the coherency limits in realistic shaped nanostructures, assessing the influence of the substrate patterning geometry on the onset of plastic relaxation and on dislocation gettering processes, and to obtain at least qualitative insight into the relevant dislocation nucleation mechanisms. The behavior predicted in Si-Ge heteroepitaxial structures is expected to be quite general, at least for other semiconductor materials with zincblende structure, and opens up the possibility to exploit substrate patterning with different geometries to govern dislocation nucleation and propagation in mismatched nanoislands and thin films.

Acknowledgements

First, I would like to acknowledge my supervisor Prof. Leo Miglio who introduced me to the research field of nanotechnology and gave me the opportunity to carry on the PhD research activity. I also thank him for his precious advise and support.

I sincerely thank Francesco Montalenti for his constant help and support during the entire PhD time.

I am grateful to Benoit Devincre who hosted me at the Laboratoire d'Etude des Microstructures in Paris, introduced me to dislocation dynamics simulations and taught me this technique. I also would like to acknowledge Riccardo Gatti for his valuable help in performing the dislocation dynamics simulations presented in this work. I thank both of them for helping me day by day during the period spent in Paris and for the continuous collaboration and support.

The investigation of plastic relaxation in epitaxial films and islands grown on pit patterned substrates was carried out in collaboration with the group of Prof. Bauer and Prof. Shäffler at the university of Linz. The intriguing experiments performed in this group and presented throughout this work, motivated the detailed analysis of dislocation formation in such nanostructures. All the people contributing to this work are acknowledged for their valuable work and the helpful scientific discussions. In particular, I would like to thank Prof. Bauer, Prof. Shäffler, M. Grydlik, M. Brehm and H. Groiss for the continuous and fruitful collaboration.

The theoretical investigation of dislocation formation in core-shell nanowire was done in collaboration with S. A. Dayeh, working at the Los Alamos National Laboratory and coworkers, in the attempt to explain the dislocation pattern observed in Ge-Si core-shell nanowires. I would like to thank particularly S. A. Dayeh and K. Kavenagh for our collaboration and the helpful discussions.

Finally I would like to thank all the people in the group of Prof. Miglio, the ones who are presently part of it (Roberto, Daniele, Anna, Marco, Matteo) and that were part of it during my PhD time (Riccardo), for their continuous support, help and friendship.

Publications

Publications related to the thesis work

- F. Boioli, V. A. Zinovyev, R. Gatti, A. Marzegalli, F. Montalenti, M. Stoffel, T. Merdzhanova, L. Wang, F. Pezzoli, A. Rastelli, O. G. Schmidt, and L. Miglio "Self-Ordering of Misfit Dislocation Segments in Epitaxial SiGe Islands on Si(001)" - J. Appl. Phys. 110, 044310 (2011)

- R. Gatti, F. Boioli, M. Grydlik, M. Brehm, H. Groiß, F. Montalenti, T. Fromherz, F. Schäffler, G. Bauer, and L. Miglio "Dislocation engineering in SiGe heteroepitaxial films on patterned Si (001) substrates" - Appl. Phys. Lett. 98, 121908 (2011)

- F. Boioli, R. Gatti, M. Grydlik, M. Brehm, F. Montalenti, and L. Miglio "Assessing the delay of plastic relaxation onset in SiGe islands grown on pit-patterned Si (001) substrates" - Appl. Phys. Lett. 99, 033106 (2011)

- M. Grydlik, F. Boioli, H. Groiß, R. Gatti, M. Brehm, F. Montalenti, B. Devincre, F. Schäffler, and L. Miglio "Misfit dislocation gettering by substrate pit-patterning in SiGe films on Si (001)" - Appl. Phys. Lett. 101, 013119 (2012)

- S. A. Dayeh, W. Tang, F. Boioli, K. L. Kavanagh, H. Zheng, J. Wang, N. H. Mack, G. Swadener, J. Y. Huang, L. Miglio, K.-N. Tu, and S. T. Picraux "Direct Measurement of Coherency Limits for Strain Relaxation in Heteroepitaxial Core/Shell Nanowires" - Nano Lett. (accepted)

Other Publications

- G. Vastola, M. Grydlik, M. Brehm, T. Fromherz, G. Bauer, F. Boioli, L. Miglio and F. Montalenti "How pit facet inclination drives heteroepitaxial island positioning on patterned substrates" - Phys. Rev. B 84, 155415 (2011)

- R. Gatti, F. Pezzoli, F. Boioli, F. Montalenti, and L. Miglio "Assessing the composition of hetero-epitaxial islands via morphological analysis: an analytical model matching GeSi/Si(001) data" - J. Phys.: Condens. Matter 24, 104018 (2012)

Bibliography

[1] D. Hull and D. J. Bacon, *Introduction to Dislocations* (Butterworth-Heinemann, 2001).

[2] J. Weertman and J. R. Weertman, *Elementary Dislocation Theory* (Macmillan Series in Materials Science, 1964).

[3] J. P. Hirth and J. Lothe, *Theory of Dislocations* (Krieger, Malabar, 1992).

[4] F. R. N. Nabarro, Advances in Physics **1**, 284 (1952).

[5] V. V. Bulatov and W. Cai, *Computer simulations of dislocations* (Oxford Series on Materials Modelling, 2006).

[6] F. C. Frank, Physica **15**, 131 (1949).

[7] Y. Zhu, X. Wu, X. Liao, J. Narayan, L. Kecskés, and S. Mathaudhu, Acta Materialia **59**, 812 (2011).

[8] J. E. Ayers, *Heteroepitaxy of semiconductors. Theory, growth and characterization* (CRC press, Taylor and Francis Group, 2007).

[9] M. A. Herman and H. Sitter, *Molecular Bean Epitaxy: Fundamentals and Current status* (Springer verlag, New york, 1988).

[10] M. H. Grabow and G. H. Gilmer, Surface Science **194**, 333 (1988).

[11] I. Daruka and A.-L. Barabási, Physical Review Letters **79**, 3708 (1997).

[12] B. Voigtländer, Surface Science Reports **43**, 127 (2001).

[13] J. P. Dismukes, L. Ekstrom, and R. J. Paff, Journal of Physical Chemistry **68**, 3021 (1964).

[14] Y. Ishikawa, K. Wada, J. Liu, D. D. Cannon, H.-C. Luan, J. Michel, and L. C. Kimerling, Journal of Applied Physics **98**, 013501 (2005).

[15] Y. Okada and Y. Tokumaru, Journal of Applied Physics **56**, 314 (1984).

[16] R. J. Asaro and W. A. Tiller, Metallurgical Transactions A **3**, 1780 (1972).

[17] M. A. Grinfeld, Sov. Phys. Dokl. **31**, 831 (1986).

[18] Y. Tu and J. Tersoff, Physical Review Letters **93**, 216101 (2004).

[19] A. Sakai and T. Tatsumi, Applied Physics Letters **64**, 52 (1994).

[20] J. H. Van Der Merwe, Journal of Applied Physics **34**, 117 (1963).

[21] J. H. Van Der Merwe, Journal of Applied Physics **34**, 123 (1963).

[22] E. Kasper and H.-J. Herzog, Thin Solid Films **44**, 357 (1977).

[23] E. Kasper, Surface Science **174**, 630 (1986).

[24] J. W. Matthews, Journal of Vacuum Science and Technology **12**, 126 (1975).

[25] Y. Shiraki and A. Sakai, Surface Science Reports **59**, 153 (2005).

[26] J. Matthews and A. Blakeslee, Journal of Crystal Growth **27**, 118 (1974).

[27] J. C. Bean, L. C. Feldman, A. T. Fiory, S. Nakahara, and I. K. Robinson, Journal of Vacuum Science and Technology A **2**, 436 (1984).

[28] R. People and J. C. Bean, Applied Physics Letters **49**, 229 (1986).

[29] J. Bevk, J. P. Mannaerts, L. C. Feldman, B. A. Davidson, and A. Ourmazd, Applied Physics Letters **49**, 286 (1986).

[30] D. C. Houghton, C. J. Gibbings, C. G. Tuppen, M. H. Lyons, and M. A. G. Halliwell, Applied Physics Letters **56**, 460 (1990).

[31] D. C. Houghton, D. D. Perovic, J.-M. Baribeau, and G. C. Weatherly, Journal of Applied Physics **67**, 1850 (1990).

[32] M. L. Green, B. E. Weir, D. Brasen, Y. F. Hsieh, G. Higashi, A. Feygenson, L. C. Feldman, and R. L. Headrick, Journal of Applied Physics **69**, 745 (1991).

[33] R. People and J. C. Bean, Applied Physics Letters **47**, 322 (1985).

[34] J. W. Matthews, S. Mader, and T. B. Light, Journal of Applied Physics **41**, 3800 (1970).

[35] B. W. Dodson and J. Y. Tsao, Applied Physics Letters **51**, 1325 (1987).

[36] J. Y. Tsao, B. W. Dodson, S. T. Picraux, and D. M. Cornelison, Physical Review Letters **59**, 2455 (1987).

[37] J. Matthews, A. Blakeslee, and S. Mader, Thin Solid Films **33**, 253 (1976).

[38] R. Hull and J. C. Bean, Journal of Vacuum Science and Technology A **7**, 2580 (1989).

[39] U. Jain, S. C. Jain, A. H. Harker, and R. Bullough, Journal of Applied Physics **77**, 103 (1995).

[40] D. E. Jesson, S. J. Pennycook, J. M. Baribeau, and D. C. Houghton, Physical Review Letters **71**, 1744 (1993).

[41] H. Gao and W. D. Nix, Annual Review of Material Science **29**, 173 (1999).

[42] W. Hagen and H. Strunk, Applied Physics Letters **17**, 85 (1978).

[43] J. D. P. A. Lefebvre, C. Herbeaux, Philosophical Magazine A **63**, 471 (1991).

[44] F. K. LeGoues, B. S. Meyerson, J. F. Morar, and P. D. Kirchner, Journal of Applied Physics **71**, 4230 (1992).

[45] R. Beanland, Journal of Applied Physics **72**, 4031 (1992).

[46] C. G. Tuppen, C. J. Gibbings, M. Hockly, and S. G. Roberts, Applied Physics Letters **56**, 54 (1990).

[47] J. Washburn and E. P. Kvam, Applied Physics Letters **57**, 1637 (1990).

[48] Y.-W. Mo, D. E. Savage, B. S. Swartzentruber, and M. G. Lagally, Physical Review Letters **65**, 1020 (1990).

[49] D. J. Eaglesham and M. Cerullo, Physical Review Letters **64**, 1943 (1990).

[50] J. Stangl, V. Holý, and G. Bauer, Review of Modern Physics **76**, 725 (2004).

[51] I. Berbezier and A. Ronda, Surface Science Reports **47**, 64 (2009).

[52] L. Miglio and F. Montalenti, "Silicon-germanium (sige) nanostructures: Production, properties, and applications in electronics," (Woodhead Publishing - UK, 2011) Chap. 10.

[53] G. Medeiros-Ribeiro, A. M. Bratkovski, T. I. Kamins, D. A. A. Ohlberg, and R. S. Williams, Science **279**, 353 (1998).

[54] M. J. Beck, A. van de Walle, and M. Asta, Physical Review B **70**, 205337 (2004).

[55] G.-H. Lu, M. Cuma, and F. Liu, Physical Review B **72**, 125415 (2005).

[56] A. Vailionis, B. Cho, G. Glass, P. Desjardins, D. G. Cahill, and J. E. Greene, Physical Review Letters **85**, 3672 (2000).

[57] F. M. Ross and R. M. Tromp, Science **286**, 1931 (1999).

[58] M. Stoffel, A. Rastelli, J. Tersoff, T. Merdzhanova, and O. G. Schmidt, Physical Review B **74**, 155326 (2006).

[59] E. Sutter, P. Sutter, and J. E. Bernard, Applied Physics Letters **84**, 2262 (2004).

[60] A. Rastelli and H. von Kanel, Surface Science **515**, L493 (2002).

[61] F. K. LeGoues, M. C. Reuter, J. Tersoff, M. Hammar, and R. M. Tromp, Physical Review Letters **73**, 300 (1994).

[62] M. Brehm, F. Montalenti, M. Grydlik, G. Vastola, H. Lichtenberger, N. Hrauda, M. J. Beck, T. Fromherz, F. Schäffler, L. Miglio, and G. Bauer, Physical Review B **80**, 205321 (2009).

[63] H. T. Johnson and L. B. Freund, Journal of Applied Physics **81**, 6081 (1997).

[64] R. Gatti, F. Pezzoli, F. Boioli, F. Montalenti, and L. Miglio, Journal of Physics: Condensed Matter **24**, 104018 (2012).

[65] G. Capellini, M. D. Seta, and F. Evangelisti, Applied Physics Letters **78**, 303 (2001).

[66] M. Brehm, M. Grydlik, H. Lichtenberger, T. Fromherz, N. Hrauda, W. Jantsch, F. Schaffler, and G. Bauer, Applied Physics Letters **93**, 121901 (2008).

[67] S. A. Chaparro, Y. Zhang, and J. Drucker, Applied Physics Letters **76**, 3534 (2000).

[68] Y. Tu and J. Tersoff, Physical Review Letters **98**, 096103 (2007).

[69] G. Medeiros-Ribeiro and R. S. Williams, Nano Letters **7**, 223 (2007).

[70] F. Zipoli, S. Cereda, M. Ceriotti, M. Bernasconi, L. Miglio, and F. Montalenti, Applied Physics Letters **92**, 191908 (2008).

[71] J. Tersoff, Applied Physics Letters **83**, 353 (2003).

[72] M. Floyd, Y. Zhang, K. P. Driver, J. Drucker, P. A. Crozier, and D. J. Smith, Applied Physics Letters **82**, 1473 (2003).

[73] T. U. Schülli, M. Stoffel, A. Hesse, J. Stangl, R. T. Lechner, E. Wintersberger, M. Sztucki, T. H. Metzger, O. G. Schmidt, and G. Bauer, Physical Review B **71**, 035326 (2005).

[74] M. D. Seta, G. Capellini, F. Evangelisti, and C. Spinella, Journal of Applied Physics **92**, 614 (2002).

[75] A. Marzegalli, V. A. Zinovyev, F. Montalenti, A. Rastelli, M. Stoffel, T. Merdzhanova, O. G. Schmidt, and L. Miglio, Physical Review Letters **99**, 235505 (2007).

[76] R. Gatti, F. Uhlík, and F. Montalenti, New Journal of Physics **10**, 083039 (2008).

[77] J. Zoua, X. Z. Liao, D. J. H. Cockayne, and Z. M. Jiang, Applied Physics Letters **81**, 1996 (2002).

[78] M. Hammar, F. K. LeGoues, J. Tersoff, M. C. Reuter, and R. M. Tromp, Surface Science **349**, 129 (1995).

[79] B. J. Spencer and J. Tersoff, Applied Physics Letters **77**, 2533 (2000).

[80] B. J. Spencer and J. Tersoff, Physical Review B **63**, 205424 (2001).

[81] K. Tillmann and A. Förster, Thin Solid Films **368**, 93 (2000).

[82] R. Gatti, A. Marzegalli, V. A. Zinovyev, F. Montalenti, and L. Miglio, Physical Review B **78**, 184104 (2008).

[83] T. Merdzhanova, S. Kiravittaya, A. Rastelli, M. Stoffel, U. Denker, and O. G. Schmidt, Physical Review Letters **96**, 226103 (2006).

[84] A. Portavoce, R. Hull, M. C. Reuter, and F. M. Ross, Physical Review B **76**, 235301 (2007).

[85] A. Pascale, I. Berbezier, A. Ronda, and P. Kelires, Physical Review B **77**, 075311 (2008).

[86] J. L. Gray, R. Hull, and J. A. Floro, Journal of Applied Physics **100**, 084312 (2006).

[87] J. F. Graham, C. D. Kell, J. A. Floro, and R. Hull, Nanotechnology **22**, 075301 (2011).

[88] E. Lausecker, M. Brehm, M. Grydlik, F. Hackl, I. Bergmair, M. Muhlberger, T. Fromherz, F. Schaffler, and G. Bauer, Applied Physics Letters **98**, 143101 (2011).

[89] G. Chen, H. Lichtenberger, G. Bauer, W. Jantsch, and F. Schaffler, Physical Review B **74**, 035302 (2006).

[90] Z. Zhong, A. Halilovic, M. Muhlberger, F. Schaffler, and G. Bauer, Journal of Applied Physics **93**, 6258 (2003).

[91] T. I. Kamins, R. S. Williams, and D. P. Basile, Nanotechnology **10**, 117 (1999).

[92] F. Hackl, M. Grydlik, M. Brehm, H. Groiss, F.Schäffler, T.Fromherz, and G. Bauer, Nanotechnology **22**, 165302 (2011).

[93] Z. Zhong, W. Schinger, F. Shäffler, G. Bauer, G. Vastola, F. Montalenti, and L. Miglio, Physical Review Letters **98**, 176102 (2007).

[94] J. J. Zhang, M. Stoffel, A. Rastelli, O. G. Schmidt, V. Jovanovic, L. K. Nanver, and G. Bauer, Applied Physics Letters **91**, 173115 (2007).

[95] Z. Zhong and G. Bauer, Applied Physics Letters **84**, 1922 (2004).

[96] H. Hu, H. J. Gao, and F. Liu, Physical Review Letters **101**, 216102 (2008).

[97] T. Schülli, G. Vastola, M.-I. Richard, A. Malachias, G. Renaud, F. Uhlík, F. Montalenti, G. Chen, L. Miglio, F. Schäffler, and G. Bauer, Physical Review Letters **102**, 025502 (2009).

[98] R. S. Wagner and W. C. Ellis, Applied Physics Letters **4**, 89 (1964).

[99] J. Westwater, D. P. Gosain, S. Tomiya, S. Usui, and H. Ruda, Journal of Vacuum Science and Technology B **15**, 554 (1997).

[100] K. Hiruma, M. Yazawa, T. Katsuyama, K. Ogawa, K. Haraguchi, M. Koguchi, and H. Kakibayashi, Journal of Applied Physics **77**, 447 (1995).

[101] C. M. Lieber, Solid State Communications **47**, 107607 (1998).

[102] X. Duan and C. M. Lieber, Advance Materials **12**, 298 (2000).

[103] H. J. Fan, P. Werner, and M. Zacharias, Small **2**, 700 (2005).

[104] M. Law, J. Goldberger, and P. Yang, Annual Review of Materials Research **34**, 83 (2004).

[105] K. A. Dick, Progress in Crystal Growth and Characterization of Materials **54**, 138 (2008).

[106] E. Givargizov, Journal of Crystal Growth **31**, 20 (1975).

[107] L. D. Landau and E. M. Lifshitz, *Theory of Elasticity*, 3rd ed. (Butterworth Heinemann, Oxford, 1986).

[108] L. Colombo and S. Giordano, *Introduzione alla teoria elastica. Meccanica dei solidi continui in regime lineare elastico* (Springer-Verlag Italia, Milano, 2007).

[109] B. Devincre, Solid State Communications **93**, 875 (1995).

[110] W. Cai, A. Arsenlis, C. Weinberger, and V. Bulatov, Journal of the Mechanics and Physics of Solids **54**, 561 (2006).

[111] I. N. Remediakis, D. Jesson, and P. Kelires, Physical Review Letters **97**, 255502 (2006).

[112] A. K. Head, Proceeding of the Physical Society B **66**, 793 (1953).

[113] E. V. der Giessen and A. Needleman, Modelling and Simulation in Materials Science and Engineering **3**, 689 (1995).

[114] D. Weygand, L. H. Friedman, E. V. der Giessen, and A. Needleman, Modelling and Simulation in Materials Science and Engineering **10**, 437 (2002).

[115] B. Devincre, R. Madec, G. Monnet, S. Queyreau, R. Gatti, and L. Kubin, *Mechanics of Nano-objects* (Presses de l'Ecole des Mines de Paris, 2011) p. 85.

[116] K. Schwarz, Physical Review Letters **91**, 145503 (2003).

[117] S. Groh, B. Devincre, L. P. Kubin, A. Roos, F. Feyel, and J.-L. Chaboche, Philosophical Magazine Letters **83**, 303 (2003).

[118] Solid State Phenomena **23-24**, 455 (1992).

[119] B. Devincre and L. P. Kubin, Modelling and Simulation in Materials Science and Engineering **2**, 559 (1994).

[120] K. W. Schwarz, Journal of Applied Physics **85**, 108 (1999).

[121] K. W. Schwarz, Journal of Applied Physics **85**, 120 (1999).

[122] D. Weygand, L. H. Friedman, E. V. der Giessen, and A. Needleman, Modelling and Simulation in Materials Science and Engineering **10**, 437 (2002).

[123] H. M. Zbib, T. D. de la Rubia, and V. Bulatov, Journal of Engineering Materials and Technology **124**, 78 (2002).

[124] A. Arsenlis, W. Cai, M. Tang, M. Rhee, T. Oppelstrup, G. Hommes, T. G. Pierce, and V. V. Bulatov, Modelling and Simulation in Materials Science and Engineering **15**, 553 (2007).

[125] X. H. Liu, F. M. Ross, and K. W. Schwarz, Physical Review Letters **85**, 19 (2000).

[126] M. C. Fivel and G. R. Canova, Modelling and Simulation in Materials Science and Engineering **7**, 753 (1999).

[127] L. M. Brown, Philosophical Magazine **10**, 441 (1964).

[128] A. J. E. Foreman, Philosophical Magazine **15**, 1011 (1967).

[129] S. Gavazza and D. Barnett, Journal of the Mechanics and Physics of Solids **24**, 171 (1976).

[130] V. Mohles, Philosophical Magazine A **81**, 971 (2001).

[131] R. Hull and J. C. Bean, Physica Status Solidi (a) **138**, 533 (1993).

[132] V. V. Bulatov, J. F. Justo, W. Cai, S. Yip, A. S. Argon, T. Lenosky, M. D. Koning, and T. D. D. L. Rubia, Philosophical Magazine A **81**, 1257 (2001).

[133] R. Hull and J. C. Bean, Applied Physics Letters **54**, 925 (1989).

[134] M. Ieong, B. Doris, J. Kedzierski, K. Rim, and M. Yang, Science **306**, 2057 (2004).

[135] E. Bugiel, M. Lewerenz, and H. Osten, Physica E: Low-dimensional Systems and Nanostructures **37**, 250 (2007), proceedings of the E-MRS 2006 Symposium E: Science and Technology of Nanotubes and Nanowires.

[136] X. Yu, W. Seifert, O. F. Vyvenko, M. Kittler, T. Wilhelm, and M. Reiche, Applied Physics Letters **93**, 041108 (2008).

[137] M. Lourenço, M. Milosavljević, G. Shao, R. Gwilliam, and K. Homewood, Thin Solid Films **515**, 8113 (2007), asia-Pacific Conference on Semiconducting Silicides Science and Technology Towards Sustainable Optoelectronics (APAC-SILICIDE 2006), July 29-31, 2006, Kyoto.

[138] M. E. Ware and R. J. Nemanich, Thin Solid Films **518**, 1990 (2010).

[139] Y. Bolkhovityanov, A. Gutakovskii, V. Mashanov, O. Pchelyakov, M. Revenko, and L. Sokolov, Thin Solid Films **392**, 98 (2001).

[140] J. C. P. Chang, J. Chen, J. M. Fernandez, H. H. Wieder, and K. L. Kavanagh, Applied Physics Letters **60**, 1129 (1992).

[141] R. S. Goldman, K. L. Kavanagh, H. H. Wieder, V. M. Robbins, S. N. Ehrlich, and R. M. Feenstra, Journal of Applied Physics **80**, 6849 (1996).

[142] J.-S. Park, J. Bai, M. Curtin, B. Adekore, M. Carroll, and A. Lochtefeld, Applied Physics Letters **90**, 052113 (2007).

[143] J. Li, Z. Li, Y. Sheng, and D. Zhang, Applied Physics Letters **91**, 022903 (2007).

[144] R. Hull, J. C. Bean, G. S. Higashi, M. L. Green, L. Peticolas, D. Bahnck, and D. Brasen, Applied Physics Letters **60**, 1468 (1992).

[145] E. Fitzgerald and N. Chand, Journal of Electronic Materials **20**, 839 (1991).

[146] O. Yastrubchak, T. Wosinski, T. Figielski, E. Lusakowska, B. Pecz, and A. Toth, Physica E: Low-dimensional Systems and Nanostructures **17**, 561 (2003), proceedings of the International Conference on Superlattices, Nano-structures and Nano-devices ICSNN 2002 o-structures and Nano-devices ICSNN 2002.

[147] R. Beanland, M. Aindow, T. Joyce, P. Kidd, M. Lourenço, and P. Goodhew, Journal of Crystal Growth **149**, 1 (1995).

[148] M. A. Lutz, R. M. Feenstra, F. K. LeGoues, P. M. Mooney, and J. O. Chu, Applied Physics Letters **66**, 724 (1995).

[149] A. M. Andrews, A. E. Romanov, J. S. Speck, M. Bobeth, and W. Pompe, Applied Physics Letters **77**, 3740 (2000).

[150] A. M. Andrews, J. S. Speck, A. E. Romanov, M. Bobeth, and W. Pompe, Journal of Applied Physics **91**, 1933 (2002).

[151] A. M. Andrews, R. Lesar, M. A. Kerner, J. S. Speck, A. E. Romanov, A. L. Kolesnikova, M. Bobeth, and W. Pompe, Journal of Applied Physics **95**, 6032 (2004).

[152] V. I. Vdovin, Physica Status Solidi (a) **171**, 239 (1999).

[153] B. Pichaud, N. Burle, M. Texier, C. Alfonso, M. Gailhanou, J. Thibault-Pénisson, C. Fontaine, and V. I. Vdovin, Physica Status Solidi (c) **6**, 1827 (2009).

[154] D. Perovic, G. Weatherly, J.-M. Baribeau, and D. Houghton, Thin Solid Films **183**, 141 (1989).

[155] D. D. Perovic and D. C. Houghton, Physica Status Solidi (a) **138**, 425 (1993).

[156] S. C. Jain, A. H. Harker, and R. A. Cowley, Philosophical Magazine A **75**, 1461 (1997).

[157] Y. B. Bolkhovityanov and L. V. Sokolov, Semicond. Sci. Technol. **27**, 043001 (2012).

[158] M. Albrecht, H. P. Strunk, R. Hull, and J. M. Bonar, Applied Physics Letters **62**, 2206 (1993).

[159] J. Godet, L. Pizzagalli, S. Brochard, and P. Beauchamp, Physical Review B **70**, 054109 (2004).

[160] J. Godet, P. Hirel, S. Brochard, and L. Pizzagalli, Journal of Applied Physics **105**, 026104 (2009).

[161] S. Brochard, P. Beauchamp, and J. Grilhe, Physical Review B **61**, 8707 (2000).

[162] S. Brochard, P. Hirel, L. Pizzagalli, and J. Godet, Acta Materialia **58**, 4182 (2010).

[163] C. Li and G. Xu, Philosophical Magazine **86**, 2957 (2006).

[164] Z. Li and R. C. Picu, Journal of Applied Physics **108**, 033522 (2010).

[165] M. Kammler, D. Chidambarrao, K. W. Schwarz, C. T. Black, and F. M. Ross, Applied Physics Letters **87**, 133116 (2005).

[166] E. V. der Giessen and A. Needleman, Modelling and Simulation of Material Science and Engineering **3**, 689 (1995).

[167] R. Gatti, F. Boioli, M. Grydlik, M. Brehm, H. Groiss, M. Glaser, F. Montalenti, T. Fromherz, F. Schaffler, and L. Miglio, Applied Physics Letters **98**, 121908 (2011).

[168] M. Grydlik, M. Brehm, F. Hackl, H. Groiss, T. Fromherz, F. Schäffler, and G. Bauer, New Journal of Physics **12**, 063002 (2010).

[169] K. Sato, M. Shikida, T. Yamashiro, K. Asaumi, Y. Iriye, and M. Yamamoto, Sensors and Actuators A: Physical **73**, 131 (1999).

[170] S. Y. Shiryaev, F. Jensen, and J. W. Petersen, Applied Physics Letters **64**, 3305 (1994).

[171] M. Grydlik, F. Boioli, H. Groiss, R. Gatti, M. Brehm, F. Montalenti, B. Devincre, F. Schaffler, and L. Miglio, Applied Physics Letters **101**, 013119 (2012).

[172] M. Elkurdi, P. Boucaud, S. Sauvage, O. Kermarrec, Y. Campidelli, D. Bensahel, G. Saint-Girons, and I. Sagnes, Applied Physics Letters **80**, 509 (2002).

[173] O. Schmidt and K. Eberl, Electron Devices, IEEE Transactions on **48**, 1175 (2001).

[174] G. Vastola, R. Gatti, A. Marzegalli, F. Montalenti, and L. Miglio, *Self-Assembled Quantum Dots* (Zhiming M. Wang editor, Springer, Berlin, 2008) pp. 421–438.

[175] F. Ross, J. Tersoff, M. Reuter, F. Legoues, and R. Tromp, Microscopy Research and Technique **42**, 281 (1998).

[176] F. Boioli, V. A. Zinovyev, R. Gatti, A. Marzegalli, F. Montalenti, M. Stoffel, T. Merdzhanova, L. Wang, F. Pezzoli, A. Rastelli, O. G. Schmidt, and L. Miglio, Journal of Applied Physics **110**, 044310 (2011).

[177] F. Glas, Physical Review B **74**, 121302 (2006).

[178] A. Atkinson and S. C. Jain, Journal of Physics: Condensed Matter **5**, 4595 (1993).

[179] M.-I. Richard, T. U. Schulli, and G. Renaud, Applied Physics Letters **99**, 161906 (2011).

[180] F. Ross, J. Tersoff, and R. M.Tromp, Physical Review Letters **80**, 984 (1998).

[181] J. J. Zhang, N. Hrauda, H. Groiss, A. Rastelli, J. Stangl, F. Schäffler, O. G. Schmidt, and G. Bauer, Applied Physics Letters **96**, 193101 (2010).

[182] J. Zhang, F. Montalenti, A. Rastelli, N. Hrauda, D. Scopece, H. Groiss, J. Stangl, F. Pezzoli, F. Schäffler, O. Schmidt, L. Miglio, and G. Bauer, Physical Review Letters **105**, 166102 (2010).

[183] G. Vastola, F. Montalenti, and L. Miglio, Journal of Physics: Condensed Matter **20**, 454217 (2008).

[184] F. Boioli, R. Gatti, M. Grydlik, M. Brehm, F. Montalenti, and L. Miglio, Applied Physics Letters **12**, 063002 (1974).

[185] B. J. Spencer and J. Tersoff, Physical Review Letters **63**, 205424 (2001).

[186] J. Zhang, A. Rastelli, O. Schmidt, and G. Bauer, Applied Physics Letters **97**, 203103 (2010).

[187] M. L. Lee, E. A. Fitzgerald, M. T. Bulsara, M. T. Currie, and A. Lochtefeld, Journal of Applied Physics **97**, 011101 (2005).

[188] A. Nainani, S. Raghunathan, D. Witte, M. Kobayashi, T. Irisawa, T. Krishnamohan, K. Saraswat, B. Bennett, M. Ancona, and J. Boos, in *Electron Devices Meeting (IEDM), 2009 IEEE International* (2009).

[189] X. Sun, J. Liu, C. Kimerling, and J. Michel, Optics Letters **34**, 1198 (2009).

[190] H. Ye, P. Lu, Z. Yu, Y. Song, D. Wang, and S. Wang, Nano Letters **9**, 1921 (2009).

[191] Y. Liang, W. D. Nix, P. B. Griffin, and J. D. Plummer, Journal of Applied Physics **97**, 043519 (2005).

[192] S. Raychaudhuri and E. T. Yu, Journal of Vacuum Science and Technology B **24**, 2053 (2006).

[193] S. Raychaudhuri and E. T. Yu, Journal of Applied Physics **99**, 114308 (2006).

[194] T. E. Trammell, X. Zhang, Y. Li, L.-Q. Chen, and E. C. Dickey, Journal of Crystal Growth **310**, 3084 (2008).

[195] J. Colin, Physical Review B **82**, 054118 (2010).

[196] I. A. Ovid'ko and A. G. Sheinerman, Philosophical Magazine **84**, 2103 (2004).

[197] L. Lauhon, M. Gudksen, C. Wang, and C. Lieber, Nature **420**, 57 (2002).

[198] F. Qian, S. Gradecak, S. Y. Li, C.-Y. Wen, and C. M. Lieber, Nano Letters **5**, 2287 (2005).

[199] C.-H. Lee, J. Yoo, Y.-J. Doh, and G.-C. Yi, Applied Physics Letters **94**, 043504 (2009).

[200] P. Parkinson, H. J. Joyce, Q. Gao, H. H. Tan, X. Zhang, J. Zou, C. Jagadish, L. M. Herz, and M. B. Johnston, Nano Letters **9**, 3349 (2009).

[201] P. W. W. van Tilburg, R. E. Algra, W. G. G. Immink, M. Verheijen, E. P. A. M. Bakkers, and L. P. Kouwenhoven, Semiconductor Science and Technology **25**, 024011 (2010).

[202] G. Liang, J. Xiang, N. Kharche, G. Klimeck, C. M. Lieber, and M. Lundstrom, Nano Letters **7**, 642 (2007).

[203] J. Xiang, A. Vidan, M. Tinkham, R. M. Westervelt, and C. M. Lieber, Nature Nanotechnology **1**, 208 (2006).

[204] Y. Hu, H. O. H. Churchill, D. J. Reilly, J. Xiang, C. M. Lieber, and C. M. Marcus, Nature Nanotechnology **2**, 622 (2007).

[205] D. C. Dillen, K. M. Varahramyan, C. M. Corbet, and E. Tutuc, Physical Review B **86**, 045311 (2012).

[206] I. A. Goldthorpe, A. F. Marshall, and P. C. McIntyre, Nano Letters **9**, 3715 (2009).

[207] S. A. Dayeh, J. Wang, N. Li, J. Y. Huang, A. V. Gin, and S. T. Picraux, Nano Letters **11**, 4200 (2011).

[208] F. M. Ross, J. Tersoff, and M. C. Reuter, Physical Review Letters **95**, 146104 (2005).

[209] I. A. Goldthorpe, A. F. Marshall, and P. C. McIntyre, Nano Letters **8**, 4081 (2009).

[210] K. L. Kavanagh, J. Salfi, I. Savelyev, M. Blumin, and H. E. Ruda, Applied Physics Letters **98**, 152103 (2011).

[211] K. L. Kavanagh, Semiconductor Science and Technology **25**, 024006 (2010).

[212] K. L. Kavanagh, I. Savelyev, M. Blumin, G. Swadener, and H. E. Ruda, Journal of Applied Physics **111**, 044301 (2012).

[213] H. Chu, J. Wang, C. Zhou, and I. Beyerlein, Acta Materialia **59**, 7114 (2011).

[214] S. A. Dayeh, W. Tang, F. Boioli, K. L. Kavanagh, H. Zheng, J. Wang, N. H. Mack, G. Swadener, J. Y. Huang, L. Miglio, K.-N. Tu, and S. T. Picraux, Submitted to Nano Lett. (2012).